Abstract

Multi-objective Optimal Design of Low Noise Launch Pad using Empirical Method with Genetic Algorithm

Seoryong Park

Department of Mechanical and Aerospace Engineering

The Graduate School

Seoul National University

The acoustic loads are intense acoustic waves generated by the supersonic jet plume of launch vehicle during a lift-off. They can be sources of vibration and deteriorate the external devices like antenna panels or internal electronic components. Thus, it is important to predict the acoustic loads and acoustic environment around the launch vehicle during a lift-off.

There are two representative acoustic loads prediction methods, numerical and empirical method. Since the cost of predicting the acoustic environment around the launch vehicle is very expensive, many studies have been done based on the empirical method. The most representative empirical prediction method is called distributed source method(DSM) developed by NASA SP-

8072. But this method is based on free jet data, there are disadvantages that some physical phenomena cannot be considered. In this dissertation, the improved empirical prediction methods are developed to consider some physical phenomena that occur in real condition but are not considered in original method.

Meanwhile, as the recent launch environment has been diversified, many studies are under way for low noise launch pad. In addition, it is emphasized that the low noise launch pad also needs to consider additional requirements such as impact force on the launch pad and the construction cost. Many studies related to this optimized low noise launch pad were carried out mainly based on numerical method with63 high cost. But in this dissertation, the prediction was performed by the improved empirical method. To do this we have introduced some methods to the empirical method, 1) NURBS (Non-Uniform Rational B-Spline) which is a method that can simulate curved launch pad shape freely and 2) NSGA-II (Non-dominated Sorting Genetic Algorithm-II) which is a multi-objective genetic algorithm. Then we examined the accuracy and efficiency of the results of the empirical approach about the multi-objective optimal design of low noise launch pad.

Keywords: Acoustic Loads Prediction, Empirical Method, Additional Physics, Multi-objective Optimization, Low Noise Launch Pad, NURBS, NSGA-II

Contents

iv

List of Tables

List of Figures

xii

Chapter 1. Introduction

1.1. Background

In the 2000s, the total budget for space technology has grown steadily due to the expansion of investment of developing countries. And a large proportion of the budget is occupied by satellites and launch vehicles. Launch vehicles developed in each country are used for their own satellites (non-commercial services) or for other countries satellites that do not have launch vehicles (commercial services). The market size of commercial services of launch vehicle has steadily increased since 2006, and the whole market size of launch vehicle is also expected to continue to increase as the satellite utilization of each country increases[1]. On the other hand, space technology related to the launch vehicle is considered as an intensifier of various industrial technologies such as machinery, aviation, materials, electronics, etc. And it is one of industries demanding the high technology because it requires extreme performance. In this commercial and scientific aspect, it is very important to have an independent technology of the launch vehicle

Especially, a load analysis is an essential requirement for stable performance of launch vehicle[2, 3]. The outer surface of the launch vehicle is constituted by thin plates, and in the fairing many devices are loaded with

1

mission-critical equipment such as vibration-sensitive navigation electronics. On the other hand, the launch vehicle is exposed to various vibration environments according to the flight conditions, and there is a possibility that the vibration causes the degradation of the robustness of the fuselage, vibration on the mounted electronic equipment, and malfunction. Therefore, the load analysis is essential to predict loads at the design stage and to properly design the dynamic characteristics of the body structure so that vibration responses above critical value will not be generated. On the other hand, Acoustic loads analysis is known to be especially important at the lift-off stage. During a lift-off, the supersonic combustion jet flow can radiate tremendous acoustic power close to 100 MW and make harsh acoustic environment through the interaction with the launch pad or the surrounding structure. Since the radiated acoustic waves are very intense [4], they can affect the internal or external structure of launch vehicle in the form of acoustic loads.
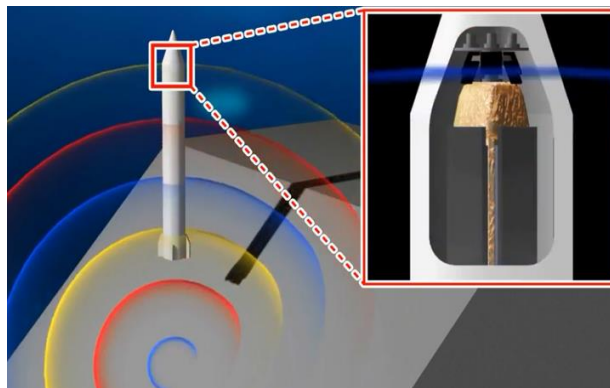
Fig. 1.1. Acoustic loads during a lift-off[5]

1.1.1. Acoustic Loads

Acoustic loads are defined by sound pressure fluctuation on the surface of the launch vehicle. Primary source of acoustic loads is known as jet flow-induced turbulent mixing noise. A lot of knowledge about the acoustic loads was developed during the early years of space flight, particularly during the Apollo program. Experiments have shown that sound levels are up to 160 decibels (dB) on the launch vehicle surface and it is 100-1000 times stronger acoustic energy relative to aircraft noise of 100-120 decibels[6]. So, in general, the main concern is focused on how to predict these powerful acoustic loads and reduce them.

1.1.2. Acoustic Loads Prediction Methods

There are three methods for predicting acoustic loads; theoretical, numerical and empirical methods. Firstly, theoretical studies which are based on Light hill's theory have been applied for jet noise prediction of high-speed vehicle both in subsonic[7, 8] and supersonic[9, 10] cases. However, because of complexity of noise source and configuration of launch pad, this approach seems to be hard to be applied to real acoustic environment. Secondly, numerical method is based on solving the 3D compressible Naiver-Stokes equation. A typical method is two-step prediction method in which flow region and noise propagation region are divided as shown in Figure 1.2.
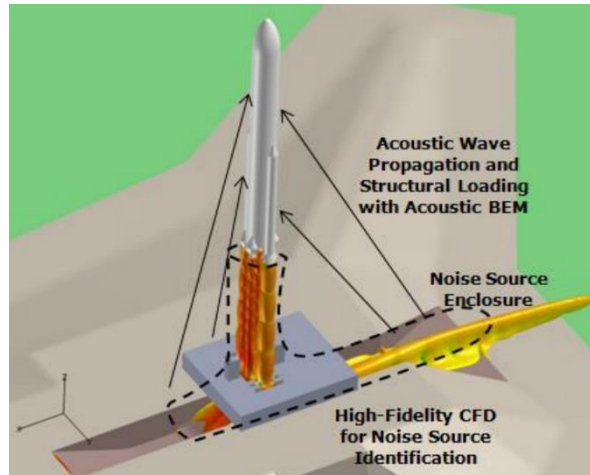
Fig. 1.2. Numerical based acoustic loads prediction method[17]

This method includes acoustic analogy both integral methods [11, 12] and differential method [13-16]. Computational fluid dynamics (CFD) used in the flow region can completely model the real launch vehicles with multiple plumes interacting with detailed surrounding structures. So, simulations with this numerical method are capable of capturing the sources of acoustic waves originating from the plume interaction with the facility structures[17]. For this reason, using the numerical method, practical simulations of acoustic fields around the launch vehicle have been conducted for design of new rocket launch site[18-20]. In addition, studies on the multi-objective optimal design of low noise launch pad have been proceeding based on numerical approach spending enormous computation cost[21].

However, the jet flow of the launch vehicle has a very high Reynolds number, which means that it requires tremendous computation time when

4

using the Large Eddy Simulation(LES) method. Therefore, there are problems in cost and effectivity of numerical method. For example, Tatsukawa et al.[21] conducted multi-objective optimal design for a rocket launch site using the evolutionary algorithm with the LES, but too much computational cost is required. Evaluation of one case took about 7 hours and required the use of 1,040 CPU cores of "K" supercomputer whose computational speed is several hundred thousand times faster than a personal computer and they had to solve the 2,500 cases for the multi-objective optimization problem.

On the other hands, empirical method is based on various jet experimental data containing much of jet knowledge. Most representative empirical method is proposed by Eldred in the report of NASA SP-8072[22]. It is known as distributed source method(DSM) placing sources along the jet plume axis and giving them characteristics of a source by taking similarity principle for source power, spectrum, and directivity. It is divided by two types of methods according to the characteristics of distributed sound source. DSM-I places point sources having narrow band components and DSM-II places slice sources having broadband components. Because DSM-I shows a nonphysical result at the moment when the flame axis suddenly breaks[23], many researchers have conducted studies based on DSM-II[24-26]. This DSM-II has advantages of cost-effective and relatively simple to implement.

5

As the DSM-II provides relatively accurate results for a conventional launch vehicle within 4 dB in terms of overall sound pressure level (OASPL) and also gives comprehensive prediction results, many domestic[27-30] and international researchers have been using it for a long time[31-41].

However, this method is based on the experimental data limited to 'free jet', many studies using the DSM-II have been confined to conventional launch environments and couldn't consider various acoustic phenomena like impingement[6, 42], diffraction[25, 29], reflection effects[37] related to the interaction of jet plumes and launch pad. In addition, the noise sources are distributed in a simple manner, it is difficult to freely simulate various launch pad shapes such as having curved shapes of low noise launch pad.

Recently, studies related to acoustic loads have been required for the efficient and practical acoustic field prediction as the launch environment has become diversified. However, as described before, there is a limit to using so far developed prediction methods to simultaneously overcome both the computational cost efficiency problem(numerical) and the realistic acoustic field simulation problem(empirical). Even though the numerical method has advantages in simulating the real physical phenomena, there are problems such as dissipation and dispersion error and computational cost inevitably. Also, the empirical method which has advantages in the efficiency is difficult to reflect the various physical phenomena for the

diversified launch environment, and hard to simulate the change of acoustic fields by the height elevation.

In this dissertation, the purpose is to develop novel methods that can additionally consider the physical phenomena not considered in the original empirical prediction method such as diffraction, reflection and impingement effects and to extend it to the latest study of multi-objective optimization problems. We first complement the existing empirical method by introducing some models that can consider missing phenomena. This allows the empirical method to be applied to a variety of launch environments, and in particular to provide a realistic description of the acoustic environment by height variation. Next, we apply this improved empirical method to the study of multi-objective optimal design of low noise launch pad that was mainly studied by numerical method.

In the following section, previous research regarding the empirical and numerical method will be reviewed.

1.2. Literature Review

In order to gain more insight into the objectives of this dissertation, the previous research regarding the empirical and numerical investigation for the acoustic loads prediction will be reviewed. Despite many researcher's efforts to overcome the disadvantages of original empirical method, the

problem of underestimation in the high-frequency range still persists in empirical based research. On the other hands, in the numerical research case, we can see the results of state-of-art research related to the acoustic loads, which is the goal of this dissertation to study the same condition by using improved empirical method in order to examine the results comparison of the two approach.

1.2.1. Empirical Based

There are two common features in almost research based on empirical method. The first is that it has problem of underestimation in the high-frequency range. The second is that the shape of spectrum is always smooth-shaped spectrum, because the original empirical method always provide that type of spectrum from the similarity principle. In fact, it is not a problem for most acoustic loads prediction cases, because the shape of the spectrum is known to be mostly smooth-shaped for the noise of launch vehicles with very high speeds and temperatures. However, it can be a problem for a flight vehicle that is not as large as a launch vehicle or is heavily influenced by the surrounding structure, as in the following case.
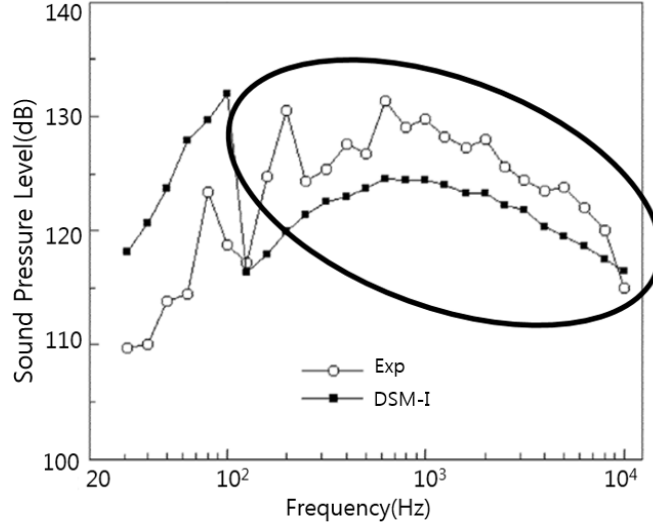
Fig. 1.3 Acoustic loads prediction results for Spain missile[23]

Figure 1.3 shows the prediction result of Campos[23] using DSM-I not DSM-II due to feature of the spectrum of missile. The experimental result shows that the shape of spectrum of missile is not a smooth-shaped but having many local peaks. It is due to the influence of surrounding structure such as a canister and the characteristics of rocket. On the other hand, the spectrum of DSM-I shows a nonphysical region near the frequency of 10^2 (Hz). This is because the directivity of the narrowband point source near the region where the axis suddenly changes is directly influenced. And figure 1.3 also shows the problem of underestimation in the high-frequency range.

ONERA's research group, represented by Varnier[6], carried out many experiments of supersonic impinging jet for the acoustic loads prediction of ARIANE 5. From this experiments, they established an important

9

conclusion that will be the basic assumption of acoustic efficiency in this dissertation that the acoustic efficiency, the ratio of acoustic power to mechanical power, is independent of the shape of the obstacle and of its distance from the nozzle if the Mach number is constant. And also, Varnier[26] suggested several modification to the original empirical method such that the characteristic length must be reduced and the fully expanded jet data must be used instead of the jet exhaust data to overcome the problem of underestimation in the high-frequency region mentioned earlier.

However, there were still many cases having same problem in the high-frequency range. Kandula[37] additionally considered the ground reflection effect to overcome this problem. But figure 1.4 shows that it still had underestimation problem in the high-frequency range despite considering the effect of ground reflection.
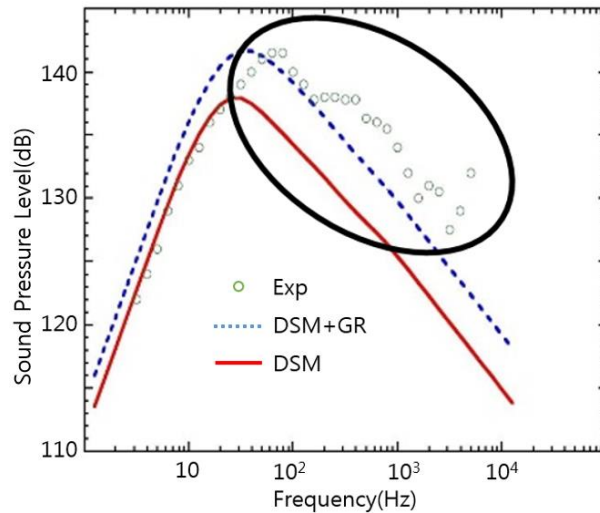
Fig. 1.4. Underestimation case of empirical method: Kandula[37]
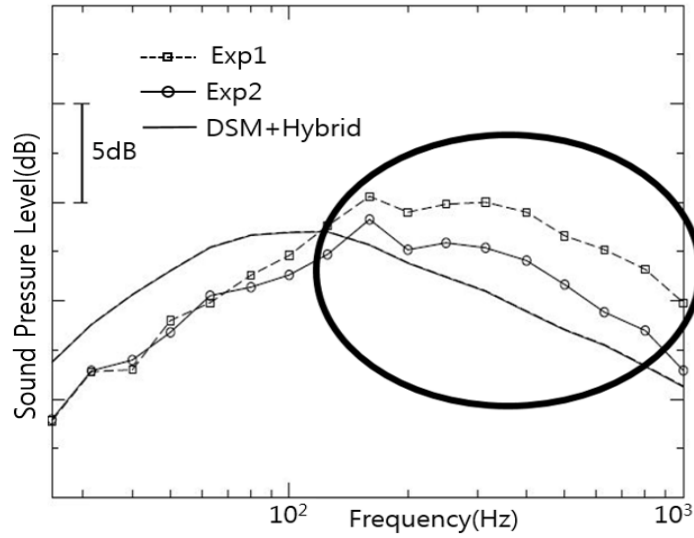
Fig. 1.5. Underestimation case of empirical method: Casalino[32]
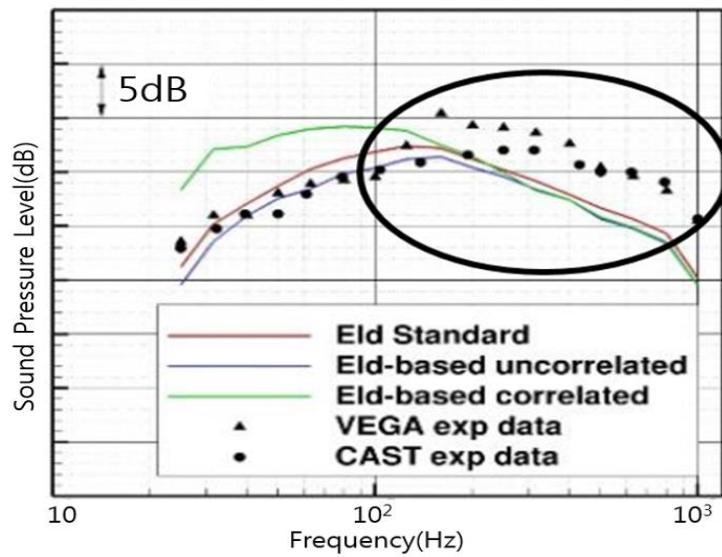
Fig. 1.6. Underestimation case of empirical method: Barbarino[43]

Casalino et al.[32] attempted a hybrid CAA-empirical approach. The jet sources extracted from the empirical method were used to convolute a database of tailored Green's function computed by means of the frequency-domain CAA code. This approach permitted to take into account the real launch pad geometry and mean flow refraction effects in the jet stream. This research showed that tuning the original empirical model is required in order to improve the accuracy of the prediction and using elementary-source CAA solutions permits to reduce some discrepancies between the experiments and the empirical results. However, figure 1.5 shows that this improved method has also problem of underestimation in high-frequency range.

In 2016, Barbarino et al.[43] pointed out that the sources of standard empirical method are uncorrelated. So, an improvement of the Eldred's original model was suggested. This new modification contained an explicit expression for the acoustic pressure of each source, in terms of amplitude and phase, in order to investigate the sources correlation effects and to propagate them through a wave equation. However, even if the results were improved through his method, it can be seen that the prediction result still have the problem of underestimation in the high-frequency range as shown in figure 1.6.
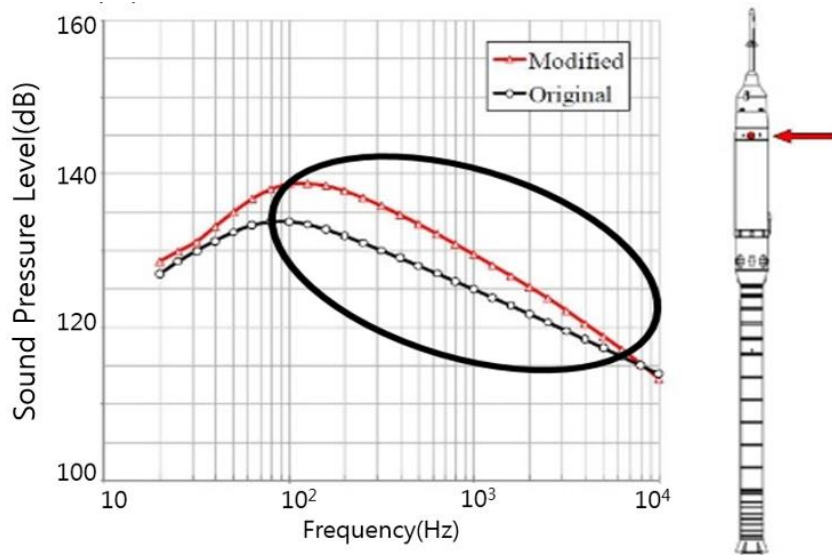
Fig. 1.7. Modification of underestimation problem: Haynes[24]
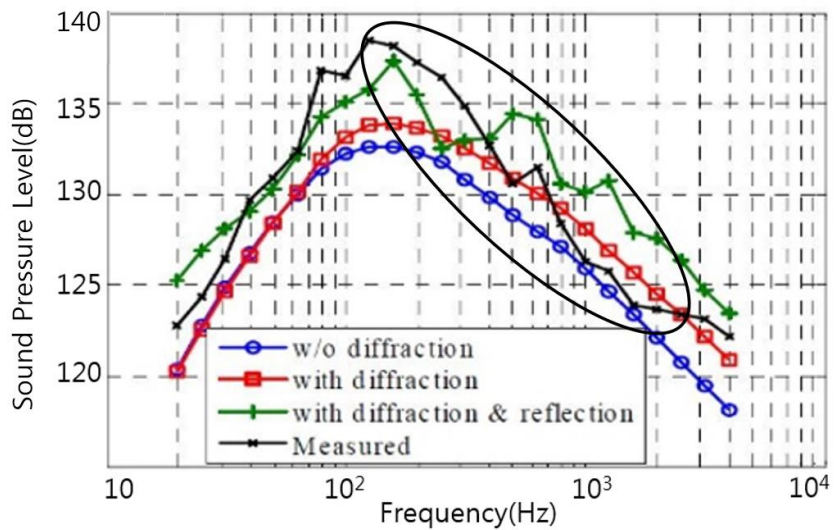
Fig. 1.8. Modification of underestimation problem: Choi[30]

To overcome this problem, Haynes et al.[24] proposed three modifications including a shorter core length, a core termination concept, and a new set of directivity index measured from static firing tests. In particular, the idea of terminated core length was originated from the jet impingement and it can reduce the range of source distribution and peak source location. This modification made the peak levels shifted two third-octave bands higher in frequency shown as figure 1.7. On the other hand, Choi et al.[30] proposed several source line locations and included diffraction and reflection effect. Then they chose the source line location as the centerline of the turbulence kinetic energy contour and the result of modification is shown as figure 1.8.

As described above, many studies based on empirical methods have been carried out in order to complement those that the original method does not consider. And it can be found that the most common weakness of the original method is the underestimation problem in the high-frequency range. In this dissertation, a new improved empirical method is suggested to solve this problem by considering additional impingement effect that is missed in the original method. Although many attempts of previous research to solve this problem have led to some improvements, that is not a fundamental solution and also not a general solution but a limited method in a special case. Therefore, our study of implementing additional impingement source according to the height variation can solve the inherent problems of original

empirical method and it can greatly expand the utilization of empirical prediction method. As can be seen in the next section, the development of this improved empirical method implies that the empirical method can be alternative for the latest study of the multi-objective optimal design of low noise launch pad which is only studied by numerical approach.

1.2.2. Numerical Based

Unlike the empirical method using the similarity principle based on the free jet experiments, numerical method can simulate various conditions existing in actual launch environment. In real launch environment, acoustic radiation due to small, large scale turbulence from the supersonic jet can cause strong interaction with surrounding structures. Many researchers[44, 45] divide the flow structure and acoustic fields of supersonic impinging jet into three part, main jet, impingement, and wall jet region.
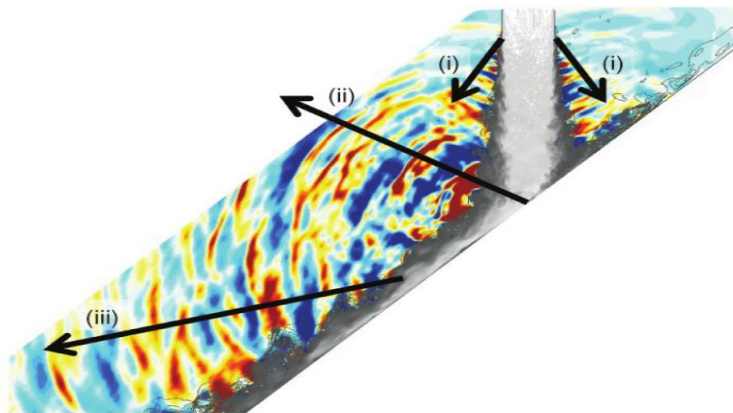
Fig. 1.9. Three types of acoustic waves of supersonic impinging jet[46]

Nonomura et al.[46] also said that the acoustic fields indicate that there are three types of acoustic waves in all the cases shown as figure 1.9: (i) Mach waves generated from the shear layer of the main jet, (ii) acoustic waves generated from the impingement region, and (iii) Mach waves generated from the shear layer of the supersonic flow downstream of the jet impingement. This study emphasized the second type of wave (ii) because the original empirical method does not consider such acoustic waves[46]. So they discussed the effects of nozzle-plate distance on the second type of acoustic waves (ii).

On the other hands, Tsutsumi et al.[18-20] considered that reflection of highly energetic Mach wave from the main jet and the acoustic wave from
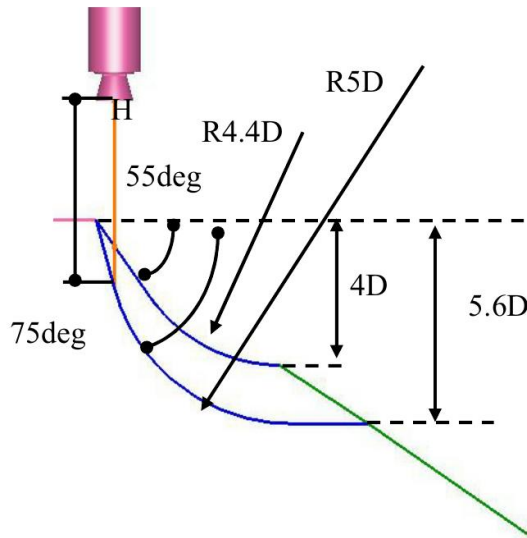
Fig. 1.10. Comparison of flame deflector shape with curvature[19]

16

the impingement region towards the vehicle are the main mechanisms for the high acoustic loads. Considering these two acoustic components, Tsutsumi et al.[18-20] studied the development of a new launch pad shape to reduce the acoustic loads on the launch vehicle. Figure 1.10 shows that low noise launch pad is designed as a various curved shape to reduce the acoustic loads.

Recently, numerical based studies have been carried out toward designing low noise launch pad. Tatsukawa et al.[21] has further studied the multi-objective optimal design of low noise launch pad considering additional objective functions. By further considering the view point of maintenance and construction cost, they investigated the correlation between each objective variable. They adopted Non-dominated sorting genetic algorithm-II(NSGA-II) known as a state-of-art technique as optimization method and
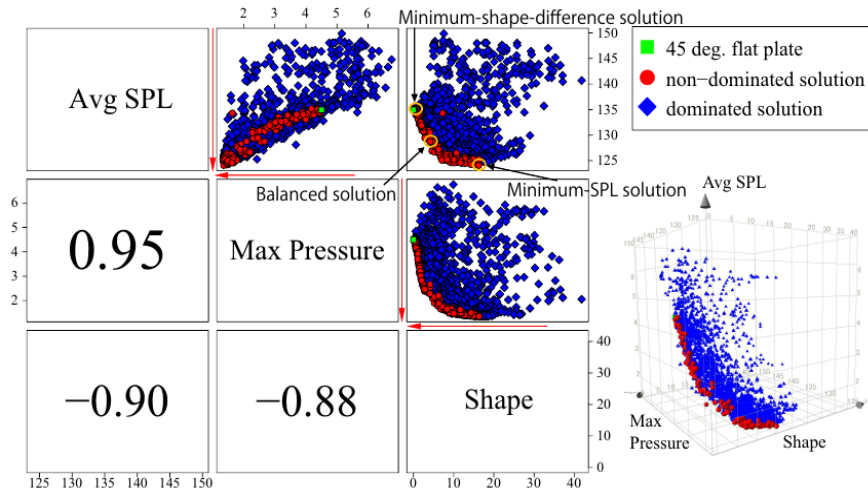
Fig. 1.11. Correlation coefficients and scatter plots[21]

17

they compared three solutions which are called by 'minimum-shape-difference solution', 'minimum-SPL solution' and 'balanced solution' having moderate value for each objective function.

Numerical based acoustic loads prediction method can simulate acoustic wave generation mechanism which is difficult to be considered in empirical method. Therefore, it is possible to study the design of various low noise launch pad. However, even if the computing power is getting better, the computational cost is still big problem. For example, numerical acoustic loads simulations of West et al.[17] are executed with up to 300M mesh cells on more than 3000 processors on the NASA NAS Pleiades supercomputer. And the study of Tatsukawa et al.[21] took more than 2weeks with 6,500 nodes of "K" supercomputers.

Therefore, although the numerical method can be useful for predicting acoustic loads of future launch vehicle in various launch environments, it is difficult to be used in iterative calculations for many prediction cases or in optimization problem.

1.3.   Objectives and Scope

In this dissertation, the improved empirical prediction method will be used to study the multi-objective optimal design of the low noise launch pad,

which is the latest research that has been mainly studied through numerical methods. For this purpose, this dissertation is organized in two stages.

At first, two improved empirical acoustic loads prediction methods are developed. The feature of the improved methods is that it can considers the additional physics that the original empirical prediction method does not consider. Additional physical phenomena are diffraction, reflection and impingement and each is applied through some models applicable to original empirical method.

The most important feature of the improved empirical methods is the additional impingement effect. As mentioned above, it was known that the impingement source was not considered in the original empirical method because it is based on the free jet experiments. In fact, there has been little research on directly considering this impingement source and only Kudryavtsev et al.[33] proposed an empirical method by classifying the noise source area into four regions and assigning characteristics to each area. However, this method cannot be applied to various situations in a general way due to limitations that can be applied only for their special case, and the process of characterizing the noise source is also unclear. On the other hand, the method developed in this dissertation is a method of placing additional impingement noise sources to the original empirical method with the four characteristics of impingement source and can be applicable to various

19

situations as a general method because it takes the general characteristics of impingement source according to impingement height and jet characteristics. This improved empirical method will be validated and verified for various rocket situations and it will be used as basis empirical method for the future low noise optimization design problem.

Meanwhile, the diffraction and reflection effects are also considered by well-known methods, each of which is Maekawa's thin screen model[47] and image source method. Although there are many studies on the effect of diffraction by barriers, Maekawa's method is the most fundamental and useful to be applied to existing acoustic loads prediction methods. In fact, these effects of diffraction by barrier and ground reflection have been previously studied for acoustic loads prediction[25, 30, 37, 40]. However, in this dissertation, unlike the previous studies, these two effects are not applied to the launch vehicle but limited to the missile in the canister comparable with the case of Spain missile[23]. This is because, in case of the launch vehicle to be validated in this dissertation, there is no surrounding structure that will cause diffraction phenomenon, and it will be replaced by impingement source instead of reflection phenomenon.

For this first stage, the novel contributions of this dissertation can be summarized as follows.

i) Improved empirical acoustic loads prediction methods are developed to consider additional physical phenomena that original empirical method cannot consider.

ii) The method of considering the impingement effect can solve the underestimation problem in the high-frequency range which has long been a challenge for many studies.

iii) The method of considering the impingement effect can simulate the acoustic environment around the launch vehicle similar to the real environment according to the height increases

iv) The method of considering the diffraction and reflection effects can more realistically and physically explain the results of acoustic loading on the missile launched in the canister

Secondly, based on the improved empirical method, the study of multi-objective optimal design of low noise launch pad is conducted considering three objectives, SPL, impact force and shape difference from the reference shape. The reason for considering these three objectives is that the study of the multi-objective optimal design of low noise launch pad is a state-of-art study of numerical method and there are comparable numerical results under this condition. To accomplish this research, some additional methods are needed for empirical method. First, the curved launch pad shape should be free to simulate. In the original empirical method, the path of the jet flame

axis is expressed by several simple vertices, but curved launch pad shapes are essential to the low noise optimization problem. Therefore, in this dissertation, the method of distributing the curved noise source was considered by using NURBS (Non-Uniform Rational B-Spline) method. Next, an optimization algorithm for multi-objective design of launch pad is required. NSGA-II is adopted as an optimization algorithm because the NSGA-II is the state-of-art technique in the multi-objective optimization field[48] in terms of computational cost, approach method, diversity and reliability of solutions. In the multi-objective optimization problem, the primary purpose is having an ability to find multiple Pareto-optimal solutions in one single run. So, by using NSGA-II the multiple-solutions can be obtained simultaneously, constituting Pareto-optimal solutions with each objective function influencing.

For this second stage, the novel contributions of this dissertation can be summarized as follows.

    i)   NURBS, which is mathematical method of expressing 2D or 3D geometry, is combined with the empirical method and this make it possible to simulate easily a curved launch pad shape like a low noise launch pad.

    ii)   Multi-objective optimization algorithm, NSGA-II, combined with the improved empirical method makes it possible to conduct a

multi-objective optimal design of low noise launch pad by using an improved empirical method

iii) The study of multi-objective optimization based on the empirical method can show reasonable results in terms of accuracy and reliability when compared with the latest numerical study, especially having advantages in computation cost

To summarize again, in this dissertation, the study of multi-objective optimal design of the low noise launch pad will be carried out based on the empirical acoustic loads prediction method. For this purpose, it is necessary to develop improved empirical methods that can consider additional impingement effects, and to combine NURBS which is a source distributing method and the NSGA-II which is multi-objective optimization algorithm. The final solutions will be examined and compared with the numerical method to see the meaning of the final solution in terms of accuracy and efficiency.

1.4. Outline of Dissertation

To provide an outline of this dissertation, the contents of the chapters are presented in the following.

In Chapter 2, the development of improved empirical acoustic loads prediction method will be presented. In the section 2-1, some characteristics

of the original empirical method are examined. Then the characteristics of a typical supersonic jet noise component are reviewed and the relation with the empirical acoustic loads method is examined. Then detailed prediction procedure will be described about the original empirical method. In the section 2-2, the first improved empirical method is discussed, which can consider diffraction and reflection effects by surrounding structures such as the canister. This method will be applied to Spain missile and the results will be examined. And in the section 2-3, typical supersonic 'impinging' jet noise components are also reviewed and then the acoustic wave generated from impingement region will be discussed as an impingement source. To apply that source to the empirical method, the impingement source is modeled based on some results of impinging jet studies. And then the validation process will be carried out for several rocket cases.

In Chapter 3, Multi-objective optimization of low noise launch pad based on the improved empirical method will be presented. In the section 3-1, the low noise launch pad concept having curved shape is discussed. Then the NURBS method to simulate the curved launch pad shape freely and the validation process will be presented. In the section 3-2, by using the optimization algorithm, NSGA-II, the multiple optimized solutions for the three objective function, SPL, impact force and construction will be

obtained. The optimized solutions are compared with a numerical based solutions and the accuracy and reliability of the analysis will be examined.

In Chapter 4, summarization of this dissertation and conclusions and will be included.

Chapter 2. Improved Empirical Acoustic Loads Prediction Method

2.1   Original Empirical Method

The empirical acoustic loads prediction method proposed by NASA SP-8072[22] is the most representative acoustic load prediction method. In this paper, Eldred proposed the empirical method by summarizing the theoretical and experimental data on the supersonic jet noise since 1950 due to the interest in space development. In this method, the noise sources are distributed along the jet flame axis as shown in figure 2.1 using the theoretical equations and the non-dimensional experimental results, the similarity principle, and the characteristics of power, spectrum and directivity are assigned to each noise source. The acoustic loads are obtained by superimposing the influence of each noise source and whole prediction procedure is illustrated in figure 2.2. This empirical method is called distributed source method(DSM) because it is the method of distributing the noise sources along the jet flame axis and it is divided into DSM-I and DSM-II depending on the characteristics of the distributed sources. The sources of DSM-I are point sources having narrow band components and of DSM-II are slice sources having broadband components.

26
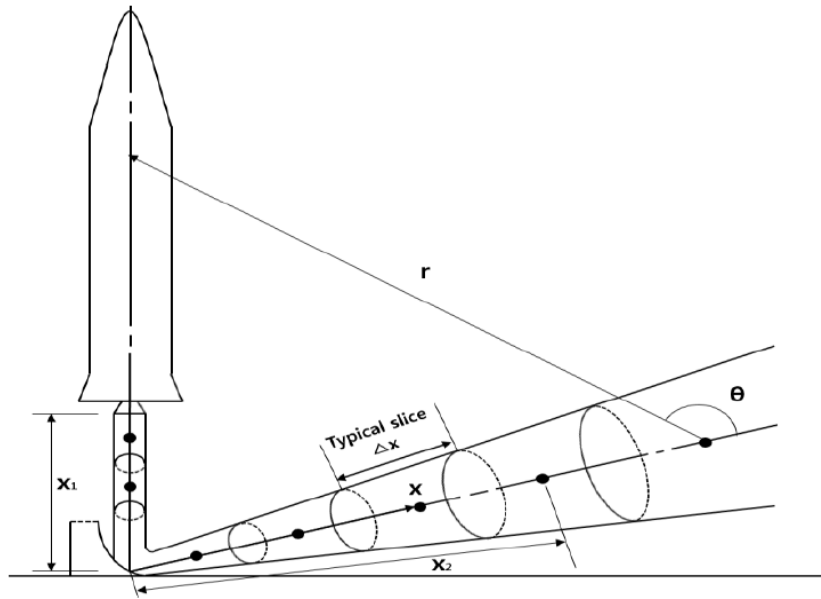
Fig. 2.1. Schematic sketch of noise source distribution of empirical method
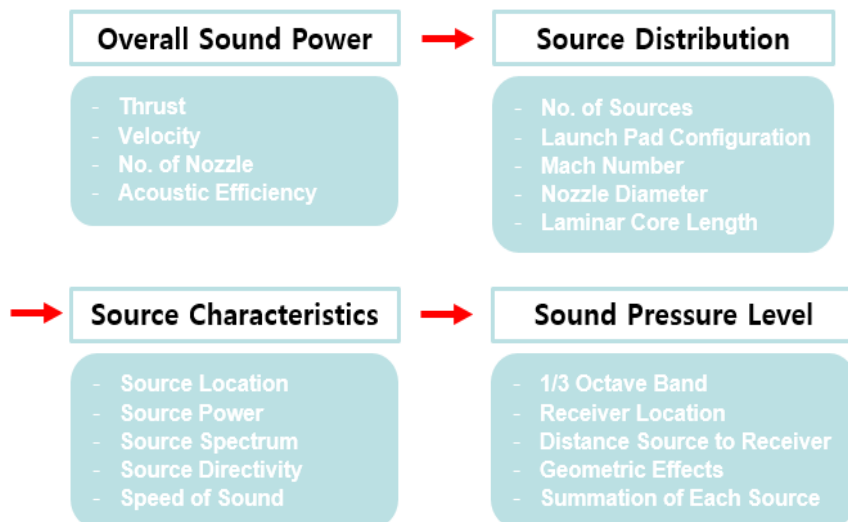
Fig. 2.2. Prediction procedure of distributed source method(DSM)

He mentioned three principle parameters affecting acoustic loading as follows.

    i)   Rocket-nozzle exit-flow parameters

    ii)   Vehicle, stand, and flow geometry

    iii) Vehicle velocity

The parameters associated with i) and ii) can affect acoustic loading by changing the noise generation characteristics. However, iii) causes to change the relative relationship between sound propagation velocity and vehicle velocity. Acoustic loading decreases as the vehicle gains velocity[49, 50]. As shown in figure 2.3, when the vehicle reaches sonic velocity, the acoustic loading from the rocket exhaust decreases to an insignificant value since the vehicle's speed exceeds the propagation velocity of the noise.

The plot shows a curve labeled $20\log(1 - M_\infty)$, with the y-axis "Relative sound pressure level on vehicle(dB)" ranging from 0 to -40, and the x-axis "Free-stream Mach number, M_∞" ranging from 0 to 1.0.
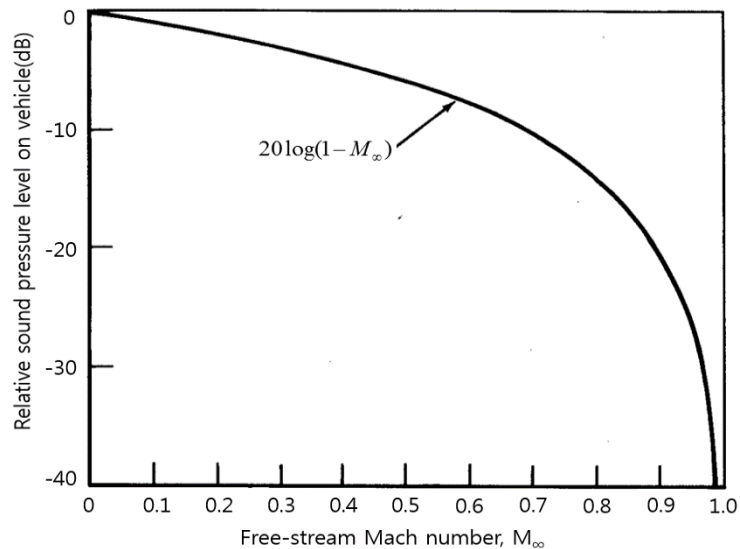
Fig. 2.3. Estimated effect of vehicle velocity on acoustic loading[22]

He anticipated that the maximum acoustic loading occurs during ground firings or starting to lift off from a launch stand. It is because the vehicle velocity is almost zero and the effect of deflector in such a situation. For standard configurations, the flow is deflected by impinging on the ground plane or deflector. Then it brings the exhaust flow closer to the vehicle, increasing the noise level over the vehicle. This effect is illustrated in figure 2.4, 2.5. The increase resulting from flow deflection at launch is significant until the distance between the nozzle and deflector is nearly 70 to 100 nozzle-exit diameters. When this distance is reached, most of the noise is generated in the un-deflected exhaust flow and free from the effects of the deflector. In this way, in the original empirical method, acoustic loading is maximally predicted at the starting lift-off due to the vehicle velocity having nearly zero and much closer exhaust flow of launch vehicle by the deflector.

However, the practical experimental results show that there are higher altitudes where the launch vehicle is affected by larger acoustic loads than when the starting lift-off. This empirical method was not able to reflect the increased the acoustic loads effect due to the elevation of height because it only considered the turbulent mixing noise from exhaust flow as the main component of acoustic loads. Therefore, before developing the improved empirical method, the components of a typical supersonic jet noise will be reviewed in the next section.

2.1.1 Supersonic Jet Noise

Since the 1950s, there have been many experiments and studies on supersonic jet noise[51-56]. In 1995 paper, Tam[57] summarized the supersonic jet noise into three components, 1) turbulent mixing noise, 2) broadband shock-associated noise and 3) screech tones. The turbulent mixing noise is associated with both fine and large-scale turbulence structures. And both the broadband shock-associated noise and screech tones are associated with shock cell structure.

2.1.1.1 Mach Wave

For the turbulent mixing noise, it is now generally accepted that both fine and large-scale turbulence structures contribute to the turbulent mixing noise of a supersonic jet. However, the relative importance of their contribution depends on the extent on the jet Mach number and temperature. For supersonic jets and especially high temperature jets, unlike subsonic jets, the large turbulence structures propagate downstream at supersonic Mach number relative to the ambient sound speed producing intense Mach wave radiation. The Mach wave radiation easily predominates over the noise from fine-scale turbulence, making the large turbulence structures the dominant noise source of supersonic jets[57]. Thus only the component of Mach wave generated by the large turbulence structures will be discussed.

The first literature relating supersonic jet noise directly to the Mach wave radiation problem is the study of Phillips[58]. He predicted that turbulent shear layers with supersonic convection velocities, relative to that of the acoustic medium, radiate in the form of Mach waves. Subsequently, Ffowcs Williams[59] and Ribner[60] did a similar interpretation within the framework of their acoustic analogy[56]. They said that how the Mach waves are generated resembles the formation by thin bodies moving supersonically[58] or supersonic flow over a slightly irregular wavy-wall[56] developed from the nozzle exit as shown figure 2.4 and 2.5. So they can be described conveniently as 'eddy Mach waves'. In fact, many visualization techniques such as shadowgraph, schlieren, etc have been indicating the characteristics of Mach wave shown as figure 2.6.
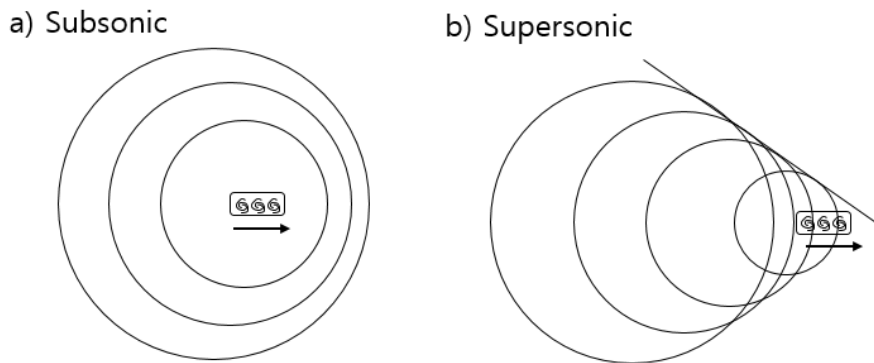
Fig. 2.4. Acoustic wave formation by moving body of eddies
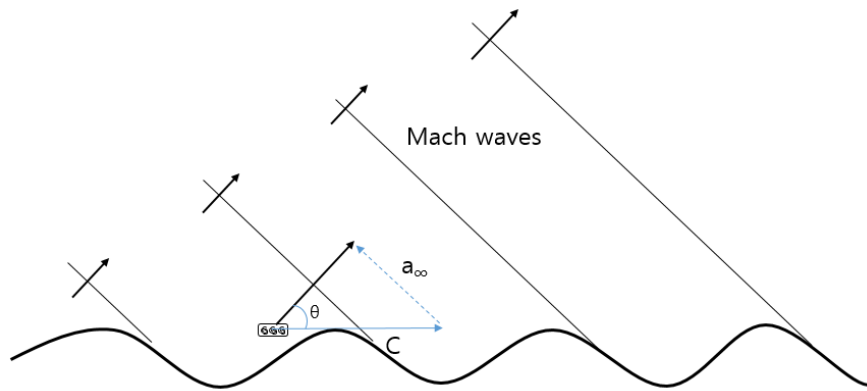
Fig. 2.5. Schematic sketch showing Mach wave radiation generated by wavy surface traveling at supersonic phase velocity C
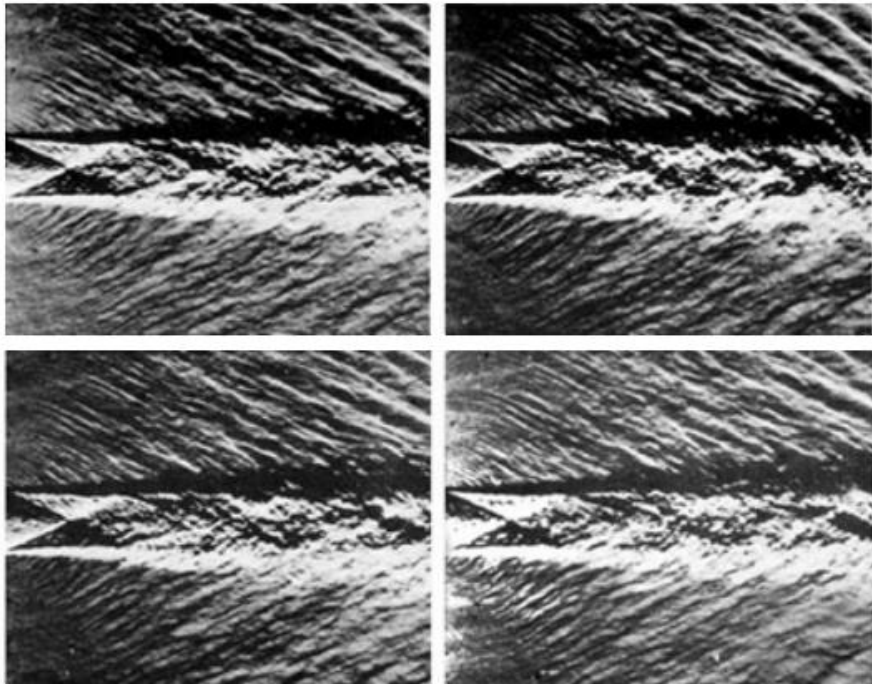
Fig. 2.6. Frame series of Mach waves generated in supersonic jet [61]

From the experiments, it is clear that the Mach waves have the form of long, straight and equal angle. The maximum radiation angle of Mach waves is known about 45 to 60 degree from the jet flow direction shown as figure 2.7. At the same time, it also has a feature that contains a relatively large amount of low-frequency components than other noise sources, having the peak values at a Strouhal number of around 0.1. Therefore, the characteristics of the Mach wave are categorized as follows.

     i)   Mach wave is turbulent mixing noise and most dominant noise source of supersonic jet noise.

     ii)   The dominant propagation direction is the downstream of jet direction. (45 to 60 degree from the jet flow)

     iii) It has spectrum that the low frequency component is dominant.
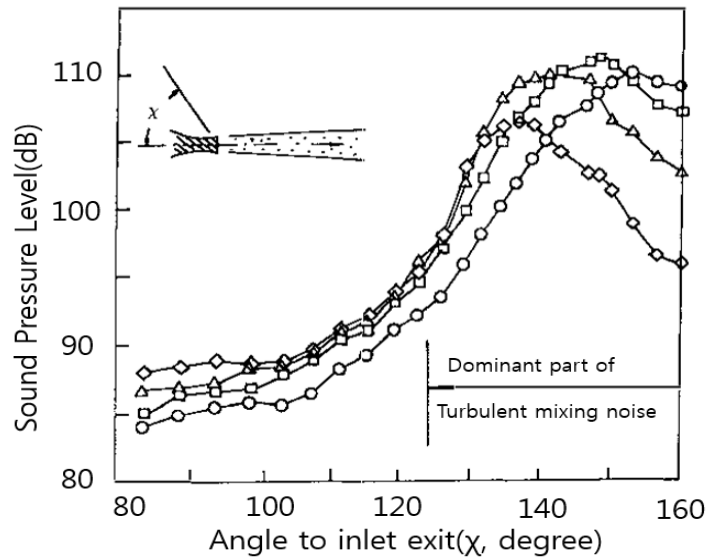
Fig. 2.7. Directivities of turbulent mixing noise for supersonic jet[57]

2.1.1.2   Broadband Shock-Associated Noise(BSAN)

Broadband shock-associated noise(BSAN) is related with the shock cell

system in imperfectly expanded jets. Harper-Bourne[62] first deal with the

broadband shock-associated noise by theoretical model. After that, many

studies[63-68] found that the mechanism by which the BSAN is generated

is by the downstream propagating large scale turbulence structures and their

interactions with the quasi-periodic shock cell structure. And the presence

of this BSAN makes supersonic jet noise shifted to high-frequency range

and directional characteristics. The main characteristics of the BSAN are

categorized as follows.

    i)   BSAN is shock associated noise that occurs anywhere with

         shock cell structure and turbulence.

    ii) The dominant propagation direction is the upstream of jet

         direction.

    iii) Compared to the spectrum of the Mach wave, the spectrum of

         the BSAN is dominant in the high-frequency range.

2.1.1.3   Screech Tone Noise

Powell[69, 70] first observed the screech tones from supersonic jets. Since

then, many studies[52, 71-75] found that the screech tone is a discrete tone
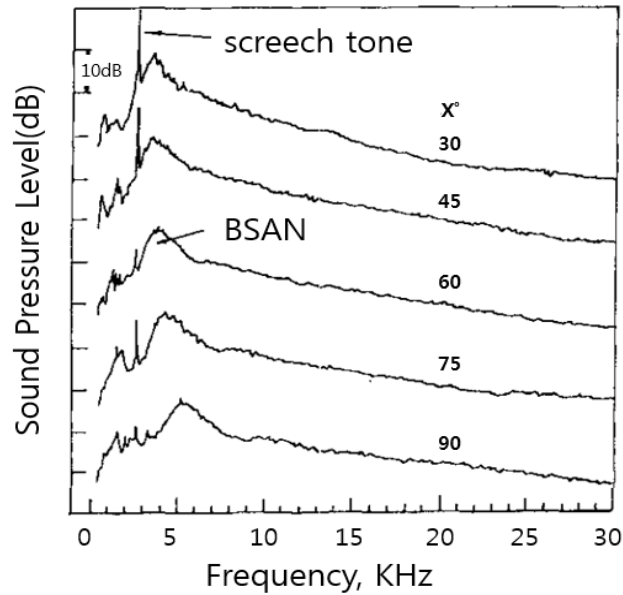
Fig. 2.8. Sound spectrum of under expanded jet[76]

radiated by imperfectly expanded jets having a significant upstream directivity. Screech tone is generated and sustained by a resonant feedback loop: 1) sound generated by passage of eddies through shock cells 2) upstream propagation toward the nozzle lip, and cogeneration of new eddy by coupling of the sound with the shear layer instability. However, this phenomenon occurs mainly in the case of cold supersonic jets not in highly hot supersonic jets[77, 78] and mostly in the case of plat plate deflector which is perpendicular to the jet axis. In this case, the broadband turbulent mixing noise is large enough to disguise the tones even if it exists. So, the screech tones can be ignored in the acoustic environment of launch vehicle.

2.1.2 Distributed Source Method II(DSM-II)

As mentioned above, the most representative study of predicting acoustic loading is the empirical method of NASA which is called distributed source method, DSM-II[22] placing slice sources having broadband spectrum. Based on the similarity principle, this empirical method assigns values of power, spectrum, and directivity to noise sources placed along the jet flame axis. The specific prediction procedure is as follows.

The first step is to determine the overall acoustic power(W_{OA}) emitted from the launch vehicle. the overall acoustic power is determined by the capability of the rocket engine and acoustic efficiency using equation (2.1).

$$W_{OA} = \eta\left(\frac{1}{2}n\dot{m}U_e^2\right) = 0.5\eta nFU_e \text{ (W)} \tag{2.1}$$

Where $\dot{m}$ is the mass flow rate (kg/s), U_e is the nozzle exit velocity (m/s), n is the number of nozzles, F is the thrust (N) of each engine, and η is the acoustic efficiency, which is defined as the ratio of sound power to the rocket exhaust's mechanical power.

$$\eta = W_{OA} / W_{mechanic} \tag{2.2}$$

The acoustic efficiency is usually 0.5 ~ 1% based on experimental data. On the other hand, Sutherland[79] proposed the acoustic efficiency as the following formula.

$$\eta = 0.0012 \left(\frac{\gamma_t}{\gamma_0}\right)\left(\frac{a_t}{a_0}\right)^3\left(\frac{a_t}{U_e}\right)^2 \qquad (2.3)$$

γ is the specific heat ratio, a is the sound speed, and the subscripts t

and 0 refer to the core tip and the ambient condition, respectively.

After the overall acoustic power is determined, the overall power is distributed to each source depending on the distance of each source from the nozzle exit along the flow axis over the laminar core length, as shown in figure 2.9. In this procedure, the laminar core length L_T which means the length of maintaining the laminar core from the nozzle exit is an important parameter for determining the range of the distributed sources and their power, and is determined using equation (2.4).

$$L_T = 3.5D_e\left(1 + 0.38M_e\right)^2 \qquad (2.4)$$
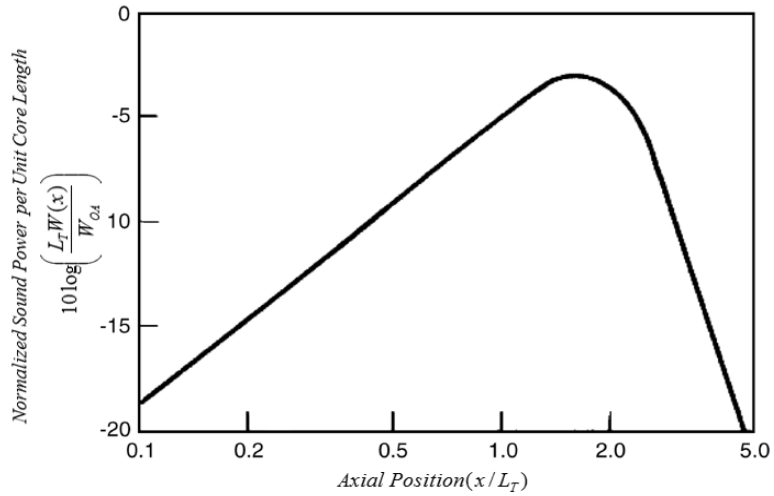
Fig. 2.9. Relative source power distribution along the jet plume axis[22]

37

Where D_e is the exit diameter of the nozzle (m) and M_e is the exit Mach number. On the other hands, Varnier et al.[26] and Haynes et al.[24] suggested different equations of laminar core length based on their own experimental data each as the following equations.

$$L_T = 1.75 D_j \left(1 + 0.38 M_j\right)^2 \tag{2.5}$$

$$L_T = \min(1.75 D_j \left(1 + 0.38 M_j\right)^2, H) \tag{2.6}$$

The subscripts j refers to the fully developed condition and H is distance between the nozzle exit and deflector.

Once the laminar core length is determined, as can be seen in figure 2.9, the total range of the distributed sources is determined as five times the laminar core length. And the maximum source power is located around 1.8 times the laminar core length from the nozzle exit. At this point, one fact can be checked that the location of maximum source power is around 1.8 L_T. This is almost consistent with the maximum location of turbulent mixing noise of common supersonic jets, which means that this method considers turbulent mixing noise including Mach wave as the dominant source as mentioned before.

From the figure 2.9, the overall sound power level of each slice source $L_{w,s}$ is calculated from equation (2.7).

$$L_{w,s} = 10\log\left(\frac{L_T W(x)}{W_{OA}}\right) + L_w + 10\log\frac{\Delta x}{L_T} \tag{2.7}$$

The first term on the right-hand side is obtained from figure 2.9, $W(x)$ is the sound power (W/m) at a distance x   from the nozzle exit along the flow axis, Δx is the length of the source slice (m), and L_w is the overall sound power level calculated from equation (2.8). The unit of sound power is the decibel (ref : $10^{-12}W$).

$$L_w = 10\log(W_{OA}) + 120 \tag{2.8}$$

Figure 2.10 shows the sound power spectrum to be allocated for each distributed source according to the modified Strouhal number, which is normalized with the distance from the nozzle to the source location. It determines the characteristics of the spectrum of the sources. The closer a source is from the nozzle exit, the larger the values of the high-frequency band noise are. Then figure 2.10 and equation (2.8) could be used, and converted to the normalized spectrum of figure 2.10 to a conventional sound power spectrum, such as power spectrum per Hz, per 1/3 octave, or per octave, as desired.

$$L_{w,s,b} = L_{w,s} + 10\log\left(\frac{W(f,x)}{W(x)}\frac{U_e a_o}{xa_e}\right) + 10\log\left(\frac{xa_e}{U_e a_o}\right) + 10\log\Delta f \tag{2.9}$$
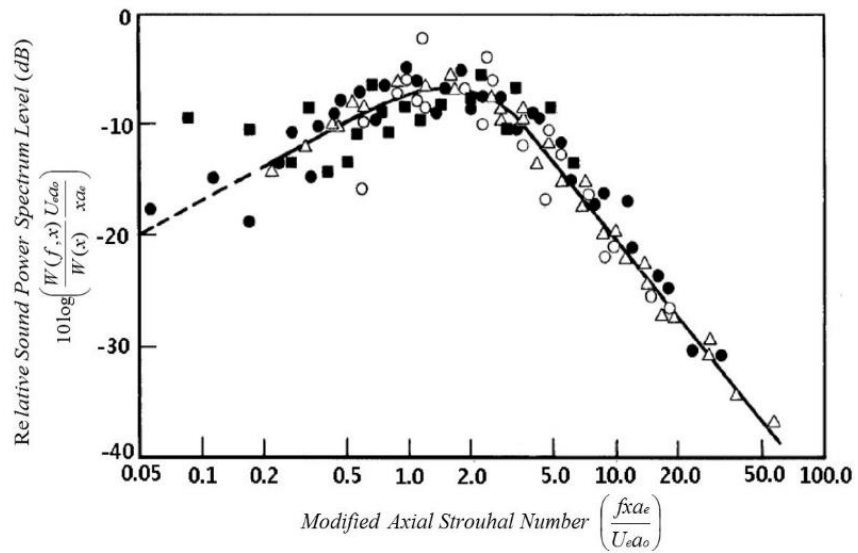
Fig. 2.10. Normalized Sound power spectrum of distributed source[22]
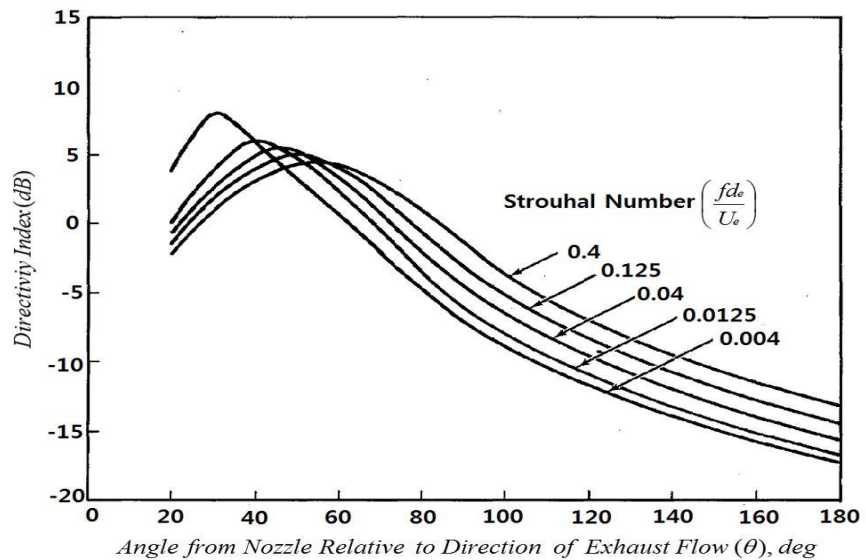
Fig. 2.11. Directivity factor as a function of observation angle and
several Strouhal number[22]

40

$L_{w,s,b}$ is the sound power level of each frequency band of each source. The second term on the right-hand side is obtained from figure 2.10. $W(f,x)$ is the sound power per Hz per unit axial length at distance x along the flow axis (W/Hz/m), and a_o, a_e are the speeds of sound in the atmosphere and at the nozzle exit (m/s), respectively, and Δf is the bandwidth of the frequency band (Hz).

In this method, sound propagation from the distributed sources is calculated by the geometric relationship between the noise sources and the receiver, considering its directivity characteristic as shown figure 2.11. At this point, we can also check the characteristics of the distributed sources in DSM-II as the turbulent mixing noise, Mach wave. Previously, as shown in the section of '2.1.1.1 Mach wave', the maximum directivity of turbulent mixing noise is formed around 45-60 degree from the jet downstream direction. Therefore, when compared with figure 2.11, it can be confirmed that the directivity of the noise sources used in the DSM-II also consistent with turbulent mixing noise.

Then, the sound pressure level contributed by each slice on the observer location, $SPL_{s,b,p}$, is calculated from equation (2.10).

$$SPL_{s,b,p} = L_{w,s,b} - 10\log\left(r^2\right) - 11 + DI(b,\theta) \qquad (2.10)$$

Where r is the length of the radial line from each source to the observer position, and $DI(b,\theta)$ is the directivity index that depends on the geometric relationship between the source and the receiver. Lastly, we sum up the contribution from each source logarithmically and obtain the total sound pressure level in the frequency band b at the observer location p, $SPL_{b,p}$ (ref : $2 \times 10^{-5} N/m^2$), from equation (2.11).

$$SPL_{b,p} = 10\log\left(\sum_s 10^{\frac{SPL_{s,b,p}}{10}} \right) \qquad (2.11)$$

Thus, through this procedure, we can implement DSM-II to predict acoustic loads.

2.1.3   Limitations

In this section, we confirm the limitations of DSM-II. Although the DSM-II is known as a relatively simple and cost-effective method, it has weaknesses because it is based on specific experimental data particularly based on free jet. So, it is difficult to consider various acoustic phenomena like diffraction, reflection and impingement effects induced by the interaction of the sources with the surrounding structures.

First, if there is a missile in canister at lift-off, it cannot consider the canister which make the acoustic loads increased or decreased because DSM-II was developed in 1972 so it is mostly appropriate only for the

conventional lift-off case. Secondly, as emphasized before, the noise sources considered in DSM-II is only turbulent mixing noise in terms of the location of the maximum source power, spectrum, and directivity. Although the turbulent mixing noise including Mach wave is the dominant component of the supersonic jet, there are impingement noise sources due to the jet collision caused by the launch pad in the practical lift-off environment. In the DSM-II, they tried to overcome problem of impinging jet by only deflecting the jet flow axis from the deflector[6] which brings about the increased acoustic loading effects by geometric change like figure 2.12. However, in order to obtain the prediction accuracy through this effect, the acoustic efficiency was taken excessively conservative value (1%)[22] and there was still a problem that the additional source by impingement cannot be considered. This limitation leads to the problem of underestimation in the high-frequency range as shown before the section of 1.2.1
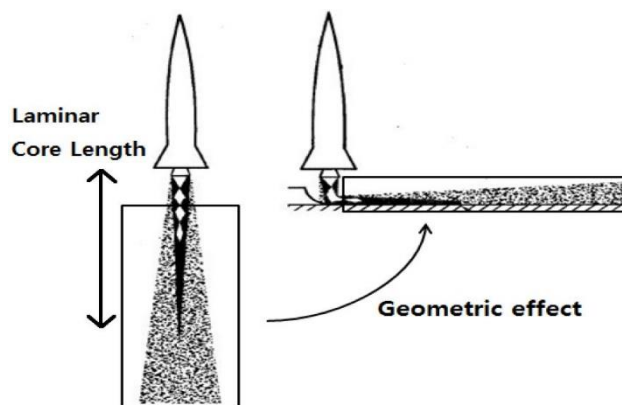
Fig. 2.12. Deflected jet axis reflecting the geometric effect of impinging jet[22]

43

So in the next section we will look at the methods to overcome these limitations of the DSM-II. In the section of 2.2, we will develop the first improved empirical method that can consider the surrounding structure such as a canister. Two simple methods to consider the diffraction effect and the reflection effect will be applied to the original DSM-II and its effect will be verified. And the section of 2.3, we will develop the second improved empirical method that can consider additional impingement source directly depending on the height. This second improved empirical method can make the acoustic fields more realistic without taking excessive acoustic efficiency. And this method will also be used for launch pad optimization in subsequent chapter 3 after verifying the prediction accuracy according to increasing height

2.2   Improved Empirical Method – Surrounding Structure

If there are walls near the noise sources, the acoustic loading on the vehicle is increased by reflection effect, and if there are obstacles between the sound sources and the receiver, acoustic loading is decreased by diffraction effect. Figure 2.13 shows launch environment of missile enclosed by canister. In this case, the jet noise inner the canister actively interacts with the surrounding structure, making additional diffraction and reflection effects unlike the conventional type of lift-off environment

Fig. 2.13. Launch environment of missile enclosed by canister

As previously explained, it is difficult for DSM-II to explain these phenomena. However, by applying some simple models, we can consider these effects in DSM-II.

2.2.1 Diffraction Effects – Thin Screen Model

To consider the diffraction effect, we adopted an empirical diffraction model, the thin screen model of Maekawa[47]. This model is based on the fact it is difficult to calculate the diffraction of sound accurately, so it is reasonable to adopt an empirical method. From the figure 2.14, we can include the diffraction effect as attenuation values based on the geometric relationship among the source, receiver, and structure. Using the geometric relationship, we can obtain the Fresnel's zone number N from equation (2.12).
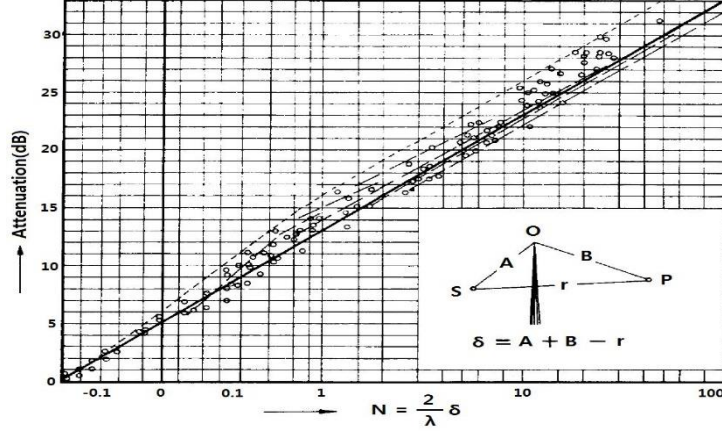
Fig. 2.14. Empirical attenuation values in terms of Fresnel's zone
number by diffraction effect[47]

$$N = \frac{2}{\lambda}\delta \qquad (2.12)$$

λ is the wavelength of sound, and the geometric parameter δ is obtained
by equation (2.13). This is shown in the figure 2.14.

$$\delta = A + B - r \qquad (2.13)$$

A and B are the distance from the tip of the obstacle to the source and
the receiver, respectively. We can apply this method to the case of like figure
2.13 by considering an additional attenuation value, which is represented by
the fifth term on the right hand side of equation (2.14).

$$SPL_{s,b,p} = L_{w,s,b} - 10\log(r^2) - 11 + DI(b,\theta) - Diff(N) \qquad (2.14)$$

46

2.2.2   Reflection Effects – Image Source Model

On the other hand, sources in the canister are reflected as the vehicle goes up. This reflection effect leads to increased acoustic loading on the vehicle resulting in the phase difference, but this effect is not included in DSM-II. This phenomenon can be explained using simple image source model, as shown in figure 2.15. This is based on the concept that if there is a wall, the reflected noise has the same effect as the image source. We apply this model to the sources influenced by the canister. It could make an increase in the acoustic loading and make spectrum have local peak, which will be more realistic and physically acceptable compared to the original smooth-shaped spectrum from the DSM-II. How this image source model is applied to DSM-II will be explained. The sound pressure on the receiver is determined by summation of the values from the original source and the image source, as given by equation (2.15).
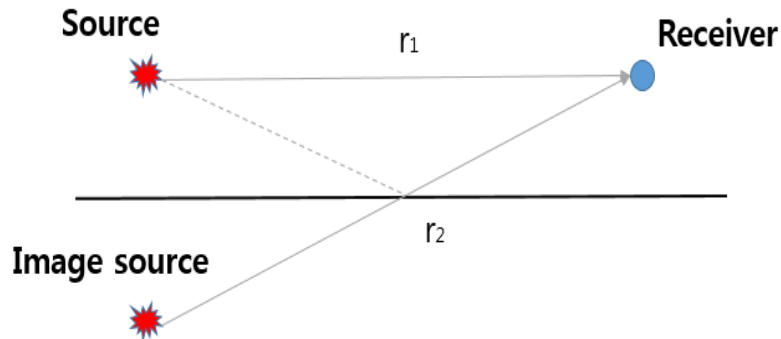
Fig. 2.15. The concept of image source model by reflection effect

$$p' = \frac{Xe^{i(\omega t + kr_1)}}{r_1} + Q(f,\phi)\frac{Xe^{i(\omega t + kr_2)}}{r_2} \qquad (2.15)$$

X is the magnitude of sound pressure of the original source and $Q(f,\phi)$ is the reflection coefficient of the canister which is function of frequency and phase, r_1 is the direct path distance from the original source to the receiver, and r_2 is the distance from the image source to the receiver. Though there are many reflection paths from the source to the receiver through the canister, we assume that there is only one reflection path and apply the reflection effect according to the geometric relationship among the source, receiver, and structure. We conservatively take the reflection coefficient value as one, and consider the spectrum of the image source to be the same as that of original one. Thus, we can rewrite the equation (2.15) to consider the phase difference as following equation.

$$p' = p_1 \cos(\omega_1 t) + p_2 \cos(\omega_2 t + \phi) \qquad (2.16)$$

p_1 is sound pressure of the original source on the receiver through the direct path and p_2 is of the image source. ω_1 and ω_2 are frequencies of the two sources, and ϕ is phase difference induced by the path disparity between two sources. To obtain the root mean square(RMS) values of sound pressure, we have to integrate the above equation after squaring the values. We can assume that sound pressure coming from each independent source

48

can be added by same frequency band, and get the RMS value on the receiver as given in equation (2.17).

$$\overline{p'^2} = \frac{1}{2} p_1^{\ 2} + \frac{1}{2} p_2^{\ 2} + p_1 p_2 \cos \phi \qquad (2.17)$$

Where the phase difference ϕ is obtained from equation (2.18).

$$\phi = \frac{r_1 - r_2}{c} \times f \times 360 \qquad (2.18)$$

Therefore, by considering some image sources, we can include the reflection effect in DSM-II as given in equation (2.19). This term will result in increased acoustic loading on the vehicle and a more realistic and physically acceptable results compared to the original smooth-shaped spectrum results of DSM-II.

$$SPL_{img,b,p} = L_{img,s,b} - 10\log\left(r_{img}^{\ 2}\right) - 11 + DI_{img}(b, \theta) \qquad (2.19)$$

In the following section, we ascertain these effects through analysis of the missile enclosed by canister.

2.2.3   Verification Case and Result

Unlike the conventional launch vehicle case, the missile targeted in this verification is initially in a canister as shown in figure 2.16 and the specification of engine used in the analysis is shown in Table 2.1. This environment has a significant effect on acoustic loads during lift-off. In this

49

section, we apply empirical method that could include various acoustic phenomena caused by this untypical condition.
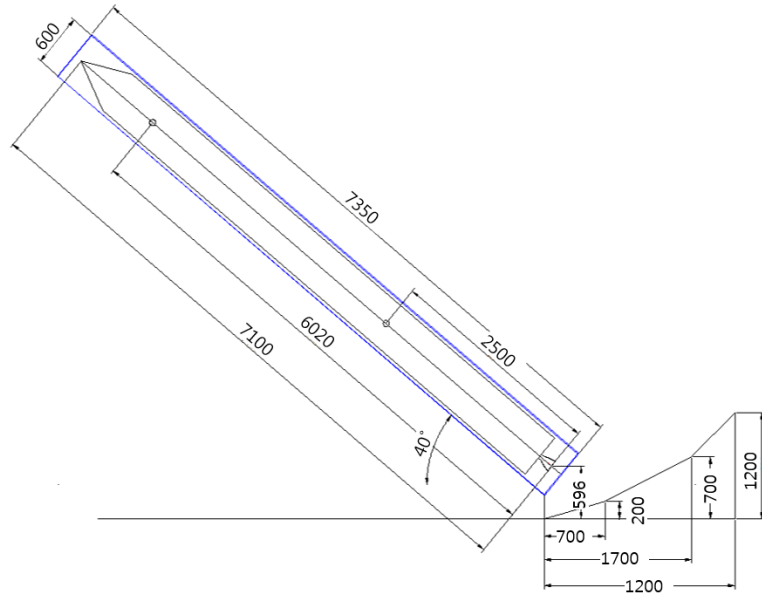
Fig. 2.16. Dimensions of launch pad and location of receiver points

Table 2.1. Specification of missile

Parameter	Value
Number of nozzle	1
Nozzle exit diameter (m)	30.54
Engine thrust (N)	119.50
Exit velocity (m/s)	1629.07
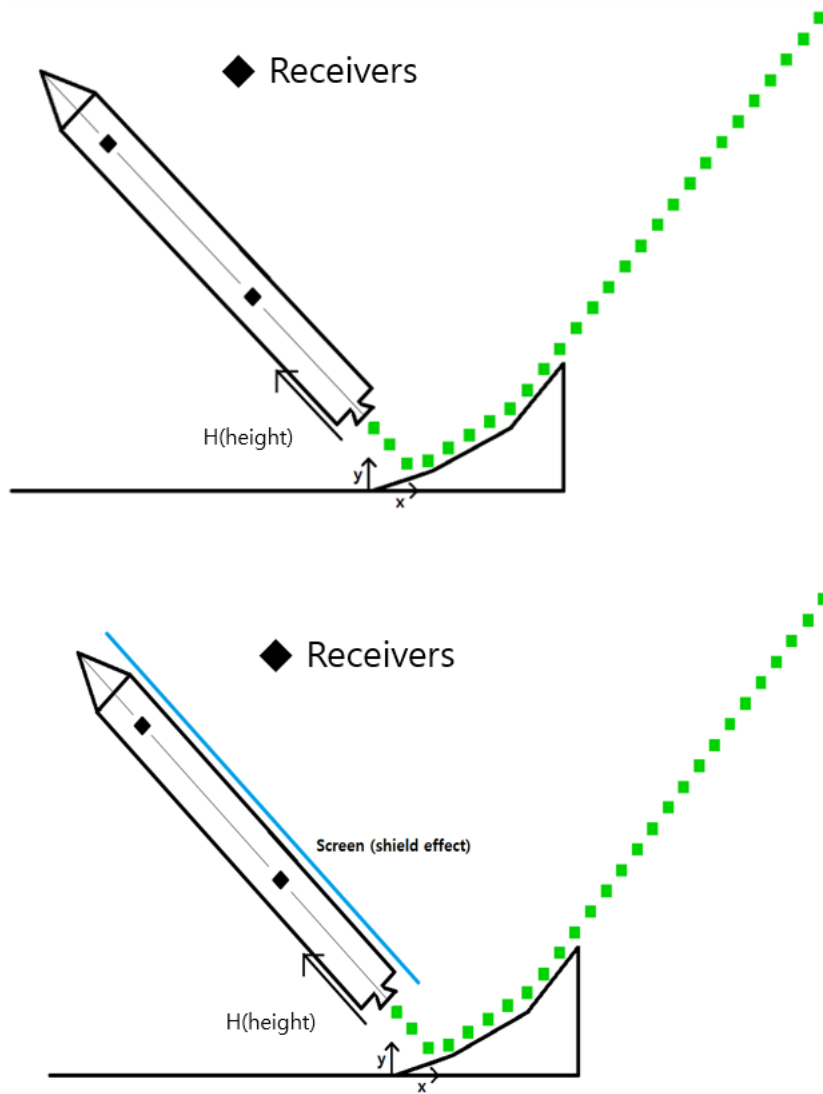
Fig. 2.17. Configuration of source distribution during a lift-off
(Upper: without a canister, Lower: with a canister)

The canister surrounding the vehicle can cause sound diffraction. Figure 2.17 shows the configurations of the distributed sources based on DSM-II without and with the canister. When the canister is considered as an obstacle, it interrupts the direct path from source to receiver. The extent of diffraction is determined by the geometric relationship, and we can apply the thin screen model to the empirical method as described before. Figure 2.18 shows the comparison of prediction results depending on height without and with thin screen theory.
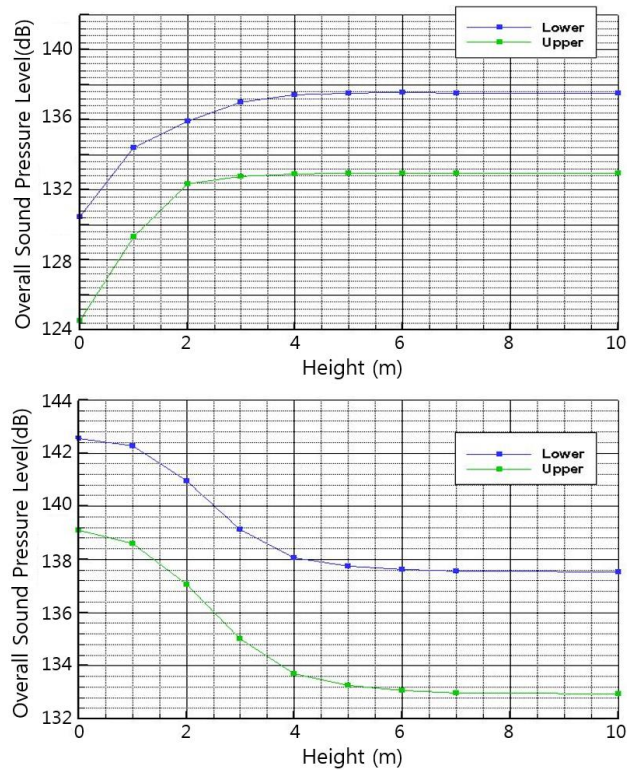
Fig. 2.18. Prediction results for OASPL depending on the height
(Upper: without a canister, Lower: with a canister)

In the upper graph of figure 2.18, the prediction results of the general case where the canister effect is not taken into consideration, the acoustic loading has the largest value at the initial launch (H = 0m). And it can be seen that as the height of the vehicle increases, the acoustic loading decreases and it is almost constant from about 6m. The result of the decreasing acoustic loads according to the altitude is a typical phenomenon that occurs when a vehicle is launched, because it depends on the distance between the noise source / receiver and the directionality of source depending on the geometry. In this case, the 7th to 12th sources are dominant sources having large acoustic power. These dominant noise sources excite the largest acoustic loading to the vehicle at the initial launch (H = 0) due to the directivity of sources. However, as the height of the vehicle increases, the dominant sources have an angle of 180 ° with the receivers and its influence is reduced, so the acoustic loading on the vehicle is hardly changes.

On the other hand, In the real launch environment as shown in figure 2.13, the vehicle is inside the canister. So the diffraction effect should be caused by the obstacle between the source and the receiver. If the thin screen model is applied as in the lower one of figure 2.17, it can be seen that the tendency is different from the previous results like the lower one of figure 2.18. Contrast to the conventional one, having a largest acoustic loading at the initial launch (H=0), this model has the smallest acoustic loading at the

initial launch and it increases as the height is increased. This is because the distributed noise sources are most greatly mitigated by the canister at the initial launch. Figure 2.19 shows the geometrical relationships of receivers, canister, and source when the height is 0m and 3m, respectively. It can be seen that the most noise sources are influenced by the canister and therefore have the smallest acoustic loading when the flight height is 0m.
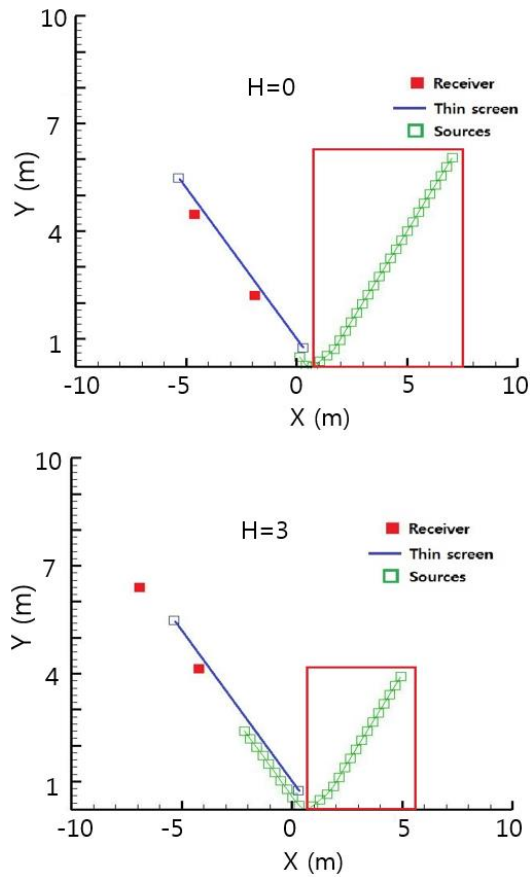
Fig. 2.19. Noise sources affected by canister diffraction
(Upper: H=10m, Lower: H=3m)
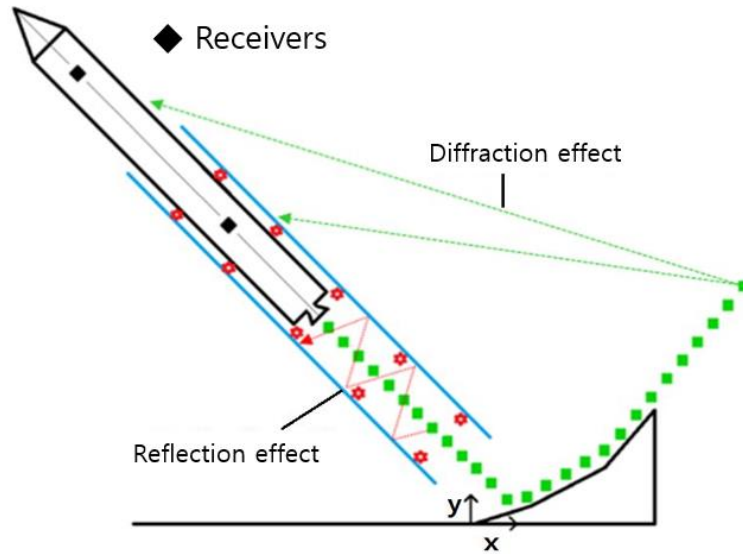
Fig. 2.20. Configuration of source distribution with consideration of reflection effect

In addition to the diffraction effect, sound reflection effect is induced by sources inner the canister, and this causes the acoustic loading on the vehicle to increase. Figure 2.20 shows the situation of the vehicle influenced by the effects of both diffraction and reflection at a height of 4 m. As described before, we applied the image model to the sources in the canister, and the prediction result of OASPL is shown in figure 2.21. The OASPL with the reflection effect has the lowest value at the instant of take-off which is same in the previous case, owing to the diffraction effect by the canister. However, as the vehicle goes up, the values of OASPL increased more than the only-diffraction case, because the number of sources influenced by the reflection
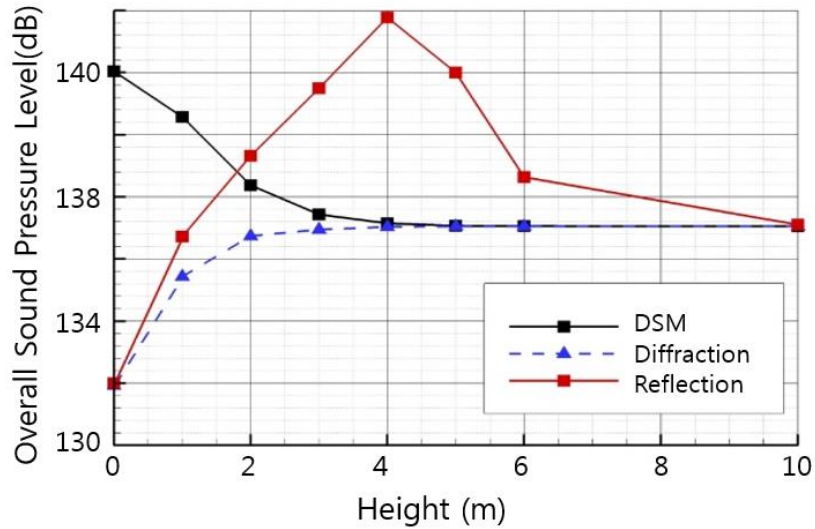
Fig. 2.21. Prediction results for considering reflection effect comparing with only-diffraction effect in terms of OASPL by height

effect inner the canister increases because of the formation of image sources that lead to an increase in the acoustic loads. While in the only-diffraction case, the value tends to converge toward that for a free jet near a height of 4 m, in the reflection case, convergence to that value happens after a height of 6 m, owing to the remaining reflection effect.

On the other hand, the importance of including the reflection effect is especially evident in the shape of the spectrum. Generally, the original empirical method based on DSM-II has only smooth-shaped sound spectrum owing to its inherent nature like figure 2.10. However, as shown in figure 1.3, the shape of the real spectrum of the missile in canister has local peaks, because it's launch environment. To make the sound spectrum have local

peak, Campos[23] utilized DSM-I instead of DSM-II as described before. Although the prediction result of DSM-I shows good agreement in the aspect of OASPL, the shape of the spectrum is so unrealistic as shown in figure 1.3. In this regard, our method considering reflection effect by image source model is a good alternative to DSM-II. As described before, we regard the sources in the canister as reflection sources that generate image sources, this leads to a realistic spectrum by considering the difference in phase that is not considered in DSM-II. Although the launch environment of Campos is not exactly the same as in our case, it is clear that employing the image source model make the spectrum have local peaks can improve the reliability in predicting the acoustic loads of a vehicle in canister.
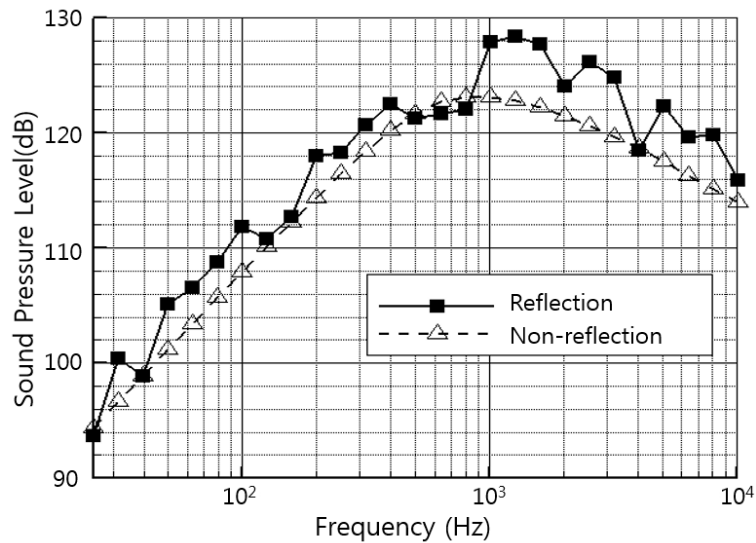
Fig. 2.22. Spectrum of considering reflection effect (1/3 Octave band)

2.3   Improved Empirical Method – Impinging Jet Model

The second improved empirical method is to consider additional impingement source directly depending on the height, which is called additional source with distributed sourced method(ASDSM). In previous studies, there were attempts to consider the impingement source to the DSM. However, these methods have disadvantages in that the analysis procedure is unclear[6, 37] or limited to only a few cases, and it is difficult to simulate the entire acoustic field depending on the height[80]. In this section, we first review the acoustic characteristics of supersonic impinging jet and the impinging jet model(ASDSM) is examined. Then, we perform validation on several cases using ASDSM and discuss how ASDSM will be used in launch pad optimization in Chapter 3.

2.3.1   Supersonic Impinging Jet Noise

Flow fields of supersonic impinging jet are complicated[81-83] and the induced acoustic waves are more complex. In general, the flow structure is classified into three regions such as main jet, impingement and wall jet and it indicates that there are at least three types of acoustic waves shown as figure 1.9[46]: (i) Mach waves generated from the shear layer of the main jet, (ii) acoustic waves generated from the impingement region, and (iii) Mach waves generated from the shear layer of the supersonic flow

58

downstream of the jet impingement. For the acoustic component of (ii), acoustic waves from impingement region, the well-known one is the high-frequency screech tone noise[84-86]. It is generated by feedback loop of acoustic waves from the supersonic impinging jet upon lift-off. However, as mentioned before, typical rockets do not have such tonal characteristics but have the broadband noise component dominantly. In this respect, we will look at the features of broadband noise component which are the Mach wave from the main jet and wall jet and the acoustic wave from the impingement region in the following section.

2.3.1.1   Mach Wave from Main Jet and Wall Jet

Like the free jet case (Section 2.1.1.1), the Mach wave is also known as the dominant component of supersonic impinging jet noise [19, 23, 46]. In the impinging jet case, Mach waves are generated by the main jet flow and the wall jet region maintaining supersonic flow like figure 1.9. Because these Mach waves play an important role in the launch environment, Tsutsumi et al.[19, 20, 87] studied the designing low noise launch pad considering these Mach wave radiation. On the other hand, since the characteristics of these Mach waves are well known due to their same characteristics as the free jet case, there is a great interest in the noise source generated in the impingement region recently.

59
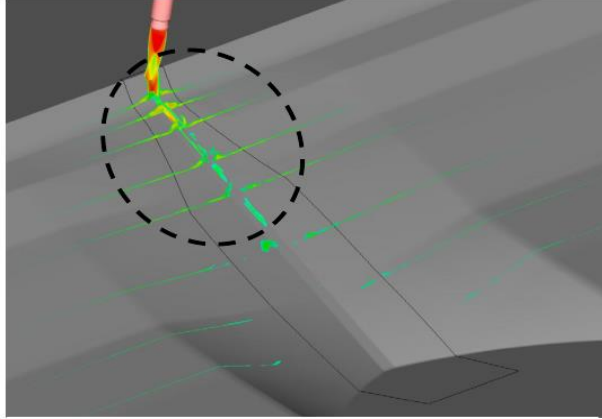
Fig. 2.23. Supersonic wall jet region[87]

2.3.1.2 Acoustic Wave from Impingement Region

Although the Mach wave is dominant in the supersonic imping jet, the acoustic waves from impingement region are also major concern. In terms of overall acoustic power of supersonic jet, the imping cases do not radiate more acoustic power than the free jet cases because the Mach wave which has dominant influence on the acoustic power is less generated. Generally, we think that the acoustic power of the imping jet is larger than the free jet, but this is the case for only subsonic jet. In the case of supersonic jet, the older researchers[88] found that the collision between the main jet and the deflector reduces the overall radiated acoustic power, because the supersonic region that generates the Mach wave is reduced and the supersonic jet flow is diffusing or spreading. However, in recent years, through many experiments conducted with more sophisticated equipment

60
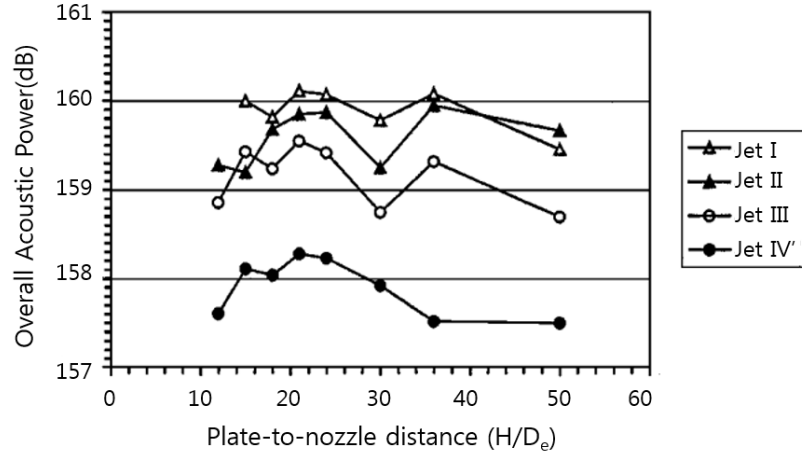
Fig. 2.24. Integrated overall acoustic power of the four jets according to
the plate-to-nozzle distance[34]

ONERA researchers[6, 26, 31, 34, 36] has reported that the radiated overall
acoustic power of the supersonic impinging jet is nearly constant regardless
of the height of impingement. It means that there are additional acoustic
waves generated by the impingement that compensate for the acoustic power
loss of the Mach wave. That is, this additional noise source is so important
that we need to examine this source specifically.

Numerous experimental and numerical studies have been carried out[46,
89-92], but the phenomenon is so complex that the generation mechanisms
of these acoustic waves have not been known completely.   However, there
are some obvious features of this noise source. First, the rocket plume near
the impingement region is supersonic, so the plate shock is generated which
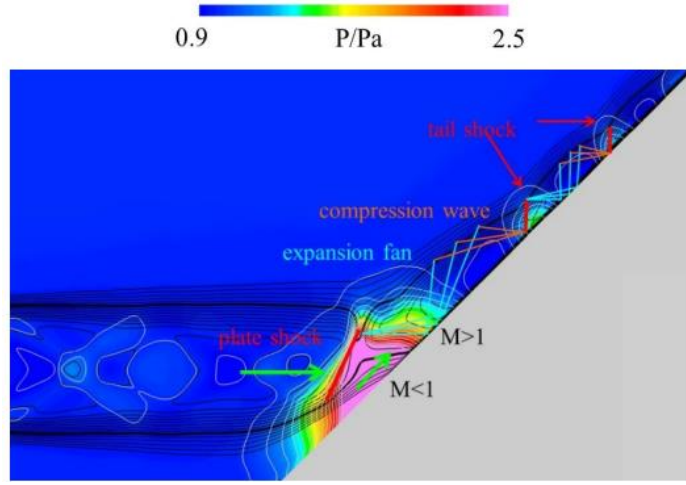
Fig. 2.25. Flow structure near the impingement region[89]

forms a shock cell structure along the launch pad. Second, the acoustic waves from impingement region do not have tonal characteristics [46, 91] but have broadband characteristics that have relatively dominant in high-frequency range than the Mach waves. Several practical simulations [89, 91] revealed the correlation between hydrodynamic structure and the acoustic field and confirmed that the acoustic waves from the impingement region are affected by the interaction of shock cell structure and turbulent structure of the shear layer. Therefore, considering all these points, we can regard this noise source as BSAN (broadband shock-associated noise) which is generated by the interaction of turbulent and shock structure and whose value is dominant in high-frequency range.

In general, the BSAN component of the supersonic free jet noise considers the two elements of interaction which are sound and shock interaction and vortex and shock interaction. For these element, the BSAN has all the components of monopole, dipole, and quadrupole terms having potential contribution to the far field sound and these components are all known as important role in BSAN [93]. Which noise component is dominant depends upon a situation. Brehm et al.[94] identified the impingement source based on the flow field and the acoustic wave propagation pattern. It revealed that there is contribution of large dipole at impingement source region. And many researchers [45, 76, 95] studied the location of effective region of impingement source. In this thesis, based on recent research[89, 91, 94], it is defined as the circle region within $2D_e$ from the impingement region.

To sum up, acoustic waves generated in the impingement region are considered BSAN generated by the interaction between shock cell and turbulent structure. To accurately model these acoustic waves, monopole, dipole and quadrupole should be used. However, the recent numerical studies show that the BSAN in the impingement region is very complicated, unlike the general free jet case, and the generation mechanism has not been known completely. However, the dipole can be introduced as a dominant source with the directivity pattern of acoustic waves radiated in a direction perpendicular to the impingement surface. The exact position of the dipole

source is also unknown, but it can be placed at a position away from the first shock cell formed along the launch pad surface.

2.3.2   Impingement Source Model

Based on the features described above, we have modeled an impingement source that can be applied to the original DSM only reflecting the turbulent mixing noise. In this procedure, the underlying assumptions are as follows.

i)   The acoustic efficiency of supersonic impinging jet is constant with height and the power is divided into turbulent mixing noise(W_{DSM}) and impingement source(W_{imp}).

ii) The impingement source can be modeled as BSAN which is dominant in high-frequency range that is affected by the shock and turbulent shear layer near the impingement region.

iii) The magnitude of the impingement source is equal to the power of the turbulent mixing noise, which is lost compared to the free jet depending on the impingement height.

iv) It can be modeled as a dipole source considering the directivity and previous research of source identification.

Then, we can apply an additional impingement source directly to the DSM-II. The added impingement source has four characteristics: location,

64

power, spectrum, and directivity to be applied to the DSM-II. Therefore, if we obtain the four characteristics of impingement source as above, we can apply impingement source by the following equation (2.20).

$$SPL_{imp,b,p} = L_{imp,s,b} - 10\log\left(r_{imp,p}^{\ 2}\right) - 11 + DI(b, \theta_{imp,p}) \qquad (2.20)$$

$SPL_{imp,b,p}$ is the sound pressure level (dB) contributed by the impingement source at the observer location, $L_{imp,s,b}$ is the sound power level for each frequency band of the impingement source, $r_{imp,p}$ is the distance from the impingement source to the observer position, and $DI(b, \theta_{imp,p})$ is the directivity index that depends on the geometric relationship between the source and the receiver. In the next section, we will look at the four characteristics of the impingement source.

2.3.2.1 Power of Impingement Source

The power of the impingement source is determined by the impingement height, which is the distance from the nozzle to the plate. Intuitively, it is generally assumed that the closer the impingement distance is, the larger the power of the impingement source. However, as mentioned above, the acoustic phenomenon of the supersonic impinging jet is not the same (this will be discussed in the next validation Section 2.3.4). Impingement source is modeled as a BSAN whose magnitude is proportional not only to the

65

Table 2.2. Three characteristic lengths of supersonic jet

Characterisitc length		Description	Equation
L_T	Laminar core length	Region of having the same velocity at the nozzle exit	$L_T = 3.45 D_e (1 + 0.38 M_e)^2$
X_p	Power peak location	Maximum interaction of turbulent and shock structure	$X_p \sim 1.8 L_T$
X_s	Supersonic length	Region of jet flow having supersonic velocity	$X_s = 6.5 M_e^{1.5} \dfrac{L_T}{3.45(1 + 0.38 M_e)^2}$

intensity of the shock but also to the turbulence intensity. Therefore, it is necessary to examine three characteristic lengths to obtain the power curve of the impingement source according to the distance plate-to-nozzle distance. The descriptions and equations from the reference papers[22, 96] for the three characteristic lengths are obtained and shown in Table 2.2.

First, the laminar core length(L_T) is the section that maintains the supersonic laminar core. Since the flow velocity in this region is the same as the nozzle exit, the shock intensity of the impingement region is max. After the laminar core structure breaks, and the intensity of the large turbulent structure becomes stronger and the maximum noise is generated in the region, peak power location(X_p). And the supersonic length(X_s) is the region of jet flow having supersonic velocity, making the shock near the impingement region.

The dipole acoustic power of the impingement source can be expressed as follows by simplification[96].

66

$$W_{imp} = \frac{1}{12\pi} \frac{1}{\rho_0 a_0^{\,3}} \overline{\left(\frac{\partial \tilde{F}}{\partial t} \right)}^2 \tag{2.21}$$

Where ρ_0 is ambient density (kg/m³) and $\overline{\left(\dfrac{\partial \tilde{F}}{\partial t} \right)}$ is the rate of change of

the fluctuating force (N/s) simplified as following equation (2.22).

$$\overline{\left(\frac{\partial \tilde{F}}{\partial t} \right)} = 2\pi f_c \tilde{F} \tag{2.22}$$

Where f_c is the characteristic frequency (Hz) of the fluctuation from

BSAN normalized spectrum[97] and the fluctuating force (N) $\tilde{F}$ can be

simplified as following equation (2.23).

$$\tilde{F} = \tilde{p} \times A_c \tag{2.23}$$

Where $\tilde{p}$ is the pressure (Pa/m³) under the impinging jet from BSAN

pressure[98] and A_c is the correlation area (m²) from BSAN diameter

relation[96]. From these relations we can calculate each value at the three

points at the initial jet($0.1L_T$), the peak power location(X_p), and the

supersonic tip(X_s). In order to obtain the relative acoustic power of the

impingement source, the acoustic power of free jet noise(W_{free}) for the

supersonic jet as the turbulent mixing noise considered in the DSM is

expressed by the following equation (2.24)

67

$$W_{free} = 0.0017 \rho_e A_e U_e^{\,3} \tag{2.24}$$

And the relative sound power level($L_{imp,s}$) of the impingement source (dB) can be obtained from that of DSM(L_{DSM}) by following equation (2.25) based on the reference acoustic power (W_{ref}, ref: $10^{-12}W$)

$$L_{DSM} = 10\log\!\left(W_{free}/W_{ref}\right) \tag{2.25}$$

The results of parameters of dipole model at three critical points are obtained in Table 2.3. From these results, we can obtain the fitted curve of relative sound power level of the impingement source according to the nozzle-to-deflector distance as shown in figure 2.26.

Table 2.3. Dipole model parameters and relative acoustic power of impingement source to turbulent mixing noise at three points

	① 0.1X$_t$	② X$_p$	③ X$_s$
f_c	$1.0 \times U_j / D_e$	$1.0 \times U_j / D_e$	$1.0 \times U_j / D_e$
$\widetilde{p}$	$0.005 \times \left(0.5\rho_j U_j^2\right)$	$0.25 \times \left(0.5\rho_j U_j^2\right)$	$0.31 \times \left(0.5\rho_j U_j^2\right)$
A_c	A_e	$0.28 A_e$	$0.15 A_e$
W_{imp}	$0.16 W_{DSM}$	$0.96 W_{DSM}$	$0.08 W_{DSM}$
$L_{imp,s}$	$L_{DSM} - 8dB$	$\approx L_{DSM}$	$L_{DSM} - 10dB$
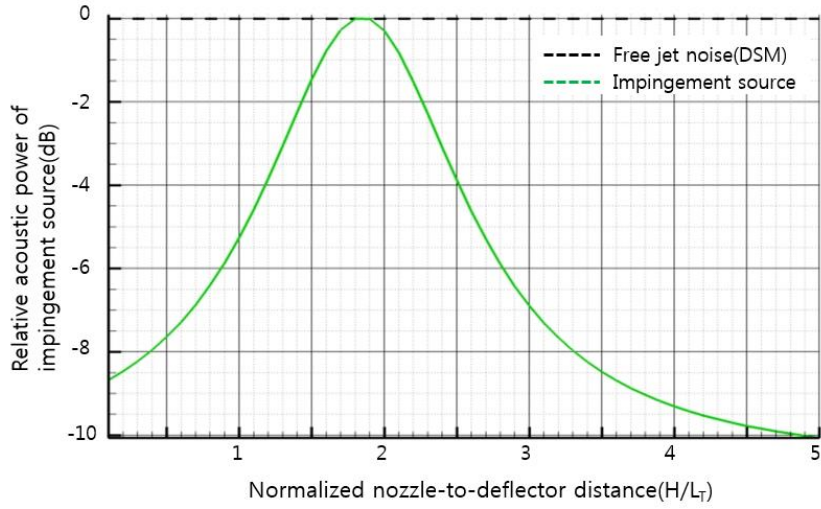
Fig. 2.26. Relative sound power level curve of impingement source

2.3.2.2 Spectrum of Impingement Source

The spectrum of the impingement source related to the first term of equation (2.20) can be determined by Olsen's dimensionless power spectral density function[99] about the impingement-only noise source like figure 2.27.
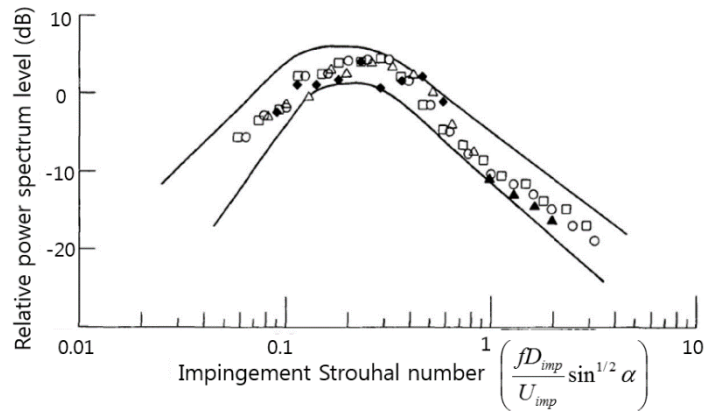
Fig. 2.27. Impingement-only source power spectrum[99]

69

The impingement Strouhal number (St_{imp}) is defined from equation (2.26).

$$St_{imp} = f \frac{D_{imp}}{U_{imp}} \sin^{1/2} \alpha \qquad (2.26)$$

α is the angle of impingement, D_{imp} and U_{imp} are the impingement diameter and velocity, respectively, and each is obtained by multiplying impingement coefficients by the exit parameter as following equations (2.27-28)

$$D_{imp} = c_{D,imp} D_e \qquad (2.27)$$

$$U_{imp} = c_{U,imp} U_e \qquad (2.28)$$

The impingement coefficients of diameter and velocity are obtained by fitting experimental data[99, 100] and are function of impingement height, exit diameter, and exit Mach number.

$$c_{D,imp} = f(H, D_e, M_e) \qquad (2.29)$$

$$c_{U,imp} = f(H, D_e, M_e) \qquad (2.30)$$

Then, the power spectral density function of the impingement source of figure 2.27 is applied as the spectral term of equation (2.20) through the following relation (2.31).

$$L_{imp,b} = L_{imp,s} + L_{imp,DPSD_C} - 10\log\left(\frac{U_{imp}}{D_{imp}}\right) + 10\log\Delta f \qquad (2.31)$$

Sound power level of the impingement source($L_{imp,s}$) is obtained as described in the Section 2.3.3.1. The value of $L_{imp,DPSD_C}$ is obtained from the power spectral density and represents the y-value corresponding to the impingement Strouhal number of the x-axis in figure 2.27.

2.3.2.3 Directivity and Position of Impingement Source

Directivity and position of an additional impingement source are determined relatively simply. The maximum radiation direction of the impingement source is known to be nearly perpendicular to the wall[46, 90, 91] of the deflector, but the specific directivity index is not known. So, We employ the Eldred's directivity[22] index corresponding to the large Strouhal number similar to that of BSAN and make it have maximum directivity in the direction perpendicular to the deflector surface. The modified directivity of Eldred to be used for the impingement source is shown in figure 2.28 and its value is used for directivity term in the equation (2.20).

On the other hand, as described before, the exact position of additional impingement source is somewhat ambiguous because it cannot be confined to exactly certain region. In order to place the impingement source, we have
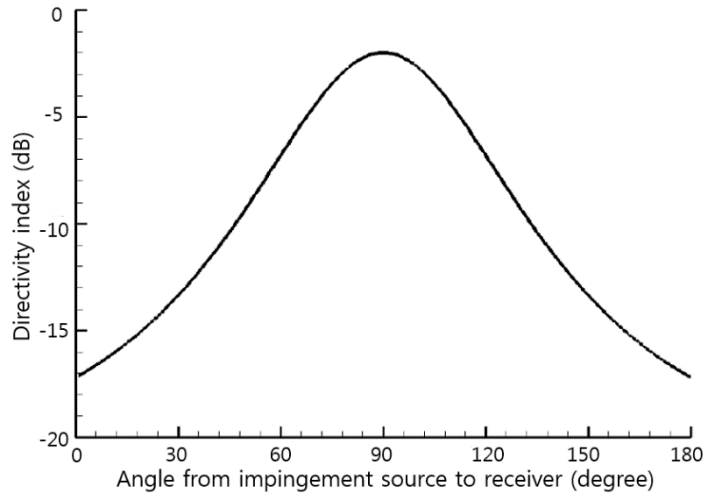
Fig. 2.28. Directivity index of the impingement source

  to define the valid region for the impingement source. Many researchers [45, 76, 95] studied the location of effective region of impingement source of their own. In this thesis, based on recent research[89, 91, 94], it is defined as the circle region within $2D_e$ from the impingement region.

2.3.3   Additional Source with Distributed Source Method(ASDSM)

In this section, we will apply the second improved empirical method which is the impinging jet model called additional source with distributed source method (ASDSM) to the several launch cases and examine its effect.

   As described before, the conventional DSM only considers the turbulent mixing noise as the dominant noise source, it was difficult to predict the upstream noise of the supersonic impinging jet only by deflecting the jet

flow axis. So the researchers overly assume the acoustic efficiency (1%) to cover the real physics and increase the prediction accuracy. However, due to the inherent feature of low-frequency dominant spectrum of the TMN, there were underestimation problems in the high-frequency range. However, when using ASDSM, it is possible to improve the accuracy in the upstream direction due to the additional noise source near the impingement region as BSAN. In this case, it can cover the realistic physics by impingement source so the acoustic efficiency can be determined more realistic value. A schematic illustration of the ASDSM is given in figure 2.29. Also, the ASDSM can simulate the acoustic fields more realistically along the height by changing the characteristics of the impingement source. To confirm this improvement, the second improved empirical method will be validated in the next section. After validation is complete, it can be applied to the recent state-of-art studies of optimization of low noise launch pad that were mainly attempted by the numerical method.

Real case: all physics are included
($\eta = k\%$)

DSM: only TMN(W_{DSM})
$\rightarrow$ Over-estimation ($\eta = 1\%$)

ASDSM: TMN(W_{DSM}) + BSAN(W_{imp})
$\rightarrow$ Realistic estimation ($\eta = k\%$)
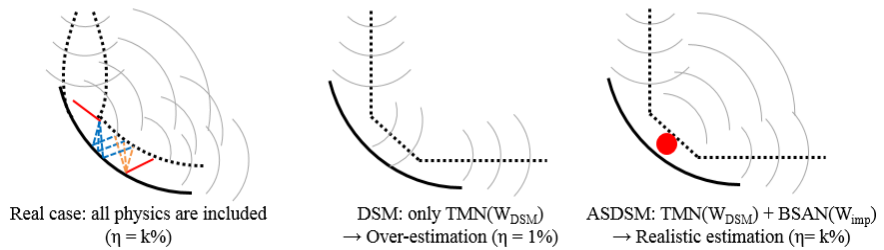
Fig. 2.29. Schematic illustration of ASDSM compared with DSM

2.3.4   Validations and Results

We validated the ASDSM for four launch cases. As a result of the application of ASDSM, we can confirm the following effects for each case. For case 1 and case 2, the accuracy of prediction in the high-frequency range is improved. And for case2 and case 3, due to the additional impingement source, the contour of the entire acoustic field changes and the directivity of the far field is improved. In case 4, we simulate the acoustic field according to the nozzle-to-deflector distance and compare it with the experimental results. We can confirm that ASDSM is more accurate than original DSM in all aspects such as OASPL, spectrum, and directivity for all heights.

2.3.4.1   Case1: KSR-III

The first validation case is Korea sounding rocket-III (KSR-III) based on the study of Park et al. [101]. The specification of KSR-III is presented in table 2.4. For the launch pad configuration[102] as shown in figure 2.30, the noise sources of DSM and additional impingement source are arranged along the jet axis and the receiver position is shown in figure 2.31. Twenty-seven sources were placed by DSM-II and the impingement source was placed in the impingement region between the fourth and fifth sources.

Table 2.4. Specification of KSR-III rocket[101]

Parameter	Value
Acoustic efficiency (%)	0.62
Nozzle exit diameter (m)	0.696
Exit Mach number	2.2
Engine thrust (N)	117,000
Receiver position (m)	(0, 13.2)
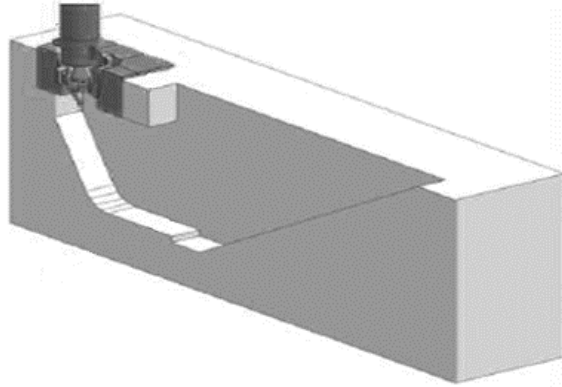
Fig. 2.30. Launch pad configuration of KSR-III[102]
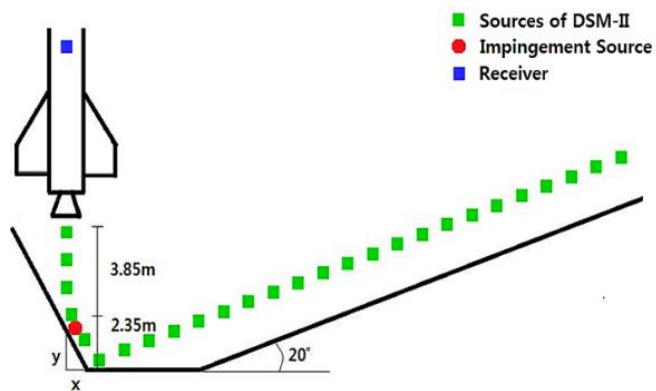
Fig. 2.31. Schematic sketch of distributed source and receiver of KSR-III

Table 2.5. Information for impingement source power of KSR-III

Parameter	Value
Normalized impingement height (H/L_T)	0.48
Relative sound power level ($L_{DSM} - L_{imp,s}$)	7.7 dB
Sound power level of DSM sources (L_{DSM})	176.3 dB
Sound power level of impingement source (L_{DSM})	168.6 dB

The nominalized length(H/L_T) for a impingement height of 3.75 m is 0.48. With this value, from the figure 2.26, we can obtain the information for impingement source power of KSR-III as listed in table 2.5. On the other hand, the spectrum of the impingement source obtained from section 2.3.2.2 is shown in figure 2.32. The spectrum has peak frequency around 400 Hz and it means that the impingement source is modeled as a BSAN with a dominant value in the high-frequency range.
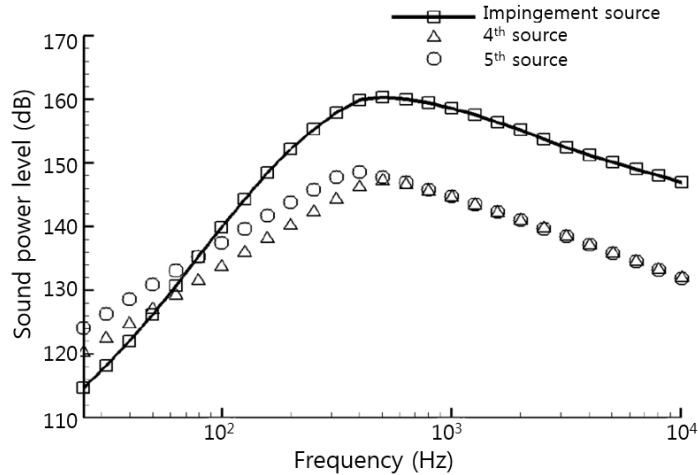
Fig. 2.32. Spectrum of the impingement source (1/3 octave band)

region than a typical DSM source. Figure 2.33 shows the results of prediction on the receiver in terms of sound spectrum. Compared with the experiment, the prediction result with DSM-II was underestimated in terms of OASPL. And in terms of spectrum, it showed the problem of underestimation in high-frequency range. On the other hand, we can find that the prediction result with ASDSM matches more closely with the experimental data in terms of spectrum as well as OASPL. This is due to the additional impingement source of ASDSM, which is modeled as BSAN having large value in the high-frequency range, and it shows that ASDSM can make great improvement in predicting the acoustic loading in terms of spectrum as well as OASPL.
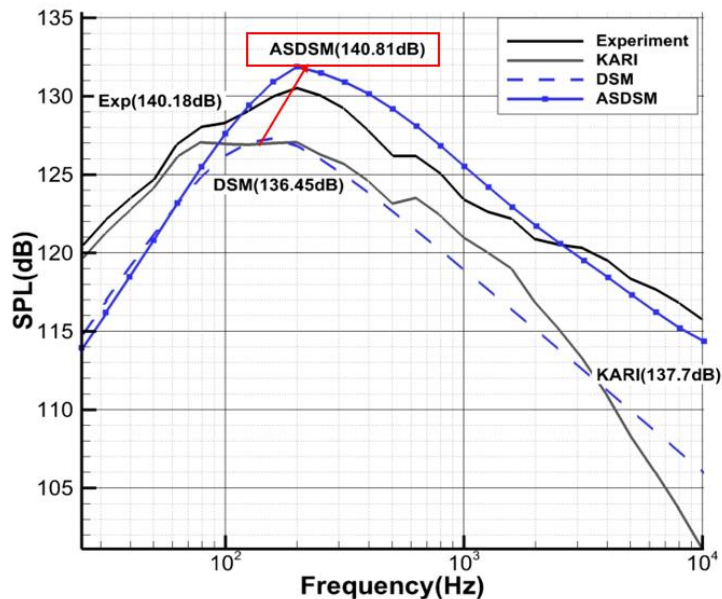
Fig. 2.33. Comparison of ASDSM with experiment and DSM-II for
KSR-III (1/3 octave band)

2.3.4.2 Case2: NARO

Next validation case is Korea space launch vehicle-I (KSLV-I), which is called NARO, based on the study of Choi et al.[30]. The specification of NARO is presented in table 2.6. For the launch pad configuration, the noise sources of DSM and additional impingement source are arranged along the jet axis. And the information for impingement source power of NARO is listed in table 2.7.

Table 2.6. Specification of NARO rocket[30]

Parameter	Value
Acoustic efficiency (%)	0.5
Nozzle exit diameter (m)	1.45
Engine thrust (N)	1,667,000
Exit Mach number	2.9
Exit sound velocity (m/s)	1,031
Receiver position (m)	(0, 26.7)

Table 2.7. Information for impingement source power of NARO

Parameter	Value
Normalized impingement height (H/L_T)	0.79
Relative sound power level ($L_{DSM} - L_{imp,s}$)	6.5 dB
Sound power level of DSM sources (L_{DSM})	188.5 dB
Sound power level of impingement source (L_{DSM})	182.0 dB
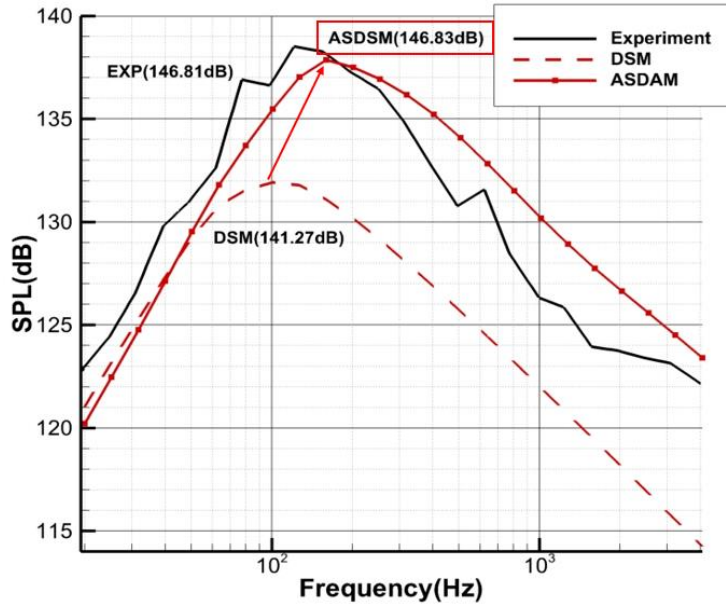
Fig. 2.34 . Comparison of ASDSM with experiment and DSM-II for
NARO (1/3 octave band)

Figure 2.34 shows the results of prediction for the NARO rocket in terms
of sound spectrum. We can find that the effects of ASDSM are similar to
that of KSR-III both in terms of OASPL and spectrum. The prediction
values of OASPL and peak frequency for KSR-III and NARO rocket are
summarized in table 2.8. Depending on the launch environment, the
difference of the sound power levels($\Delta L_{DSM-imp}$) between DSM sources
and impingement source are 7.7 dB and 6.5 dB, respectively. So the effects
of the impingement source on the OASPL results is greater for the NARO
rocket (+5.56 dB) than for the KSR-III (+4.36 dB).

Table 2.8. Summary of prediction results and effects of impingement

source on results for KSR-III and NARO rocket

Case		OASPL(dB)		f_{peak} (Hz)	
		Value	Error	Value	Error
KSR-III ($\Delta L_{DSM-imp}$ = 7.7 dB)	DSM-II	136.45	-3.73	125	-75
	ASDSM	140.81	+0.63	200	0
	Experiment	140.18	-	200	-
NARO ($\Delta L_{DSM-imp}$ = 6.5 dB)	DSM-II	141.27	-5.54	100	-25
	ASDSM	146.83	+0.02	160	+35
	Experiment	146.81	-	125	-

In the aspect of spectrum, the ASDSM predicts the peak frequency to be 75Hz, 60Hz higher than the DSM-II for each rocket. It is similar trend of many previous studies[24, 32, 37, 43] to overcome the underestimation problem in the high-frequency range of DSM-II. In this regard, the ASDSM has the merits that it is more cost-effective and is relatively simple to include directly impingement source as compared with other studies.

On the other hand, the effect of impingement source on the OASPL result can be more easily confirmed through the OASPL contour comparison around the launch vehicle as shown in Figure 2.35. The OASPL contour of ASDSM clearly shows additional upstream emission of acoustic waves near the impingement region by an impingement source. This additional emission of the impingement noise source continues to be verified in real experiments and is a great help in simulating the actual acoustic field.
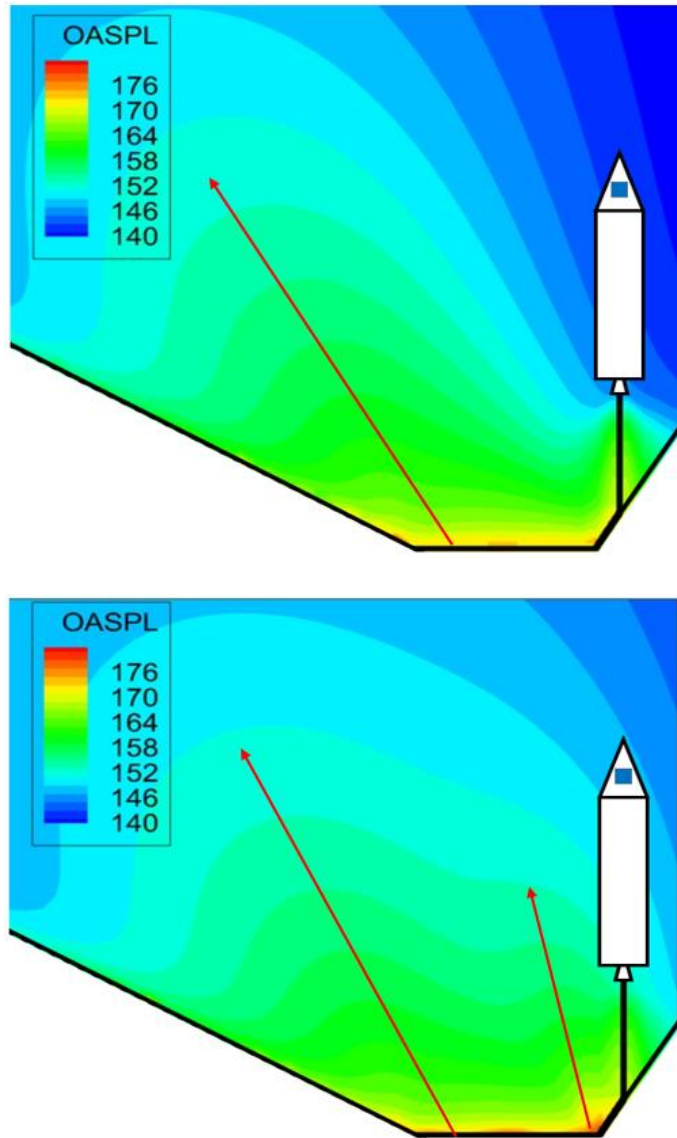
Fig. 2.35. Comparison of OASPL contour for NARO rocket

(Upper: DSM, Lower: ASDSM)

2.3.4.3 Case3: JATO

The third validation case is JATO rocket of NASA, based on the experimental study of Cole et al.[88]. In this validation case, we can also see the additional upstream emission of acoustic waves near the impingement region through the OASPL contour. And the prediction result about far-field directivity is compared with the experiment. For the JATO rocket, the specification and the information for impingement source power are presented in table 2.9 and 2.10, respectively.

Table 2.9. Specification of JATO rocket [88]

Parameter	Value
Nozzle exit diameter (mm)	66
Exit Mach number	3
Engine thrust (N)	4,532
Stagnation temperature (K)	1,615
Stagnation pressure (kPa)	6,239

Table 2.10. Information for impingement source power of JATO

Parameter	Value
Normalized impingement height (H/L_T)	0.33
Relative sound power level ($L_{DSM} - L_{imp,s}$)	8.2 dB
Sound power level of DSM sources (L_{DSM})	156.1 dB
Sound power level of impingement source (L_{DSM})	147.9 dB
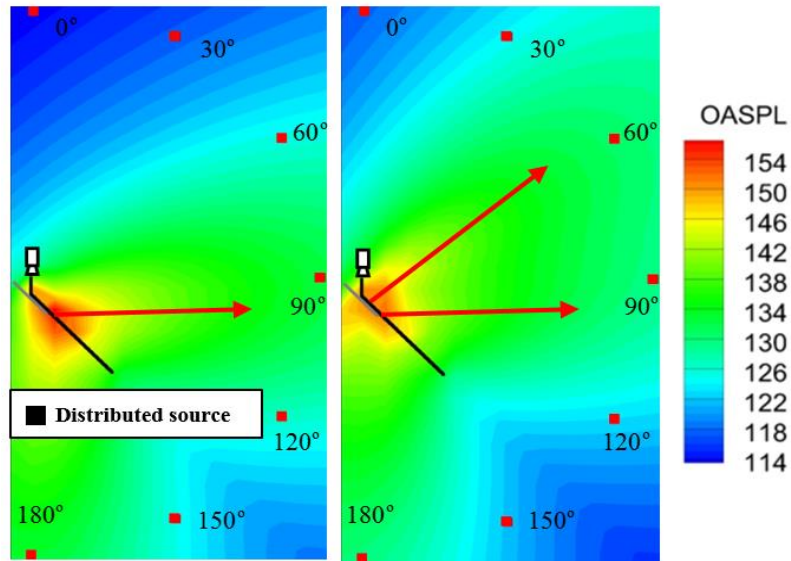
Fig. 2.36. Comparison of OASPL contour for JATO rocket

(Left: DSM, Right: ASDSM)
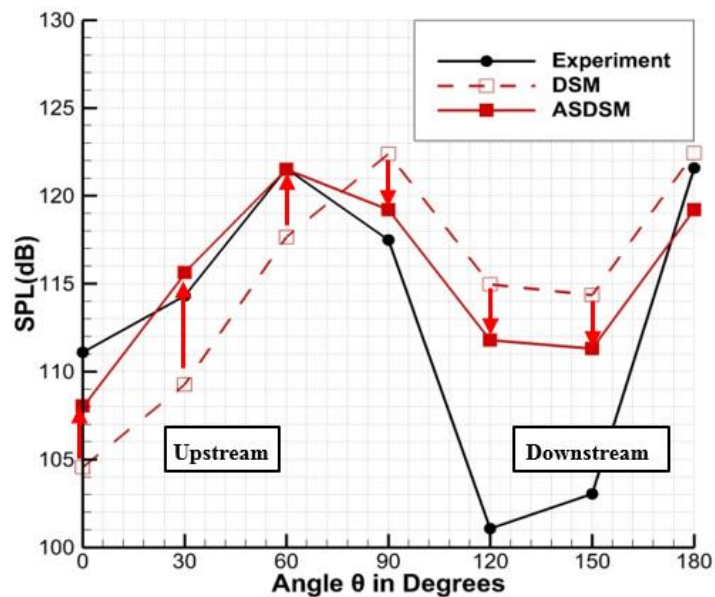
Fig. 2.37. Far-field directivity of JATO rocket[88]

In the figure 2.36, we can also find additional emission of the acoustic waves near the impingement region. And the effect of additional emission can be seen in the far-field($300D_e$) directivity of figure 2.37. ASDSM provides clearly better predictions than DSM for both upstream and downstream regions. This result again confirms that the impingement source is essential for simulating the actual acoustic field. On the other hand, the prediction results near the downstream (120, 150 degrees) has large error. This overestimating problem might be caused by atmospheric attenuation. In this case, the receiver points are distributed $300D_e$ away from the nozzle exit. For this far-field acoustic environment, the additional effects of atmospheric attenuation can be deal with in the future work.

2.3.4.4   Case4: Mach 1.8 ideally expanded jet

For the last validation case, we deal with the Mach 1.8 ideally expanded jet based on the study of Akamine et al.[92] In the previous validation cases, we confirmed that additional emission of acoustic waves near the impingement region is essential to simulate a realistic acoustic field. In this section, we will see how the ASDSM can simulate the actual acoustic field according to the height variation. Akamine et al.[92] did experiments how the acoustic field changes according to the heights. Experimental conditions are given in table 2.11.

Table 2.11. Specification of Mach 1.8 ideally expanded jet [92]

Parameter	Value
Acoustic efficiency (%)	0.38
Nozzle exit diameter (mm)	20
Exit Mach number	<u>1.8</u>
Stagnation pressure (MPa)	0.575 ± 0.01
Nozzle-plate distance (D_e)	5, 10, 15, 20
Plate angle (degree)	45

Table 2.12. Information for impingement source power of Mach 1.8 ideally expanded jet at H=5D_e

| Parameter	Value
Normalized impingement height (H / L_T)	0.64
Relative sound power level ($L_{DSM} - L_{imp,s}$)	7.1 dB
Sound power level of DSM sources (L_{DSM})	143.5 dB
Sound power level of impingement source ($L_{imp,s}$)	136.4 dB

Akamine et al.[92] noted that a high OASPL is observed where the distance is 40 D_e away from the impingement point and the angle is 75-degree from the plate. The experiment provided OASPL values only for this point, we will look at the results mainly with OASPL values for this point according to the height. First, at H = 5D_e, the information for impingement source power is shown in table 2.12. The sound power levels of DSM and impingement source are obtained as 143.5dB and 136.4dB, respectively.

Fig. 2.38. Comparison of acoustic fields for Mach 1.8 ideally expanded jet at H=5D$_e$ (Top: experiment, Middle: DSM, Bottom: ASDSM)

Table 2.13. Comparison of OASPL values at $H=5D_e$

Case	OASPL(dB)	
	Value	Error
Experiment	132	-
DSM	131.18	-0.82
ASDSM	133.64	+1.64

    The result of comparison of the OASPL values with the experiment and the predictions is shown in table 2.13. The ASDSM considers an additional impingement source to the DSM, which increases the prediction value of OASPL by 2.46dB. This effect can be described in the acoustic field contour in figure 2.38. The acoustic field of the DSM shows only propagation of turbulent mixing noise which is regarded as Mach waves in the wall jet region. On the other hand, the acoustic field of the ASDSM shows that there is an additional emission of acoustic waves near the impingement region as shown in the experimental acoustic field. In the case of $H = 5D_e$, the turbulent structure is less developed because the height is relatively small, so the acoustic power of the impingement source is modeled to be relatively small compared to that of the DSM. Therefore, it can be seen that the DSM component propagating downstream in the acoustic field of ASDSM is more dominant. The remarkable fact is that these phenomena and tendency also appear in the experimental acoustic field as well. We will look at whether this effect of ASDSM is valid for various heights.

Table 2.14. Information for impingement source power of Mach 1.8
ideally expanded jet at H=10D$_e$

| Parameter	Value
Normalized impingement height (H / L_T)	1.28
Relative sound power level ($L_{DSM} - L_{imp,s}$)	3.2 dB
Sound power level of DSM sources (L_{DSM})	142.6 dB
Sound power level of impingement source ($L_{imp,s}$)	139.3 dB

At H = 10D$_e$, the information for impingement source power is shown in table 2.14. The normalized impingement height is close to the point that generates maximum impingement source power ($H \approx 1.8L_T$) and thus the relative sound power level of impingement source has increased(139.3 dB) than H=5D$_e$ (136.4 dB). The result of comparison of the OASPL values is shown in table 2.15. Experiment shows that the OASPL value is increased by 3 dB compared to the previous case of H = 5D$_e$. On the other hand, the ASDSM increases the prediction value of DSM by 3.48dB, which makes the error less than the DSM.

Table 2.15. Comparison of OASPL values at H=10D$_e$

Case	OASPL(dB)		
	Value	Error	Difference from H=5D$_e$
Experiment	135	-	+3
DSM	131.36	-3.64	+0.18
ASDSM	134.84	-0.16	+1.2
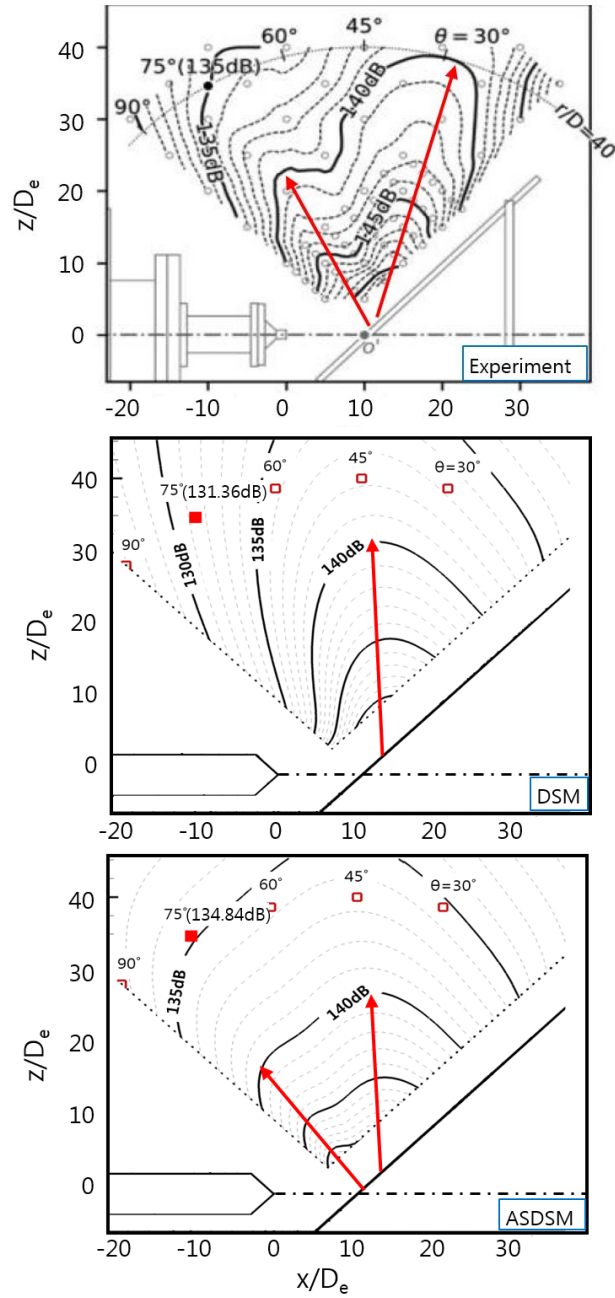
Fig. 2.39. Comparison of acoustic fields for Mach 1.8 ideally expanded jet at H=10D$_e$ (Top: experiment, Middle: DSM, Bottom: ASDSM)

Figure 2.39 shows the comparison of acoustic fields of each case for H=10D$_e$. As seen in the previous case, the DSM has only the turbulent mixing noise component generated from the main jet flow, whereas the ASDSM has the two dominant propagation directions which is similar as the experimental acoustic field. In this case, compared with H=5D$_e$, the higher impingement height changed the sound power of impingement source to be relatively strong, and thus the upward propagation becomes stronger. We can also see from the experimental result that these phenomena occurred. However, for the DSM, it is impossible to reflect this impingement effect, so only downstream propagation is observed in the acoustic field. Also, in the aspect of OASPL, DSM can predict the OASPL value relatively accurately when the height is low, but the error increases when the height is increased.

Next, for h = 15D$_e$, the information for impingement source power and the OASPL comparison results are shown in table 2.16 and 2.17.

Table 2.16. Information for impingement source power of Mach 1.8 ideally expanded jet at H=15D$_e$

Parameter	Value
Normalized impingement height (H / L_T)	1.91
Relative sound power level ($L_{DSM} - L_{imp,s}$)	0.03 dB
Sound power level of DSM sources (L_{DSM})	141.25 dB
Sound power level of impingement source ($L_{imp,s}$)	141.22 dB

In the table 2.16, the normalized impingement height is almost close to the maximum point ($H \approx 1.8L_T$) and thus the sound power level of impingement source is almost same (141.11 dB) as that of the DSM source (141.25 dB). In the table 2.17, as the height increases to 15De, the prediction result of DSM is -1.83dB less than before. This result is in consistent with the opinion of old researchers who misunderstood that the acoustic loading may have maximum value at the beginning of the launch and decrease as the height increase. However, recent research on the acoustic environment around the launch vehicle shows a different tendency [87, 92]. As can be seen from the results of this experiment, we can find that the OASPL of upstream region increases to some height. On the other hand, the ASDSM can overcome the shortcomings of the DSM as an impingement source, so that the tendency of prediction result can be made similar to the actual acoustic environment. This result can be visually confirmed with the propagation direction of the dominant acoustic source in each acoustic field in figure 2.40.

Table 2.17. Comparison of OASPL values at H=15D$_e$

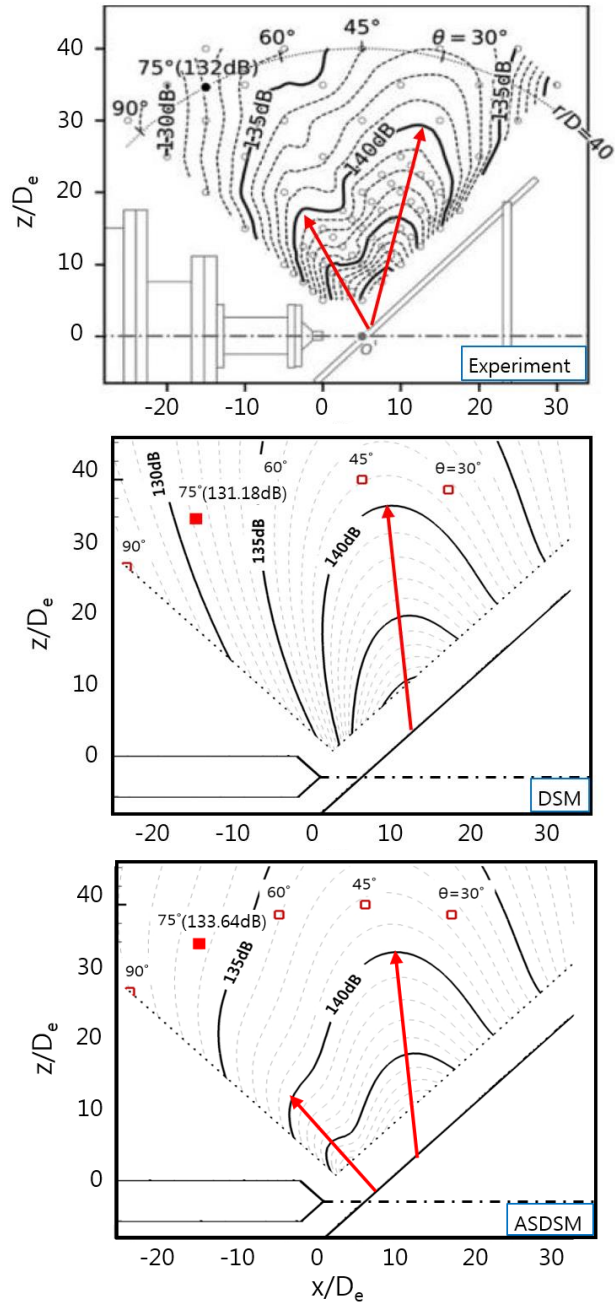| Case	OASPL(dB)		
	Value	Error	Difference from H=10D$_e$
Experiment	136	-	+1
DSM	129.53	-6.47	-1.83
ASDSM	135.38	-0.62	+0.54
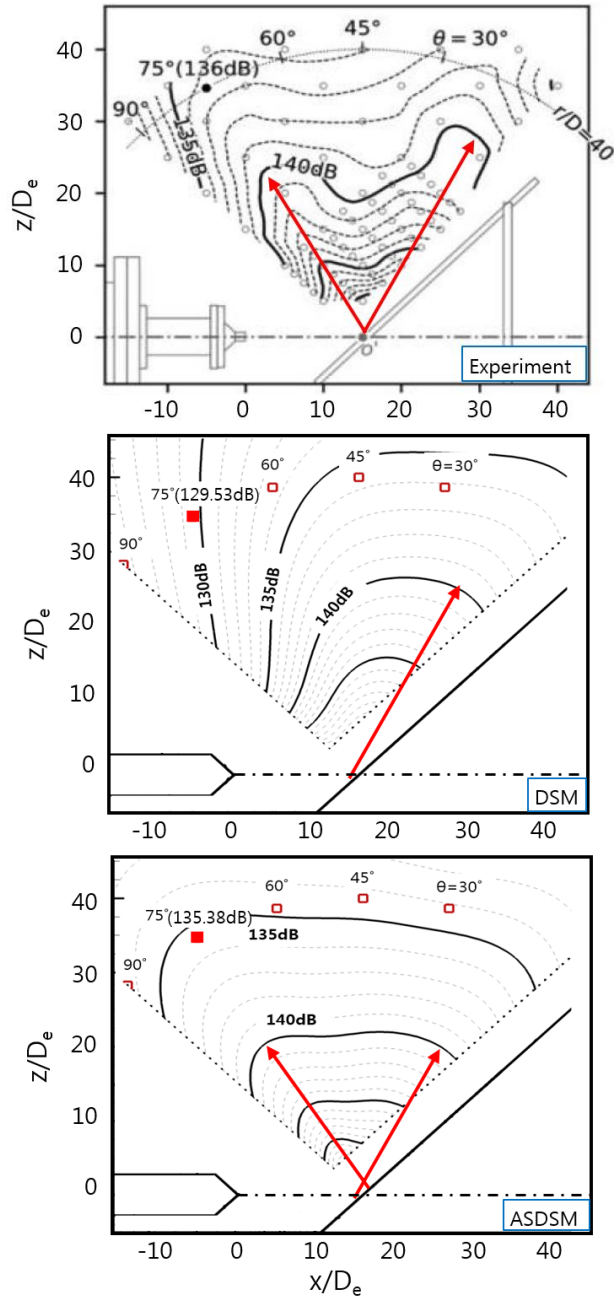
Fig. 2.40. Comparison of acoustic fields for Mach 1.8 ideally expanded
jet at H=15D$_e$ (Top: experiment, Middle: DSM, Bottom: ASDSM)

Table 2.18. Information for impingement source power of Mach 1.8 ideally expanded jet at H=20D$_e$

Parameter	Value
Normalized impingement height (H / L_T)	2.55
Relative sound power level ($L_{DSM} - L_{imp,s}$)	4.3 dB
Sound power level of DSM sources (L_{DSM})	142.9 dB
Sound power level of impingement source ($L_{imp,s}$)	138.6 dB

Finally, when H = 20D$_e$, the information for impingement source power and the OASPL comparison results are shown in table 2.18 and 2.19. As described before, the prediction result of DSM shows a larger error because it doesn't have the ability to consider the impingement phenomena. In particular, we can see in the acoustic field of figure 2.41 that the dominant propagation direction of DSM is very downstream, since the maximum noise source of the DSM is in the main jet region. On the other hand, as a result of the impingement source considerations, the ASDSM still simulates the entire acoustic field similar to the actual environment at H = 20D$_e$.

Table 2.19. Comparison of OASPL values at H=20D$_e$

| Case	OASPL(dB)		
	Value	Error	Difference from H=15D$_e$
Experiment	135	-	-1
DSM	127.77	-7.23	-1.76
ASDSM	134.05	-0.95	-1.33
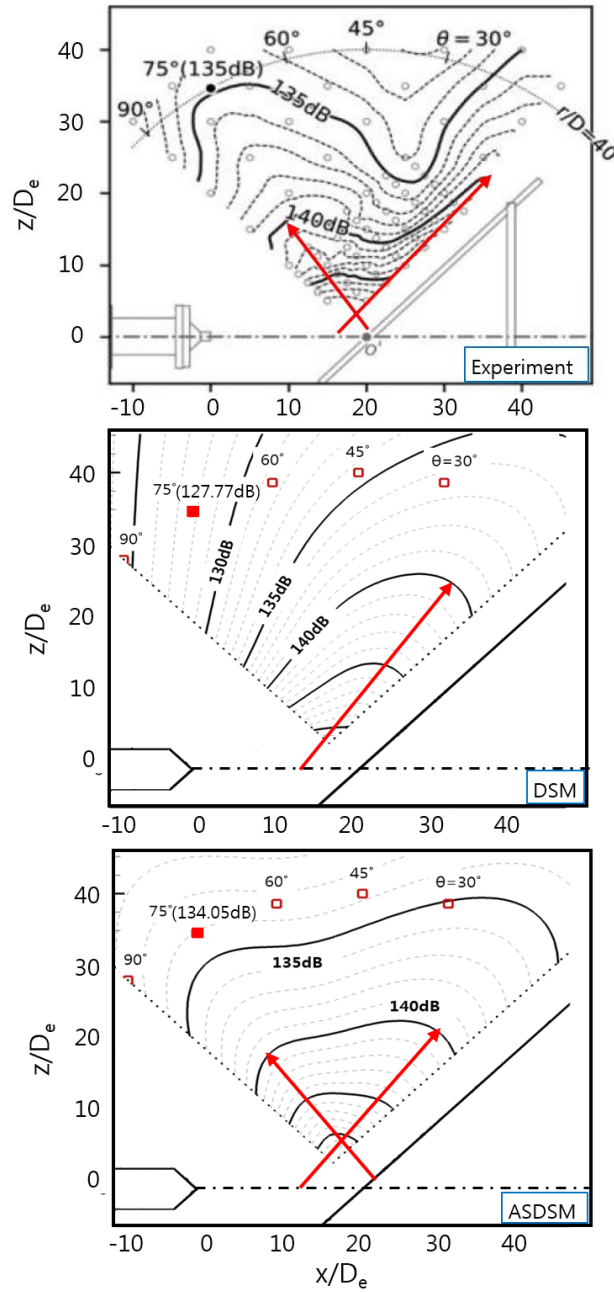
Fig. 2.41. Comparison of acoustic fields for Mach 1.8 ideally expanded
jet at H=20D$_e$ (Top: experiment, Middle: DSM, Bottom: ASDSM)
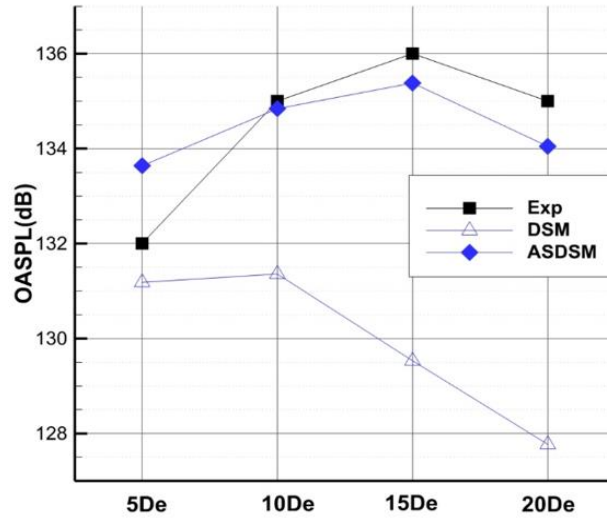
Fig. 2.42. Comparison of OASPL according to the impingement height

In figure 2.42, the OASPL values at the measurement point located 40 D_e away from the impingement point and 75 degrees from the jet flow direction are compared to the prediction results of DSM, ASDSM according to the height in figure 2.42. First, the experiment results have the smallest OAPSL value at the lowest impingement height ($5D_e$) and gradually increase to the maximum at $15D_e$. It is because the large turbulent structure is hardly developed at the lowest impingement height. So the acoustic power of the impingement source which is generated by interaction between the shock and the large turbulent structure is small. Then the dominant noise source are the Mach waves of the supersonic region jet flow existing along the deflector. Therefore, the prediction result of the DSM which is considering only the Mach wave of the turbulent mixing noise is not much different from

95

the experimental result. On the other hand, in the case of ASDSM, the OASPL value was supplemented by considering the additional impingement source and slightly overestimated. When examining the prediction results according to the height increase, the DSM which cannot consider the impingement source predict gradually less OAPSL value and the error also increase. On the other hand, the ASDSM models the impingement source with sound power level compared to the DSM source according to height as shown in figure 2.43. Therefore, the ASDSM can make predictions with similar trends to the experimentally measured OASPL values, as shown in figure 2.42. Through these cases, we can confirm that prediction results of ASDSM considering impingement source is reliable according to height.
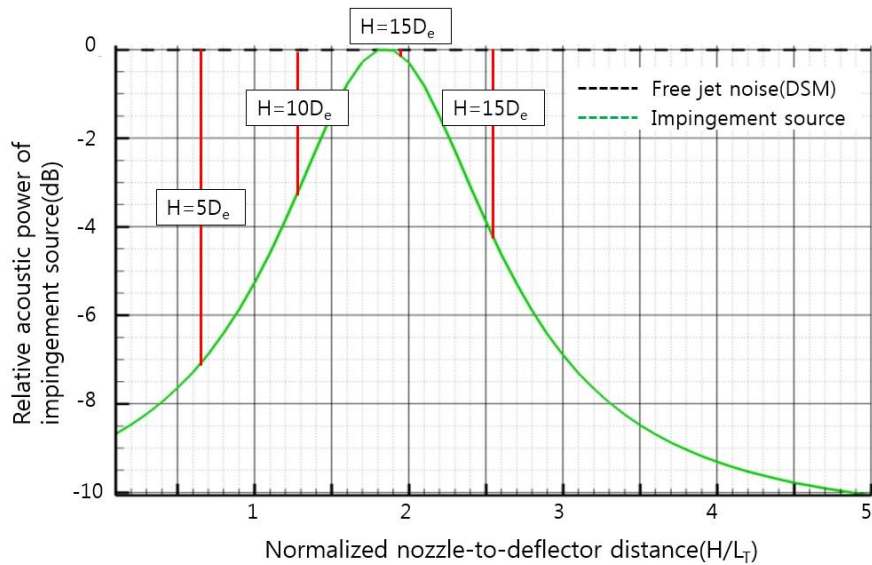
Fig. 2.43. Relative impingement source power modeled by height
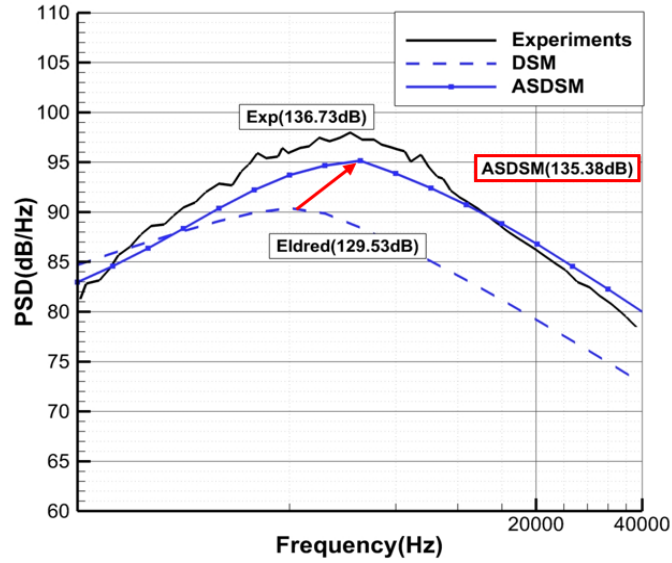
Fig. 2.44. Comparison of power spectral density spectrum at H=15 D$_e$

(1/3 octave band)

On the other hand, figure 2.44 shows the improvement of ASDSM prediction result in terms of spectrum of power spectral density when H = 15De. For this condition, where the normalized impingement height is 1.91 and the strong acoustic waves from the impingement region are generated, the prediction result of the DSM shows the limitation of underestimation in the peak frequency in aspect of spectrum as well as an error of about 7 dB in aspect of OASPL. On the other hand, the prediction result of ASDSM shows similar effects to validation cases 1 and 2 which complement the problem of underestimation in the high-frequency range as well as OASPL value.

2.4   Summary and Discussion

In this chapter we have developed two improved empirical acoustic prediction methods. First, we examined the disadvantages of the original empirical method along with the characteristics of supersonic jet noise. As a result, it is required to develop an improved empirical method considering diffraction and reflection effect by surrounding structures such as missile in canister, and an improved empirical method considering impingement effect due to collision between jet flow and launch pad in actual launch environment.

First, for the first improved empirical method, the diffraction effect and the reflection effect were applied by applying the Maekawa's diffraction model[47] and the image source model. In the verification case, the empirical method was used to predict the missile in canister. As a result, the effects of diffraction and reflection were confirmed by the surrounding structures. The canister surrounds the missile and acts as an obstacle between the acoustic source and the receiver, causing a diffraction effect which reduces the acoustic loading according to the geometric relation between the source, receiver and obstacle. In addition, the image source model was applied to the acoustic noise in the canister to apply the reflection effect, which increase the acoustic loading. Also, in the spectrum, the phase difference according to the distance between the original source and the

98

image source is considered, and it is confirmed that the inherent spectrum characteristic of the original empirical method, that is, the smooth-shaped spectrum shape appears as a spectrum having local peaks. These predictions are physically valid predictions of OASPL variation and spectrum according to the height, and it is confirmed that the surrounding structures in various launch environments can be considered properly in the future.

Next, the second improved empirical method is to add an impingement source near the impingement region which is not considered by the original empirical prediction method with the impinging jet model. This dissertation first investigated the characteristics of supersonic impinging jet noise. The first feature of supersonic impinging jet noise is the turbulent mixing noise component, which dominates the Mach wave in the supersonic flow region. This noise source is a dominant component of supersonic jet noise, and it is known that the original empirical method considers only turbulent mixing noise. The other component is a noise source having a large value in high-frequency range generated by interaction of the shock and large turbulent structure which is called broadband shock-associated noise (BSAN). In a situation where the supersonic jet collides with the launch pad, a shock cell structure is formed in the impingement region, which interacts with the surrounding turbulent structure to generate additional impingement source. Therefore, the impingement source is modeled with characteristics of BSAN

99

and applied to existing empirical method. In order to apply this impingement source, this dissertation proposed a method to obtain four characteristics of impingement: power, spectrum, directivity, and position. Then, we applied this method and performed validation for four cases. As a result of validation, many improvements were confirmed. First, in terms of OASPL, by considering the impingement source the prediction result of original empirical method is complemented and is improved. The consideration of the impingement source has also influenced the spectrum, improving the prediction accuracy in the peak frequency and also improving the problem of underestimation in the high-frequency range by overcoming the underestimation problem. Also, when the impingement source is considered, the additional acoustic propagation phenomenon in the upstream direction is observed in the impingement region due to the impingement source when the OASPL contour around the launch vehicle is examined. This phenomenon is important for simulating the acoustic field similar to the actual environment according to the height change. And we carried out the validation with a case where the acoustic field was experimented with the height change. As a result of the prediction, the original prediction method does not consider the impingement source, and the error of the prediction value of OASPL increases with the increase of the height except initial launch. On the other hand, in the case of the second improved empirical

method considering the impingement source, the reliability of the prediction of the acoustic field according to the launch vehicle height is secured by modeling the power and directivity of the impingement source as the height increases.

The development of this second improved empirical method, impinging jet noise model, is important because it can be used in a multi-objective optimization of low noise launch pad studies to be performed in Chapter 3. The study is a latest research on acoustic environment of launch vehicle, and it has been mainly carried out by numerical approach due to the limitation of original empirical method. However, very large cost and computation time are required to perform numerical methods for multi-objective optimization study on launch vehicle acoustic loads. The numerical approach is difficult in reality, because the launch environment has been diversified and the optimization requirements can also be changed variously. In Chapter 3, the second improved empirical method, the impinging jet noise model developed in Chapter 2, will be used to study multi-objective optimization of low noise launch pad. However, in order to realize this, it is necessary to include the additional method for simulating the curved low noise launch pad and the multi-objective optimization algorithm. Therefore, in Chapter 3, we will examine the additional methods for multi-objective optimization problem and apply them to the second improved empirical

method. Then we compare the results of empirical-based optimization to that of numerical-based method to verify the result of this dissertation.

Chapter 3. Multi-Objective Optimization of Low Noise Launch Pad

3.1 Low Noise Launch Pad

Recent interest in acoustic loads of launch vehicles is the design of low noise launch pad. Tsutsumi et al.[19, 20, 89] proposed a shape of low noise launch pad in relation to the emission characteristics of supersonic impinging jet in an actual launch environment. Since the acoustic loading on launch vehicle is affected by acoustic waves near the impingement region, it is essential to design the low noise launch pad in a curved shape to lessen the influence from the impingement source.

On the other hand, the empirical acoustic loads prediction method is a method of arranging noise sources along the jet flame axis. Since the conventional launch pad geometry was simple, most researchers placed the noise sources in a relatively simple way along the jet flame axis, which consisted of several straight lines. In this way, however, there is a limit to simulate the jet flame axis along a curved launch pad shape like a low noise launch pad. Therefore, in this chapter, we will discuss how to distribute noise sources to simulate a curved launch pad in a second improved empirical method that can consider the impingement source. This will allow

us to simulate the recently studied low noise launch pad and validate the prediction results with a new source distributing method.

3.1.1   Non-Uniform Rational B-Spline(NURBS)

Non-uniform rational B-spline, NURBS, is one of the mathematical representations of the geometric body. By using the NURBS, the user can simulate very precisely from 2-D simple line segments, arcs, curves to highly complex 3-D curved surfaces and lumps. And due to its ease of editing, this method is used in various areas. Using this advantage, in this dissertation, the NURBS is applied to the second improved empirical method as a new distributing method that simulates a curved launch pad.

On the other hand, the NURBS curves are determined by several factors, which are degree, control points, knot vectors, and weight. For NURBS curves with m control points and d degree, the final curve is calculated as the sum of the basis functions for the control point as following equation [103].

$$p(t) = \frac{\sum_{i=0}^{m-1} B_{i,d}(t) p_i w_i}{\sum_{i=0}^{m-1} B_{i,d}(t) w_i} \qquad (3.1)$$

Where $B_{i,d}$ is the basis function for the ith control pint and p_i, w_i are

the control point and weight for the ith control point, respectively. The basis

function for the ith control point is defined as following equation [103].

$$B_{i,0}(t) = \begin{cases} 1, & if \quad t_i \leq t < t_{i+1} \\ 0, & otherwise \end{cases} \tag{3.2}$$

$$B_{i,d}(t) = \frac{t - t_i}{t_{i+d} - t_i} B_{i,d-1}(t) + \frac{t_{i+d+1} - t}{t_{i+d+1} - t_{i+1}} B_{i+1,d-1}(t) \tag{3.3}$$

There are several rules for using NURBS: first, the number of control

points must be at least 1 higher than the degree. Second, the number of knot

vectors should equal the sum of the number of control points plus degree

plus one. Third, the degree of the curve should be at least 2. Fourth, the valid

intervals for the NURBS curves are (degree- 1) ~ (the number of control

points). Finally, the value of the knot vector must be written in ascending

order. The following sections describe parameters such as degree, knot

vector, weight that affect the NURBS curves.

3.1.1.1 Degree

The NURBS curves are defined as a series of polynomials. The order of the

polynomial is called the degree of the NURBS curves. Sufficient control

points are required to implement the degree of desired polynomials, and the

number of control points must be greater than one. In this case, the number
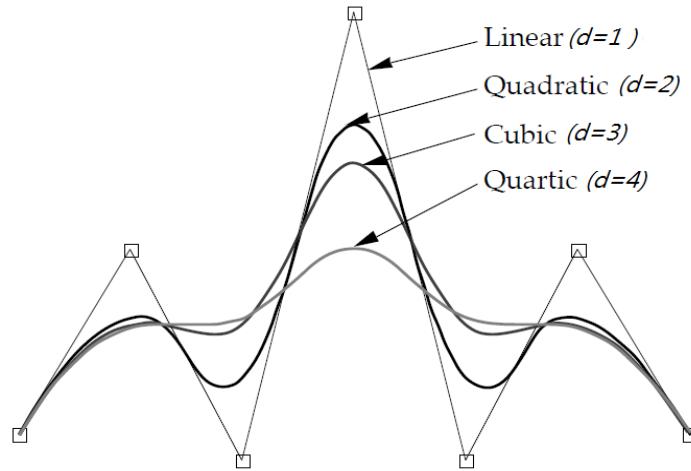
Fig. 3.1. The effect of degree on the NURBS curves[104]

of NURBS curves is set to $m - (d - 1)$ according to the degree of the curve (d) and the number of control points (m). NURBS curves with degrees of second and third order are most commonly used. Figure 3.1 shows the NURBS curves according to degree change for 7 control points. If the degree is high, the curvature of the curve is smaller because it is influenced by more control points than when the degree is lower. On the contrary, if the degree is low, the curve can be more influenced when moving one control point. On the other hand, degree is a variable that has a large influence on the generation time of NURBS curves. In general, it is common to implement NURBS of less than or equal to the third degree because it takes a long calculation time for curves having a degree of 4 or more.

106

3.1.1.2 Knot Vector

The knot vector is an additional feature of the NURBS curve that distinguishes it from the other curves and determines where the polynomial starts. The representative form of the knot vector is 'pinned uniform'. In this case, the NURBS curve starts at the first control point and ends at the last control point (both ends are 'pinned' to the control point), and the curves between the two end control points do not pass through the control point. The number of knot vectors should equal the sum of the number of control points plus degree plus one. In order to implement pinned uniform NURBS curves, the first $d+1$ knot vector values must be equal to each other, the last $d+1$ knot vector values must be equal to each other, and the increment of the knot vector must be constant. If the degree of the NURBS curves is 3 ($d=3$), the number of control points is 6 ($m=6$) and the knot
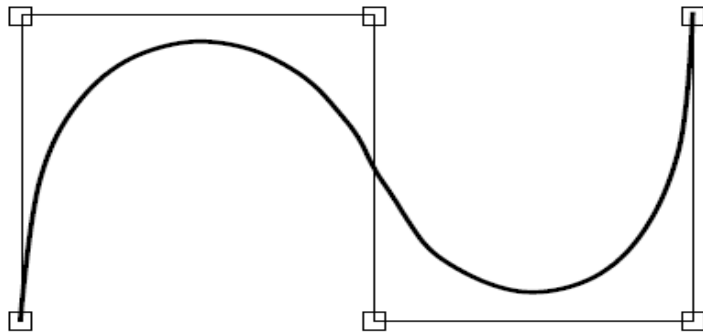
Fig. 3.2. A pinned uniform type NURBS curve ($d=3, m=6$)[104]

107

vector value of $[0,0,0,0,1,2,3,3,3,3]$, then the pinned uniform NURBS curves are shown in figure 3.2.

3.1.1.3 Weight

Weight can be regarded as the degree of influence of one control point on the NURBS curves. Unlike the existing Bezier spline, the degree of influence of each control point on the NURBS curve can be controlled by weight in the NURBS curves. Therefore, the expression of NURBS curves can be expressed by using the basis function with weight. The range of influence of the ith weight value on the ith control point is $[[t_i, t_{i+d})]$. The larger the value of weight, the closer the NURBS curve is toward the control point. The smaller the value of weight, the farther away from the control point.
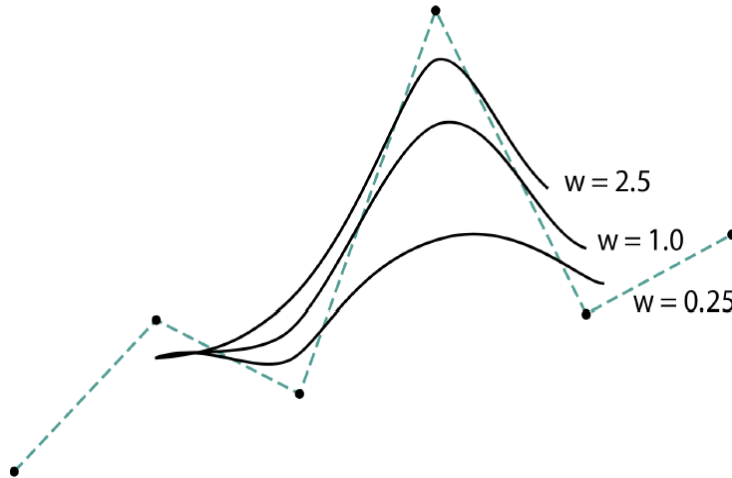
Fig. 3.3. Effect of weight on NURBS curves[104]

3.1.2   Validation and Results

In this dissertation, the pinned uniform NURBS curves which is the most representative type of knot vector were applied to the second improved empirical method. Figure 3.4 shows the difference between distributing sources along a curve using NURBS and along a straight line. Although the drastic changes are not expected, the geometric relation between the source and the receiver will affect the power and spectrum according to the noise source placement method, and the directivity index will change according to the flame axis change. In the next section, we will examine the prediction results for the Epsilon rocket of the Tsutsumi et al. [20] study as a validation case of the second improved empirical method with NURBS curves applied.
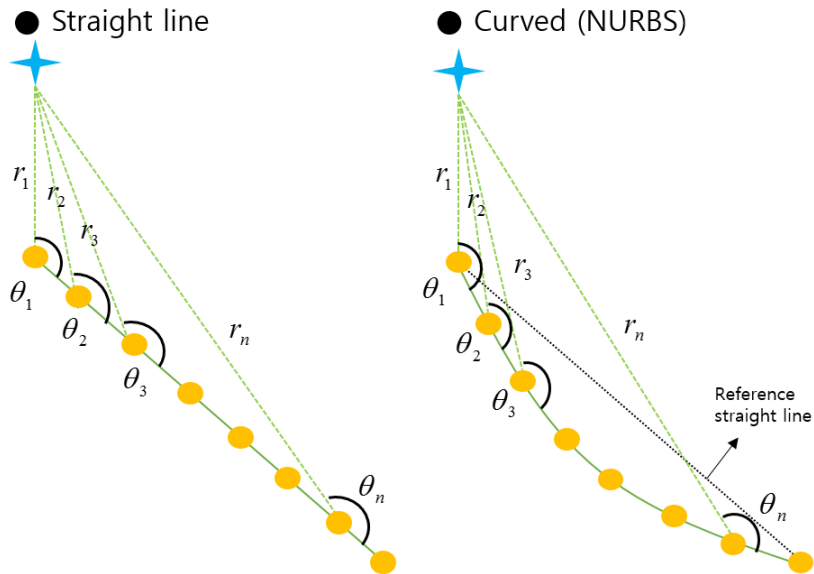
Fig. 3.4. Comparison of source distributing method

3.1.2.1 Case1: Epsilon Rocket

Tsutsumi et al.[20] predicted acoustic environment for a curved low noise launch pad with an initial inclination angle of 14 degrees, as shown in figure 3.5. And the specification of Epsilon rocket used in the analysis is shown in table 3.1.

Table 3.1. Specification of Epsilon rocket [20]

Parameter	Value
Nozzle exit Mach number	3.7
Pressure ratio of stagnation to ambient condition	89.1
Temperature ratio of stagnation to ambient condition	12
Heat specific ratio of nozzle condition	1.2
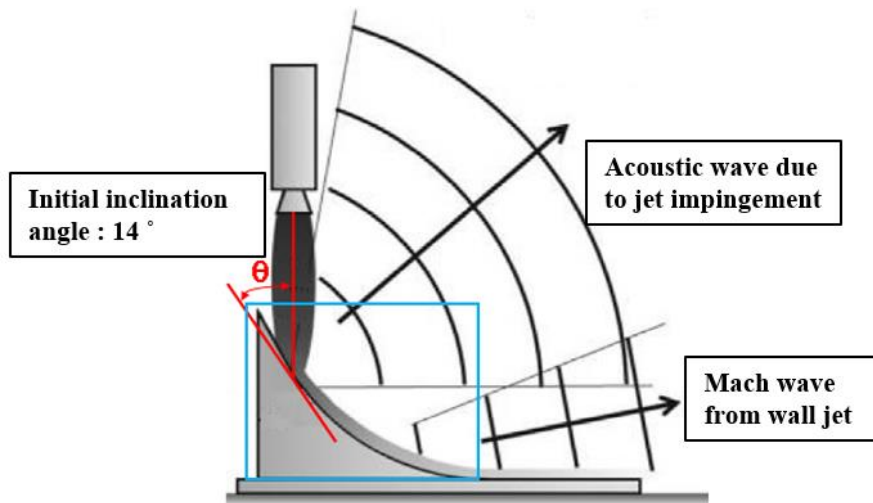
Fig. 3.5. Schematic sketch of acoustic waves around the low noise launch pad[20]

Table 3.2. NURBS parameters to simulate curved low noise launch pad
of Epsilon rocket

Parameter	Value
Degree	3
Number of control points	8
Coordinates of control points	(0, H), (0, 0.05), (0.003, 0.032) (0.0127, 0.015), (0.03, 0.001), (0.05,0), (2,0)
Knot vector	[0, 0, 0, 0, 0, 0.2, 0.4, 0.6, 0.8, 1, 1, 1, 1,]
Weight	[1, 1, 1, 1, 1, 1, 1, 1]
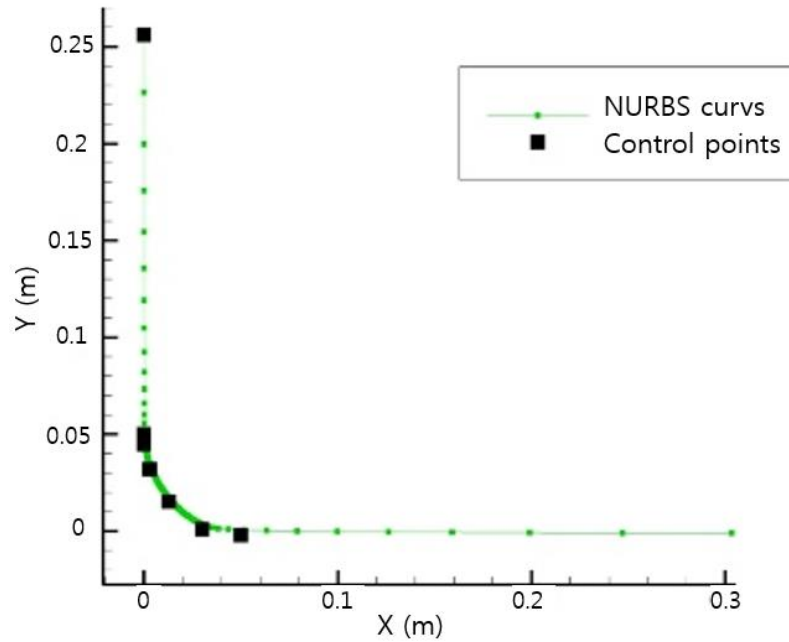
Fig. 3.6. NURBS curves simulating curved low noise launch pad of
Epsilon rocket

In order to simulate the jet flame axis along a curved low noise launch pad like the blue box area of figure 3.5, the NURBS parameters as shown in table 3.2 were used. The study of Epsilon rocket is done according to height variation of $9D_e$ and $14D_e$, so coordinate of the first control point depends on the corresponding height (0, H).

Comparison of the predicted acoustic environment around the launch pad of the numerical analysis with the empirical methods of DSM and ASDSM is shown in figure 3.6. As confirmed in the previous cases in the sections 2.3.4.2 and 2.3.4.3, the results show that DSM has only the turbulent mixing noise component generated from the main jet downstream from the nozzle exit by $1.8L_t$. On the other hand, the ASDSM has the additional acoustic propagation directions near the impingement region which is similar as the numerical acoustic field.

The effects of this additional impingement source of ASDSM can also be confirmed by comparing the experimental results at the M7 position in the placement of microphones as shown in figure 3.7. The measurement point of M7 is located on the launch vehicle surface, which is $11D_e$ above the nozzle exit. For each height, the information for impingement source power are presented in table 3.3.
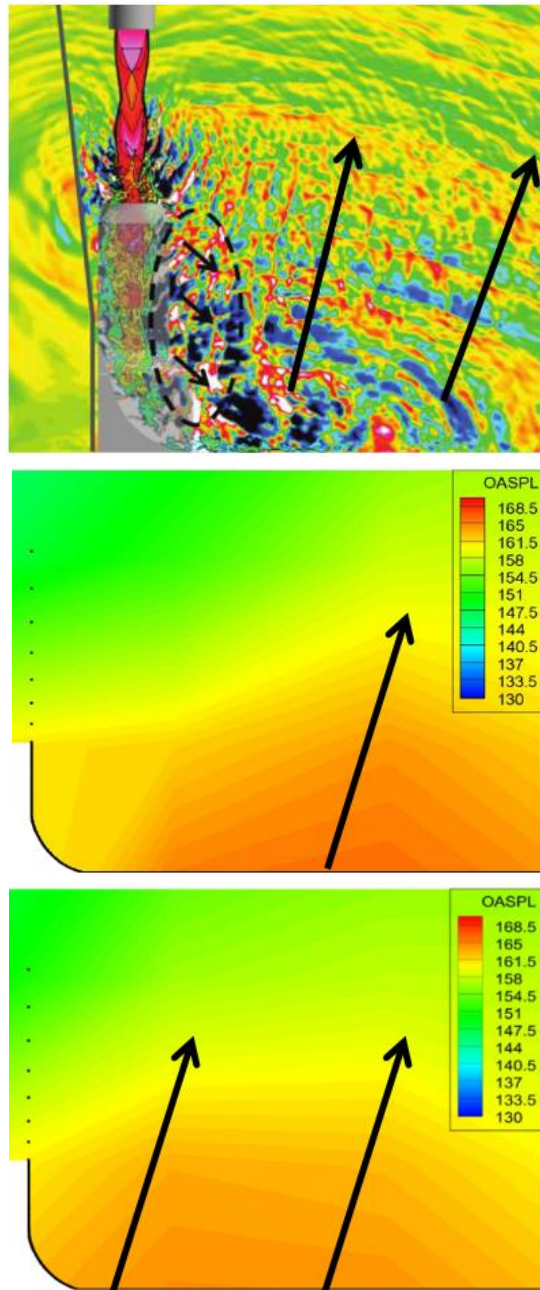
Fig. 3.7. Comparison of acoustic fields for Epsilon rocket at H=14D$_e$.

(Top: numerical[20], Middle: DSM-II, Bottom: ASDSM)

Table 3.3. Information for impingement source power at H=9D$_e$, 14D$_e$

Parameter	H=9D$_e$	H=14D$_e$
Normalized impingement height (H/L_T)	0.29	0.56
Relative sound power level ($L_{DSM} - L_{imp,s}$)	8.2 dB	5.8 dB
Sound power level of DSM sources (L_{DSM})	155.7 dB	155.3 dB
Sound power level of impingement source ($L_{imp,s}$)	147.5 dB	149.5 dB
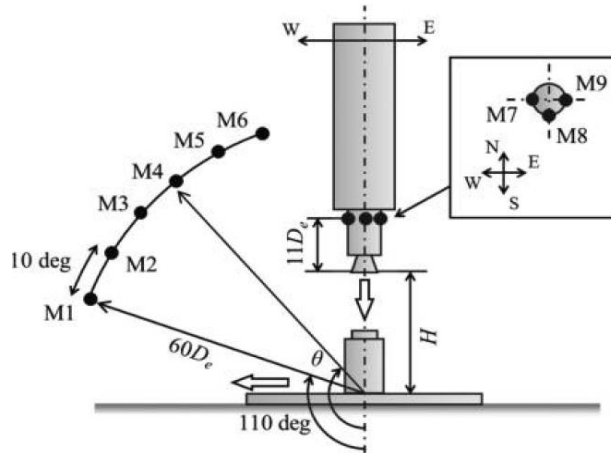
Fig. 3.8. Placement of microphones of Epsilon rocket[20]

Figures 3.9-3.10 show the results of comparison of the OASPL value and the spectrum with the experiment and each prediction for each height. Again, as shown in the previous cases, we can confirm the improvement in prediction results in terms of OASPL and spectrum. This means not only that the accuracy of the ASDSM for each height is reliable for the Epsilon rocket, but also that NURBS, a new distributing source method, is well applied to ASDSM to simulate a curved low noise launch pad.
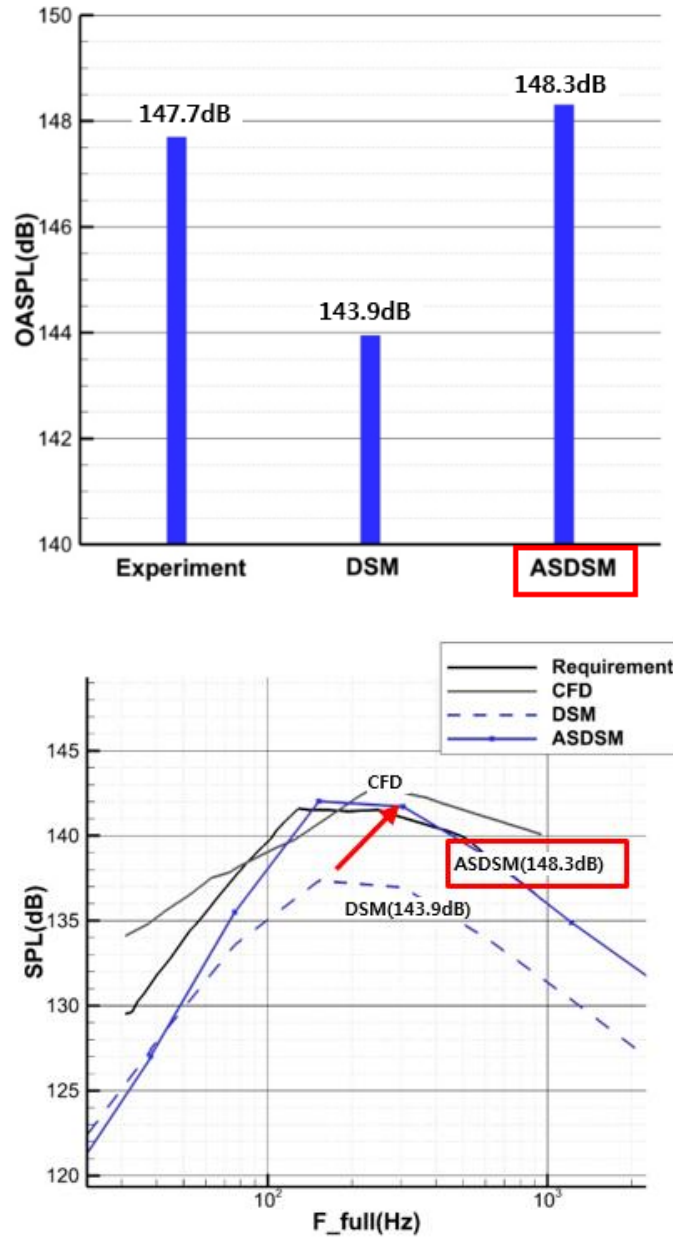
Fig. 3.9. Comparison of the OASPL and the 1/1 octave band spectrum
with the experiment and each prediction for Epsilon rocket at H=9D_e
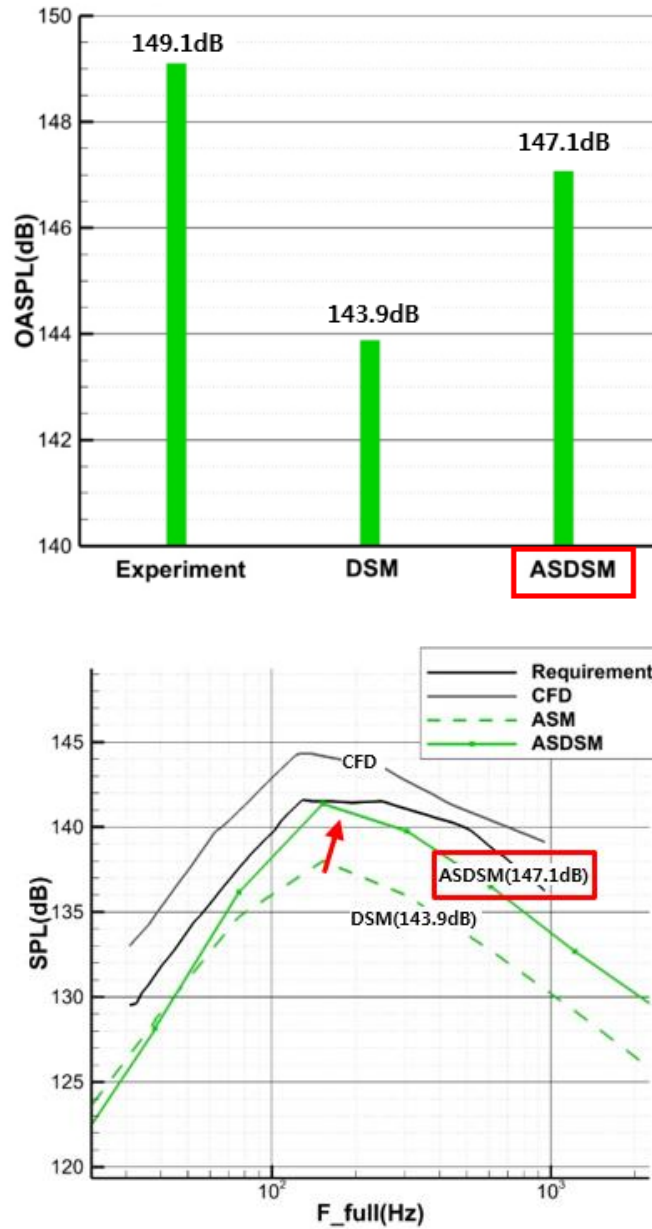
Fig. 3.10. Comparison of the OASPL and the 1/1 octave band spectrum
with the experiment and each prediction for Epsilon rocket at H=14D$_e$

116

3.2 Multi-Objective Optimization

3.2.1 Definition

In addition to the design of low noise launch pad, recent research on the acoustic loads have been carried out about multi-objective optimization of launch pad shape which considers additional design conditions.

In principle, multi-objective optimization is very different from single-objective optimization. In single-objective optimization, one tries to obtain the best solution depending on whether the problem is minimization or maximization problem for an objective function [105]. On the other hand, in the case of multi-objective optimization, there may not exist one best solution because it is involved in more than one objective function. Typically, the optimal decisions need to be taken in the presence of trade-offs between two or more conflicting objectives.

In that case, there exists a possibly infinite number of Pareto optimal solutions. A solution is called 'Pareto optimal solution' or 'non-dominated', if none of the objective functions can be improved without degrading some of the other objective values[106]. All Pareto optimal solutions are considered equally good and acceptable solutions and the boundary formed by the set of Pareto optimal solutions is called the Pareto line.

There are two most representative philosophies and goals when setting and solving the multi-objective optimization problems. The first is a 'priori'

method which includes the utility function scalarized by all the objectives with a weight factor, making the original multi-objective problem into a single-objective optimization problem. The purpose is to find a single solution that satisfies the preferences of a human decision maker(DM) about the multi-objective optimization problem before the solution process [107]. In this methods, preference information is first asked from the DM and then a solution best satisfying these preferences is found. However, in practice, it is very difficult to construct a utility function that would accurately represent the DM's preferences and the obtained solution largely depends on the weight factor used in the scalarization process[108].

On the other hand, 'posteriori' method is aiming at producing all or a representative set of Pareto optimal solutions. It has the advantage of being able to get a set of Pareto optimal solutions simultaneously in one run of the algorithm. So, it is available for DM to choose one solution among the alternate solutions on the Pareto line. The representative class of a posteriori method is the evolutionary algorithms and the non-dominated sorting genetic algorithm II (NSGA-II) is known as the most powerful and effective method in the multi-objective optimization problem. In the next section, we will examine the feature of NSGA-II, which will be used for multi-objective optimization of low noise launch pads.

3.2.2   Non-dominated Sorting Genetic Algorithm II (NSGA-II)

NSGA-II is the method being able to get a set of Pareto optimal solutions simultaneously in one run of the algorithm. The idea behind the NSGA-II is to use the concept of non-dominated sorting and crowding distance as a process of ranking individuals for the next generation selection. NSGA-II differs from a simple genetic algorithm in the way the selection operator works. Before the selection is performed, the population is pre-processed in the following procedure[48] and crossover and mutation operators remain

Initially, a random parent population P_0 is created. Next, the usual binary tournament selection, recombination, and mutation operators are used to create offspring population Q_0 of size N. Then, non-domination ranking is given to individuals. The non-domination rank is assigned a higher rank
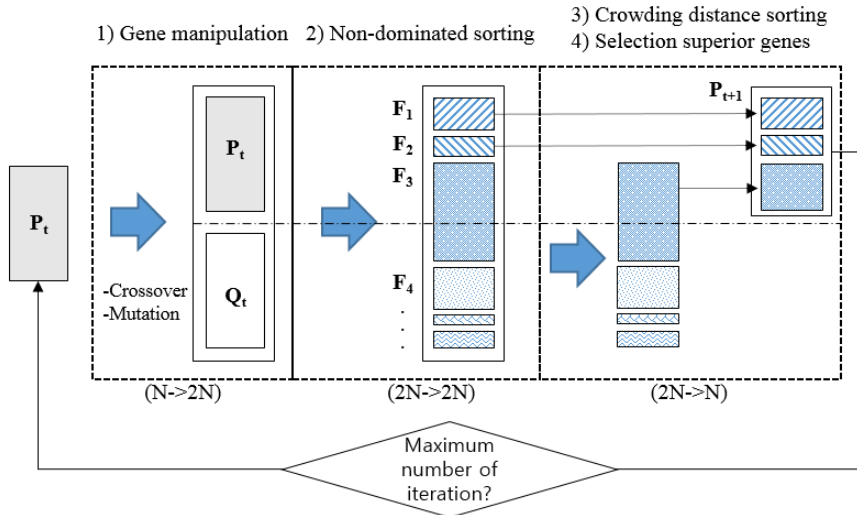
Fig. 3.11. Procedure of NSGA-II

119

as the corresponding solution is closer to the Pareto line[109]. For example, if there is no solution that dominates a solution B, then the non-domination rank of B is 1. If there is one solution that dominates the solution B, the non-domination rank of B is 2. And then the crowding distance is sorted in descending order for the same non-domination rank. Crowding distance is a measure of diversity in a set of solutions with the same non-domination rank. Each individual has higher crowding distance as the density of the surroundings is lower, that is, the similarity within the gene is smaller. The reason why NSGA-II uses crowding distance for sorting procedure is to select individuals with the most different properties among the set of solutions belonging to the same non-domination rank.

Now, solutions belonging to the best non-dominated set F_1 are of best solutions in the whole population and must be emphasized more than any other solutions. If the size of F_1 is smaller than N, we definitely choose all members of the set F_1 for the new population P_{t+1}. The remaining members of the population P_{t+1} are chosen from subsequent non-domination ranks of their own. Thus, solutions from the set F_2 are chosen next, followed by solutions from the set F_3, and so on. This procedure is continued until no more sets can be accommodated. This evolution process is performed until a pre-determined condition or maximum number of iterations is reached[48].

3.2.3 Multi-Objectives of Low Noise Launch Pad

As shown in figure 3.12, we studied multi-objective optimization of low noise launch pad by using second improved empirical method (ASDSM), a new source distributing model (NURBS) and multi-objective optimization algorithm (NSGA-II). In this thesis, we only cover the range of research related to the validity of using empirical method compared with reference research. Based on the reference paper, we tried to obtain a low noise launch pad shape that was optimized for the following three objectives. All objective functions are estimated in a similar way to the reference paper.

    i)   Minimization of the sound pressure level (SPL) on the fairing

    ii)   Minimization of impact force on the launch pad

    iii)   Minimization of shape difference from the reference shape
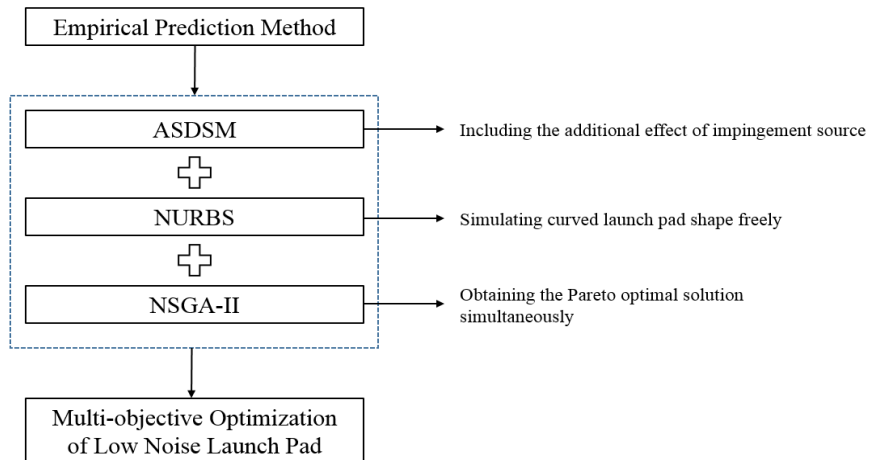
Fig. 3.12. Empirical and additional method for the optimization problem
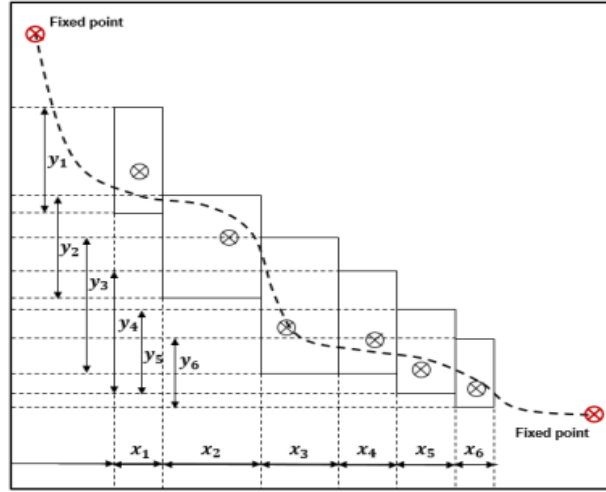
Fig. 3.13. Design variables of optimization problem

The design variables of this multi-objective optimization problem are the coordinates of the control points of the NURBS as shown in figure 3.13. The knot vector type of NURBS curves is a general pinned form with 8 total control points. The first and last control points are fixed points at (-2.857, 20), (25,714, -8.571) respectively. The available range of each control point is given in the following table 3.4. Design variables affect the NURBS curve, affecting all three objectives, so a multi-objective optimization process can be performed according to the change in design variables.

Table 3.4. Range of design variables of optimization problem

	2nd	3rd	4th	5th	6th	7th
X	[-1 3]	[3 8]	[8 12]	[12 16]	[16 19]	[19 24]
Y	[9 16]	[5 13]	[1 11]	[0 7]	[-4 7]	[-7 -3]

122

On the other hand, the optimized launch pad shape has a constraint condition that the slope of shape must be less than zero. This constraint reduces the complexity of the launch pad shape and results in a realistic launch pad shape. In the next section, we will discuss each objective.

3.2.3.1   Sound Pressure Level

The first objective value is the sound pressure level (SPL) at the fairing of launch vehicle. Because the SPL affects the satellites for withstanding vibration, it is important to get a launch pad shape that has smaller effect of SPL. The nozzle-to-deflector distance changes according to the design variable and determines the power of the impingement source, and the impingement angle determines the directivity resulting in the SPL on the vehicle. It is expected that the SPL on the fairing will become smaller as the nozzle-to-deflector distance is farther away from 1.8 L_t and the impingement angle is steeper.

3.2.3.2   Impact Force

The second objective value is impact force on launch pad. It affects the maintenance cost and is calculated as following equation (3.4).

$$F_{impact} \approx \dot{m}U_{imp} \tag{3.4}$$

$\dot{m}$ is the mass flow rate (kg/s) and U_{imp} is the impingement velocity, as remarked in equations (2.1) and (2.28), respectively.

3.2.3.3 Shape difference

The third objective value is the shape difference. From the viewpoint of the construction cost, the difference of the designed shape of the launch pad from the reference shape should be minimized. The reference shape of original launch pad is a straight line with a 45 degree inclined. And we define the shape difference from this reference shape as the construction cost. Figure 3.14 shows three objectives of multi-objective optimization of low noise launch pad.
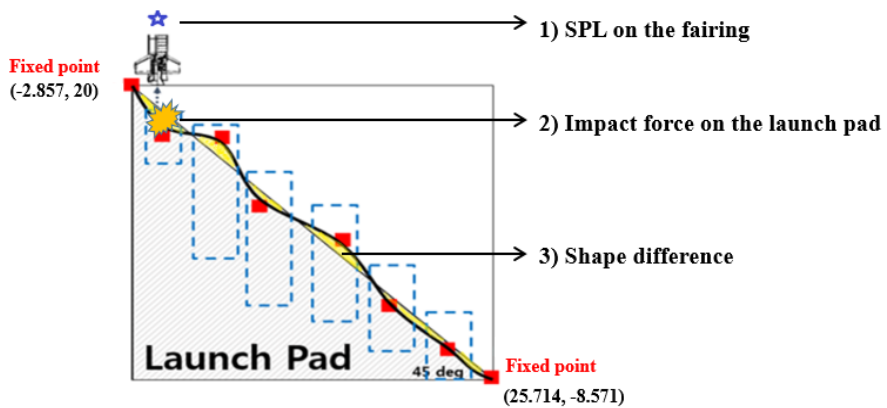
Fig. 3.14. Multiple objectives related to shape of low noise launch pad

3.2.4   Optimization Results

The one thing to note in the optimization results section is that there is no clear data to compare with the optimization result of this study. However, compared with the existing numerical multi-objective optimization results, we will examine how feasible the empirical method based research is.   The three objectives of the low noise launch pad optimization described above are the same as those considered in the numerical reference paper. In that paper, they employed shock capturing high-order scheme and it takes too much grid system, data storage for acoustic analysis and computation time. In fact, in their study, the size of population is 50 and the number of generations is 50, so a total of 2,500 cases were analyzed.   Considering that they said it took about 7 hours to conduct 1 shape configuration by using 1,040 CPU cores of "K" supercomputer, it can be seen that a total of 2,500 cases requires 730 days.

   However, our approach is based on empirical method with additional complementary methods such as impingement source model (ASDSM), a new source distributing model (NURBS) and multi-objective optimization algorithm (NSGA-II). In this results section, we will examine how the empirical based multi-objective optimization is performed according to the design variable and how the results are compared with the reference paper in the aspects of both accuracy and efficiency. The rocket specification was

125

taken with that of the KSR-III and the size of the population and the number of generations are 1000 and 100, respectively in the NSGA-II algorithm. It took two days for the whole optimization process for a personal PC.

3.2.4.1 Convergence

First, we will examine the convergence results of the optimization problem. Figure 3.15 is the 3D scatter plot with the axis of each objective value. The left one in the figure 3.15 shows the distribution of the initial population and the right figure shows the final convergence result with the last generation. The initial population was randomly distributed in the range of design variables and then reached the last generation through the evolution process based on NSGA-II. It can be seen that the red dots of the last generation form Pareto-optimal solutions.
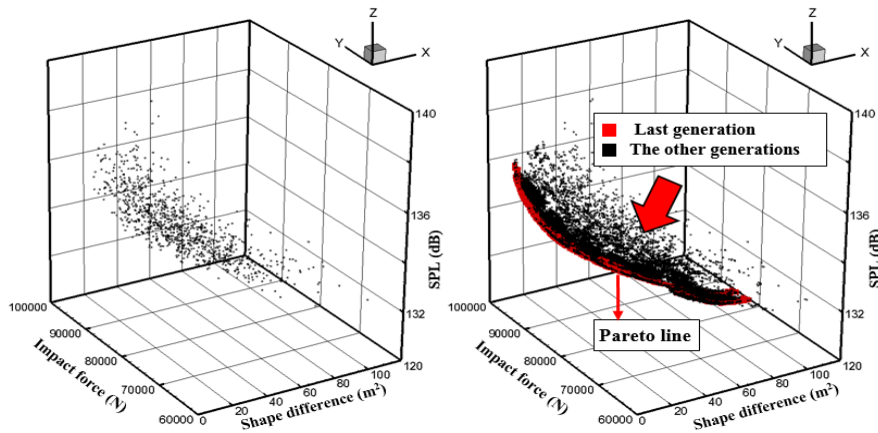
Fig. 3.15. 3D scatter plot of multi-objective optimization problem
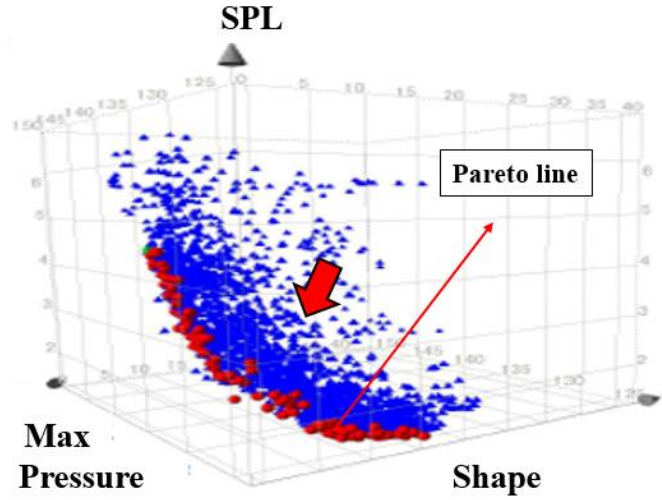
Fig. 3.16. 3D scatter plot of multi-objective optimization problem
(numerical result)[21]

Since each objective function of this multi-objective optimization problem has to be minimized, it must be found that the final solution converges in the direction to the origin. This can be seen in the 3D scatter plot in figure 3.15, which is the result of empirical based method, and also in the numerical result in figure 3.16. And it is more clearly seen in the 2D scatter plot in figure 3.17. This shows that the initially scattered solutions gradually evolve towards the lower left, the optimal direction through the evolution process, and finally the last solutions form the Pareto optimal line. Also in these the 2D scatter plots, we can see the relationships between each objective and it can be examined through the correlation coefficient in the next section.

127
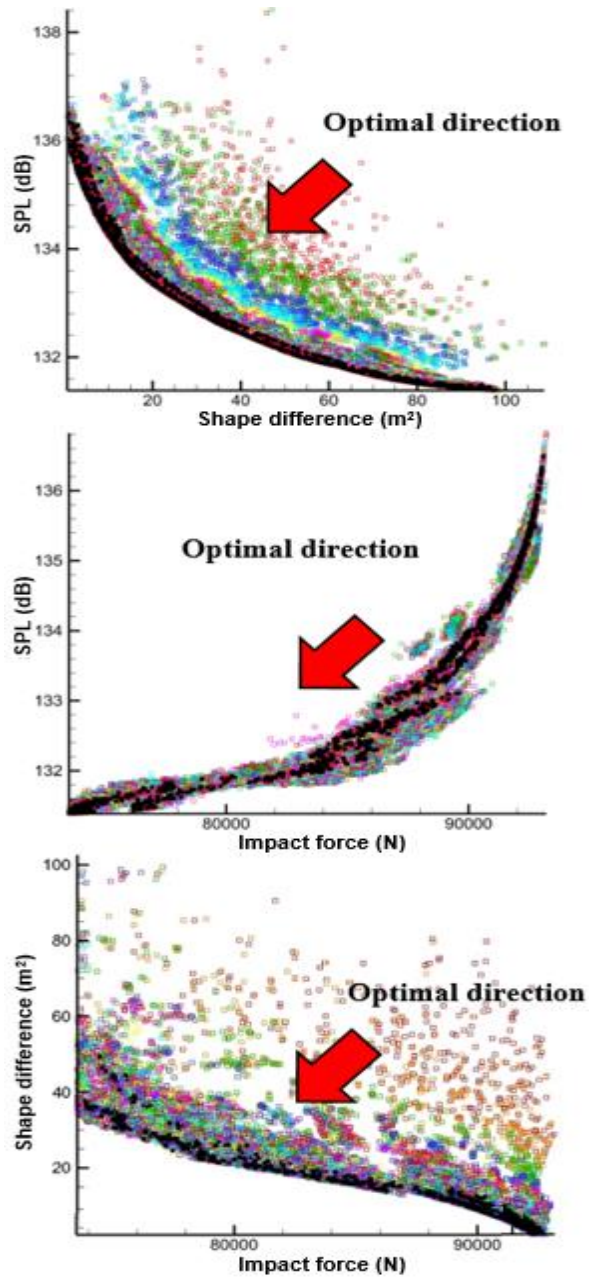
Fig. 3.17 . 2D scatter plot of multi-objective optimization problem
(Top: SPL-shape, Middle: SPL-force, Bottom: shape-force)

3.2.4.2 Correlation Coefficients

The correlation coefficient is a measure of the linear dependence between two variables[21]. A positive value means that as one variable increases, the other increases too. And the negative value means that as one variable increases and the other decreases. The values range between -1.0 and 1.0.

Most representative method is the Pearson correlation which is represented by the Greek letter ρ. Given a pair of random variables (X,Y), the formula is defined as following equation (3.5) [110].

$$\rho_{X,Y} = \frac{\text{cov}(X,Y)}{\sigma_X \sigma_Y} \tag{3.5}$$

Where $\text{cov}(X,Y)$ is the covariance, σ_X, σ_Y are the standard deviation of X, Y respectively. The formula can be also expressed in terms of mean and expectation as following equation (3.6).

$$\rho_{X,Y} = \frac{E[(X - \mu_X)(Y - \mu_Y)]}{\sigma_X \sigma_Y} \tag{3.6}$$

Where μ_X, μ_Y is the mean of X, Y respectively and E is the expectation. And by using the equations of uncentered moments, the formula for ρ can be written as following equation (3.7).

$$\rho_{X,Y} = \frac{E[XY] - E[X]E[Y]}{\sqrt{E[X^2] - [E[X]]^2} \sqrt{E[Y^2] - [E[Y]]^2}} \tag{3.7}$$

Table 3.5. Pearson correlation coefficient of each objectives

Correlation coefficient	
Sound pressure level - Impact force	0.895
Sound pressure level – Shape difference	-0.918
Impact force – Shape difference	-0.983

The correlation coefficient is calculated by using the optimized solutions of last generation. And correlation coefficients between each objective variable are shown in the table 3.5. The calculated results show that there is strong correlative relationship between SPL and impact force. This means that SPL and impact force can be improved at the same time. On the other hand, there is a strong inverse relation between SPL and the construction. It means that it is essential to significantly change the shape of launch pad to improve SPL and impact force.

3.2.4.3 Optimization Solutions

As mentioned above in the definition section of multi-objective optimization (3.2.1), there may not exist one best solution because it is involved in more than one objective function. Typically, the optimal decisions need to be taken in the presence of trade-offs between two or more conflicting objectives. All the non-dominated solutions on the Pareto line are can be a possible solution and the choice depends on the decision maker.
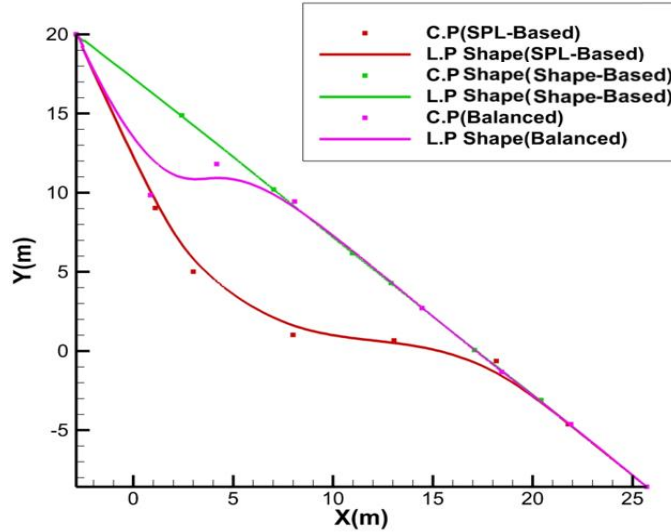
Fig. 3.18. Control points and launch pad shape of optimized solutions

We chose and discussed three solutions from all of the available solutions on the last generation, just like the numerical reference paper to compare results. Three solutions were selected from the top figure in figure 3.17, 2D optimized results of the two objectives(SPL-shape). The first one is the solution with the smallest SPL value as the SPL-based solution, the second is the shape-based solution with the smallest value of shape difference, and the third is called the balanced solution which has moderate SPL and shape difference values due to the trade-off. Figure 3.18 shows control points and launch pad shape of three optimized solutions. The launch pad shape of the SPL-based solution which has the lowest SPL value shows the steepest slope in the impingement region. This result in the propagation direction of the impingement source to move away from the launch vehicle and the

influence of the Mach wave in the downstream is also reduced. And the shape of the shape-based solution is almost identical to the reference launch pad shape which has a straight line with a 45 degree inclined. This result is clear considering the shape difference from the reference launch pad shape. On the other hand, since the launch pad shape of balanced solution has more relaxed initial slope and area difference, it may have moderate SPL and shape difference value. The objective values for each solution are summarized in Table 3.6.

Table 3.6. Summarization of objective value for optimized solutions

	SPL-based	Shape-based	Balanced
SPL (dB)	131.33	136.00	134.05
Shape difference (m^2)	109.11	1.17	25.18
Impact Force (N)	73,583	92857	81,090

3.2.4.4 Comparison with Numerical Solutions

The three solutions obtained in the previous section are compared with the numerical results. Although a specific rocket specification is not provided in the numerical reference paper, it is possible to make a meaningful comparison with the numerical result. In aspect of convergence, we have confirmed that the objective values clearly converge in the direction toward minimization in the previous section 3.2.4.1. These results can be found well in figure 3.16 and the following 2D scattering plot in numerical results.
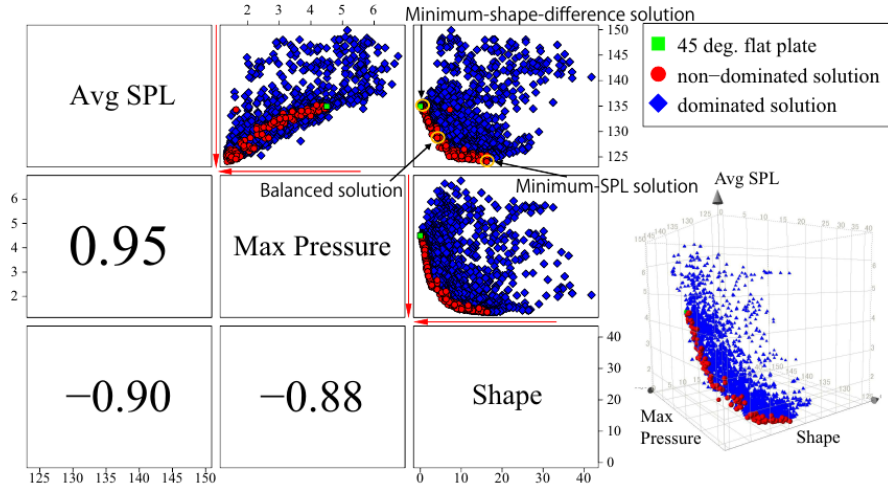
Fig. 3.19. Scatter plots and correlation coefficients of numerical reference paper[21]

Figure 3.19 also shows the correlation coefficient between each objective function. This is a result of about 2% to 10% difference compared with the correlation coefficient obtained by the empirical-based method in section 3.2.4.2. This means that, compared with the numerical method, the empirical-based study about multi-objective optimization of low noise launch pad considering same objectives is reliable in terms of the correlation coefficient as well as the tendency of convergence.

And compared with numerical results, we can compare the launch pad shape and acoustic field for the three solutions in the final optimal solutions. Among the optimal solutions on the Pareto line obtained by the NSGA-II algorithm, the SPL-based solution, the shape-based solution and the

133

balanced solution are selected as shown in figure 3.19. For each solution, the comparison of the launch pad shape and the acoustic field between the empirical and the numerical method is shown in figure 3.20.
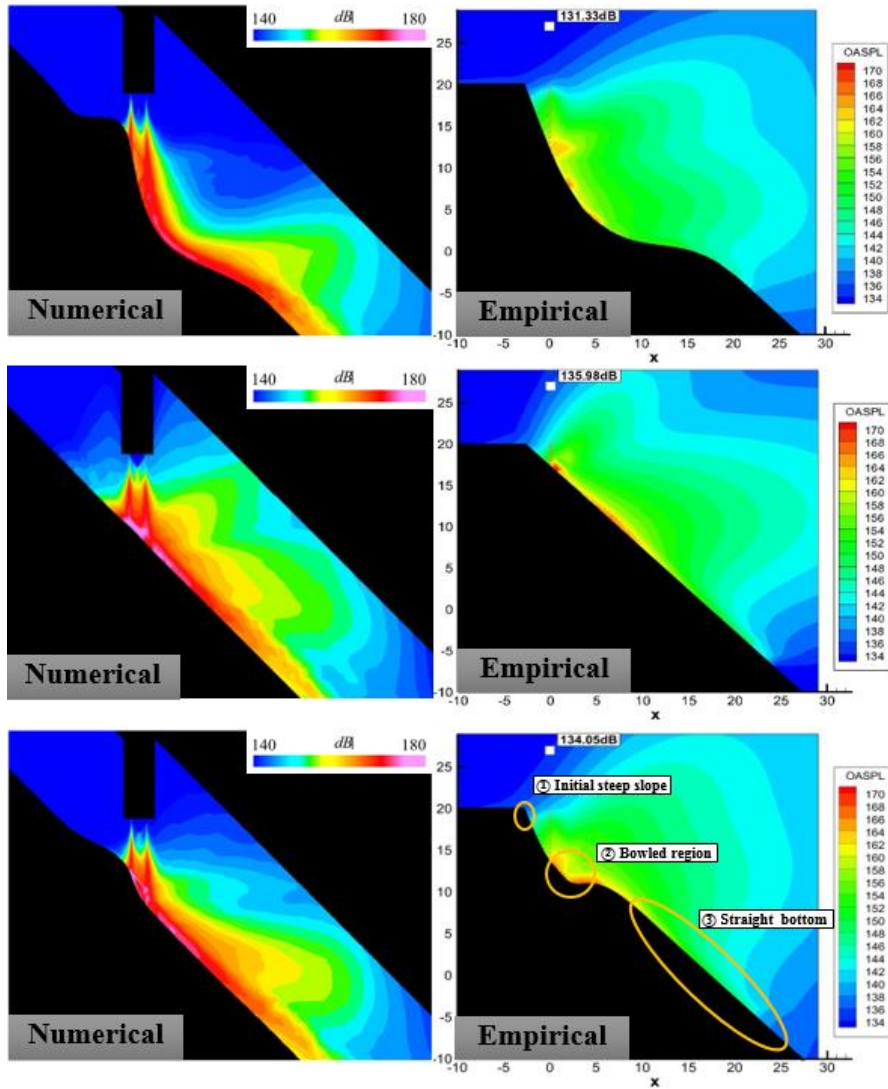
Fig. 3.20. Comparison of launch pad shape and acoustic field[21]
(Top: SPL-based, Middle: shape-based, Bottom: balanced)

First, both the empirical and numerical results for the SPL-based solution are similar and each launch pad shape has an initial steep slope and a large bowl-shape. These shape can result in the propagation direction of the impingement source to move away from the launch vehicle and the influence of the Mach wave in the downstream is also reduced. Next, for the shape-based solution, both the empirical and numerical results have almost identical shape compared to the reference launch pad shape which has a straight line with a 45 degree inclined. And the acoustic fields clearly show two dominant propagation of impingement source and Mach wave and it means that the influence of the impingement source to the launch vehicle become larger. Finally, for the balanced solution, we can see that two results are slightly different. In fact, although all three cases are solutions obtained through multi-objective optimization by NSGA-II, the selection criteria for the balanced solution is little ambiguous compared with the SPL-based solution and the shape-based solution. However, it is meaningful that there are features that can be found in both results. First, the balanced solutions have a steeper initial slope than the reference launch pad shape. This has the effect of reducing the influence of the impingement source on the launch vehicle, as mentioned above. Secondly, they have a bowled region, which reduces the influence of the Mach wave generated by the supersonic flow

along this launch pad. Third, they have a straight line with a 45 degree inclined at a higher position to reduce the shape difference.

Finally, the empirical-based study can be compared with numerical methods in aspect of computation time. Whole procedures performed by the empirical-based study took two days as a personal PC, while the calculation time of the numerical reference paper took 7 hours with 1,040 CPU cores of "K" supercomputer for only one case.

3.2.4.5   Comparison with Original DSM Solutions

In the chapter 2, we developed the second improved empirical method, ASDSM, because applying the original DSM to the multi-objective optimization problem would result in impractical results. So in this section, we compare the optimized solutions of ASDSM with the solutions of original empirical method, DSM.

First, in aspect of convergence, figure 3.21 shows that the objective functions couldn't converge well toward minimization in case of using the original DSM to the optimization problem. Even when using the original DSM, the boundary line is formed from the optimization process but it is very much different from the Pareto line obtained using the ASDSM. These convergence problems can also be confirmed in the following figure 3.22 which represents two-dimensional scatter plot of objective functions.

136
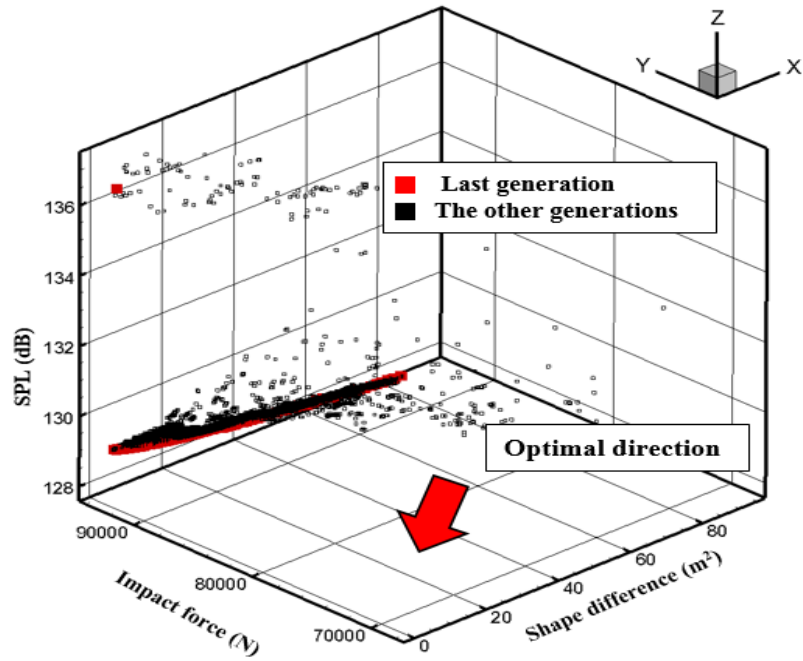
Fig. 3.21. 3D scatter plot of multi-objective optimization problem with original empirical method, DSM
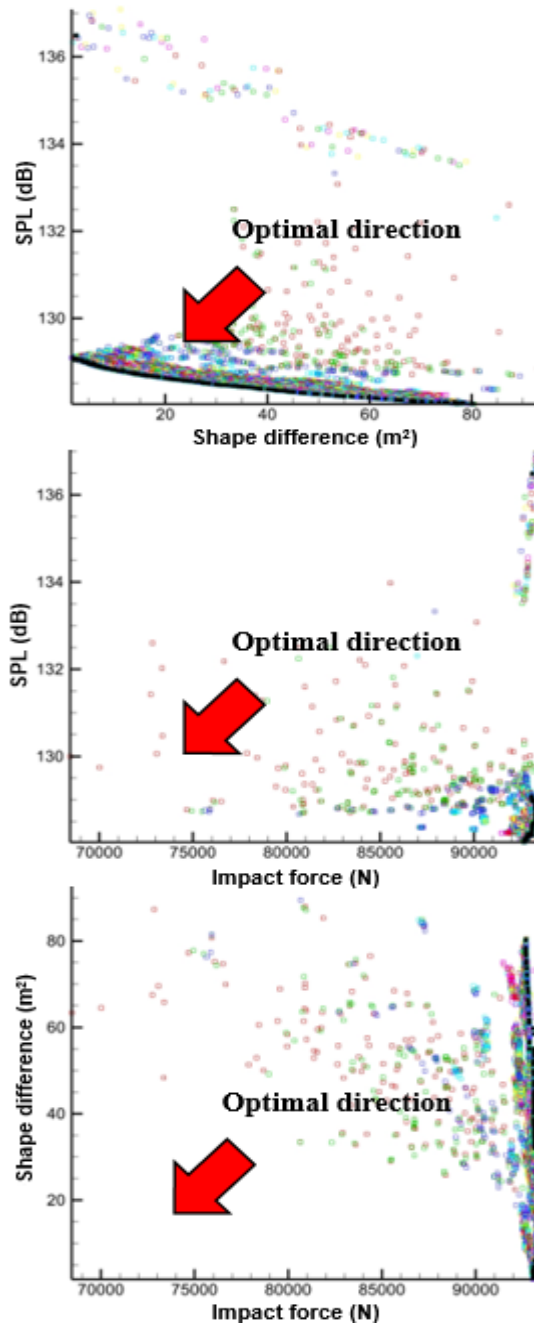
Fig. 3.22. 2D scatter plot of multi-objective optimization with DSM

(Top: SPL-shape, Middle: SPL-force, Bottom: shape-force)

Table 3.7. Comparison of correlation coefficient

	SPL–Shape	SPL–Force	Shape–Force
Numerical	-0.90	0.95	-0.88
ASDSM	-0.92	0.90	-0.98
DSM	-0.53	0.32	-0.81

Table 3.7 shows comparison of the correlation coefficient. In the case of DSM, the correlation between each objective function is weaker and much irregular than the results of the ASDSM and the numerical reference paper. Thus, we can find that the optimized results using original DSM are impractical and it can also be confirmed by optimized launch pad shape in the figure 3.23.
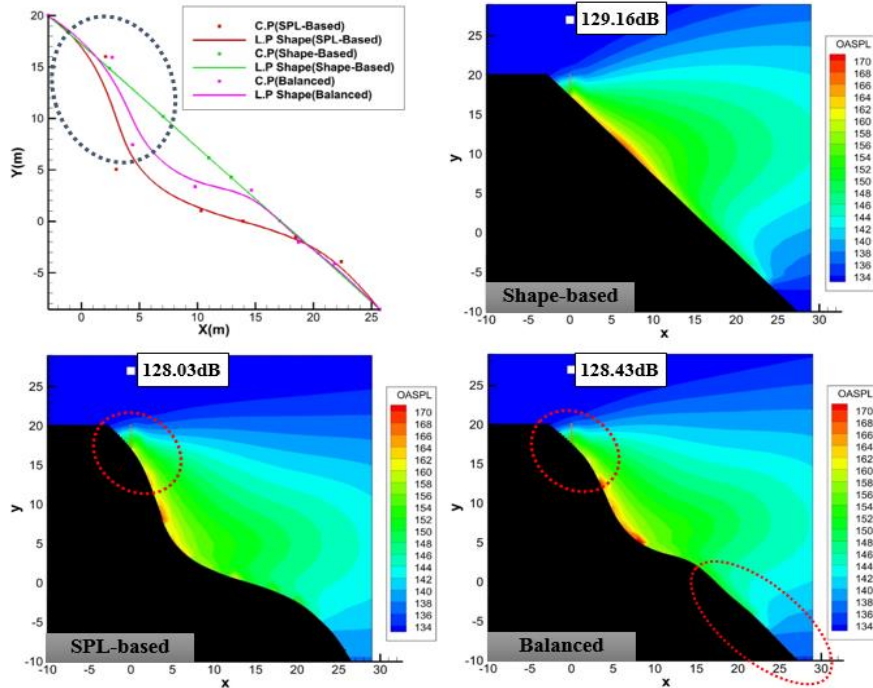
Fig. 3.23. Optimized launch pad shape and acoustic field with DSM

One of major features of DSM-based optimized solutions is that the launch pad shape has the convex shape near the impingement region. It is believed that this is to reduce the effect of the Mach wave radiated from the wall jet, since DSM cannot consider the impingement noise source. In practical case, however, the shape of the impingement region is concave because the effect of the impingement source is dominant on the launch vehicle. It can also be seen that the results of acoustic field are impractical. Since the impingement source is not considered, it shows a contour with the maximum acoustic loading along the wall jet. And when comparing each case, the variation of acoustic loading on the launch vehicle is too small due to the absence of impingement source. From all these points, it can be seen that the multi-objective optimization result using DSM, which is the original empirical method, results in impractical results, and it is necessary to use ASDSM considering the additional impingement source.

3.3   Summary and Discussion

In this chapter, the second improved empirical method, ASDSM, was used to perform a study of multi-objective optimization of low noise launch pad. To do this, this study applied the new source distributing method, NURBS, which can easily simulate a curved launch pad shape. In order to verify that NURBS is applied well, we did a validation about Epsilon rocket associated

140

with the study of designing low noise launch pad shape. The results showed that NURBS can simulate a curved low noise launch pad well. And through the prediction results of acoustic loading, it was confirmed that the ASDSM developed in this dissertation complements the original empirical method well according to the height and it could simulate the actual acoustic field well.

And then, NSGA-II, a multi-objective optimization algorithm, was applied to ASDSM. NSGA-II is known as the most powerful and effective method in the multi-objective optimization problem because it is able to get a set of Pareto optimal solutions simultaneously in one run of the algorithm. By using NSGA-II with ASDSM and NURBS, the study of the multi-objective optimization of low noise launch pad was carried out considering three objectives, SPL, shape difference and impact force on the launch pad. And the three optimized solutions on the Pareto line obtained by the empirical method were compared with those of the numerical reference paper in terms of convergence, correlation coefficient, shape, acoustic field and computation time. The results of empirical-based study show that the convergence, correlation coefficient, shape, and acoustic field are similar to those of a numerical study and there is great advance in computation time.

Chapter 4. Concluding Remarks

In this dissertation, two improved empirical methods have been developed to apply DSM-II, a representative acoustic loads prediction method established based on free jet data, to various acoustic environment analysis. The first improved model is the empirical method which is able to take into account additional physical phenomena such as diffraction and reflection effect caused by the canister-like structure surrounding the missile. A diffraction and reflection model are introduced to be applied to existing empirical method. Then through the verification of the missile launched inside the canister, it is confirmed that it can simulate the diffraction and reflection effects well according to the height variation in terms of OASPL and spectrum. The first improved model is to placing an additional impingement source to overcome the inherent limitation of the original empirical method, which is called as ASDSM. To develop the ASDSM properly, this dissertation investigated the common characteristics of supersonic impinging jet noise comparable with free jet noise and found out that the noise component of broadband shock-associated noise could be added to the impingement region. Four characteristics of impingement source are examined specifically and finally impingement source is modeled according to the height variation. Through the many validation cases, it is confirmed that ASDSM leads to the improvement of both OASPL and

142

spectrum. And it could simulate the acoustic field more realistically compared with the experiments by the height variation. These two improved empirical method are significant in that they can complement the original empirical method. Because it was developed in 1972 based on free jet data, despite its advantages of accuracy and efficiency, it was confined to conventional lift-off cases and was considered unsuitable for recent launch vehicle acoustic loads research. However, the development of these two improved empirical methods overcomes the inherent problem of the original method so that it can be widely used for non-conventional lift-off cases, and several validation cases show that the results are also reliable.

In particular, the second improved empirical method called ASDSM is significant because it enables the empirical method to be alternative to the numerical method on the latest study of the multi-objective optimal design of low noise launch pad. This optimization problem has recently been a subject of interest in relation to launch vehicle acoustic loading and it has been mainly carried out by numerical approach due to the limitation of original empirical method. However, the numerical method for such a multi-objective optimization is very costly and requires too much computation time. For example, for only one optimization problem where the size of population is 50 and the number of generations is 50, i.e., 2,500 cases, the numerical-based study of Tatsukawa et al.[21] took about 7 hours using

143

1,040 CPU cores of "K" supercomputer for one case and it means that it will be took 730days for 2,500 cases. Eventually, the numerical approach is hardly to be a frequently-used method in the future for many realistic multi-objective optimization problems, because the launch environment has been diversified and the optimization requirements can also be changed variously. On the other hand, for the optimization problem where the size of population is 1,000 and the number of generations is 100, i.e., 100,000 cases, the whole procedures of the empirical approach took two days as a personal PC, ensuring reasonable results in terms of accuracy and reliability when compared with the numerical results.

To summarize all of this dissertation, the development of two improved empirical acoustic loads prediction methods would be significant in that they can overcome the inherent problem of the original method and widely be used for non-conventional lift-off cases, and make the acoustic field around the launch vehicle more practically according to height variation. And also, the application of second improved empirical method, ASDSM, to the study of multi-objective optimal design of low noise launch pad which is state-of-art research mainly done by numerical method can be powerful tool for the future study in relation to the multi-objective optimal design of low noise launch pad in aspect of both accuracy and efficiency.

There are several future works that can be performed after this dissertation. First, additional objective functions can be considered in a multi-objective optimization problem. For example, it is known that thermal stress is important for launch pad durability. Therefore, it can be studied to consider thermal stress additionally. However, since it is difficult to calculate the thermal stress on the launch pad using the current empirical method, this should be done through additional CFD or literature studies. The second is to consider the effect of water injection. Since the water injection is a typical method for reducing acoustic load and is currently applied in many launch environments, it can be further considered in future studies of acoustic loads. In addition to water injection, many methods of reducing acoustic loads can be included such as adopting front cover in the launch pad. Third, prediction accuracy problem at the far-field acoustic loads rather than near-field can be further studied. As mentioned before section of 2.3.4.3, Far-field acoustic loads were much overestimated compared to the experiment, which means that additional factors can be considered in far-field acoustic loads prediction, unlike near-field predictions. In order to solve these problems, there is a method of considering the atmospheric attenuation effect, which can be carried out in future studies. Finally, we can advance the model of the additional impingement source. In this thesis, we adopted only simple dipole source to reflect the additional acoustic waves due to the

145

impingement. However, since the actual physical phenomenon is much more complex, it can be simulated with various combinations of monopole, dipole, and quadrupole. Accordingly, a study to determine the location of a multi-source can also be performed in a future work.

Reference

1. 한국항공우주연구원, *우주산업실태조사*. 2012.
2. Roy, N., A. Girard, and A. Calvi, *Space engineering - Spacecraft mechanical loads analysis handbook*. 2013, European Cooperation for Space Standardization(ECSS). p. 1- 505.
3. Irvine, T., *Part I: Acoustic Pressure Level near Nozzle Exit Plane Revision H*, in *Rocket Vehicle Liftoff Acoustics*. 2000.
4. McInerny, S., *Rocket noise - A review*, in *13th Aeroacoustics Conference*. 1990.
5. Fujii, K., A. Oyama, and T. Nonomura, *Aeroacoustic Multiobjective Design Exploration of Rocket Launch Site Design*. 2014.
6. Varnier, J., W. Raguenet, and D. Gely, *Noise radiated from free and impinging hot supersonic jets*, in *4th AIAA/CEAS Aeroacoustics Conference*. 1998.
7. Lighthill, M.J., *On Sound Generated Aerodynamically, Part I, General Theory*. Proceedings of the Royal Society of London, 1952. **A-1107**(211).

8. Lighthill, M.J., *On Sound Generated Aerodynamically, Part II, Turbulence as a Source of Sound*. Proceedings of the Royal Society of London Series a-Mathematical Physical and Engineering Sciences, 1954. **A-1148**(222).

9. Ffowcs Williams, J.E., *The noise from turbulence convected at high speed*. Proceedings of the Royal Society A, 1963. **255**.
10. Tam, C.K.W., *On the noise of a nearly ideally expanded supersonic jet*. Journal of Fluid Mechanics, 2006. **51**(1): p. 69- 95.
11. Freund, J.B., *Noise sources in a low-Reynolds-number turbulent jet at Mach 0.9*. Journal of Fluid Mechanics, 2001. **438**.
12. Uzun, A., G.A. Blaisdell, and A.S. Lyrintzis, *Impact of Subgrid-Scale Models on Jet Turbulence and Noise*. AIAA Journal, 2006. **44**(6): p. 1365-1368.
13. Colonius, T., S.K. Lele, and P. Moin, *Sound generation in a mixing layer*. Journal of Fluid Mechanics, 1997. **330**.
14. Bogey, C., C. Bailly, and D. Juvé, *Computation of Flow Noise*

Using Source Terms in Linearized Euler's Equations. AIAA Journal, 2002. **40**(2): p. 235-243.

15. Berland, J., C. Bogey, and C. Bailly, *Large Eddy Simulation of Screech Tone Generation in a Planar Underexpanded Jet*, in *AIAA*. 2006.

16. Bodony, D., et al., *Investigating Broadband Shock-Associated Noise of Axisymmetric Jets Using Large-Eddy Simulation*, in *12th AIAA/CEAS Aeroacoustics Conference (27th AIAA Aeroacoustics Conference)*. 2006.

17. West, J., et al., *Development of Modeling Capabilities for Launch Pad Acoustics and Ignition Transient Environment Prediction*, in *AIAA 2012-2094, 18th AIAA/CEAS Aeroacoustics Conference*. 2012.

18. Tsutsumi, S., et al., *Numerical Study of Pressure Waves Generated by H-IIA Launch Vehicle at Lift-off*, in *AJCPP*. 2008.

19. Tsutsumi, S., et al., *Effect of Deflector Shape on Acoustic Field of Launch Vehicle at Lift-Off*, in *47th AIAA Aerospace Sciences Meeting including The New Horizons Forum and Aerospace Exposition*. 2009.

20. Tsutsumi, S., et al., *Study on Acoustic Prediction and Reduction of Epsilon Launch Vehicle at Liftoff.* Journal of Spacecraft and Rockets, 2015. **52**(2): p. 350-361.

21. Tatsukawa, T., et al., *Multiobjective Design Exploration of an Aeroacoustic Design Problem for Rocket Launch Site with Evolutionary Computation and Large Eddy Simulations*, in *10th AIAA Multidisciplinary Design Optimization Conference*. 2014.

22. Eldred, K.M., *Acoustic Loads Generated by the Propulsion System*, SP-8072, Editor. 1971, NASA

23. Campos, E., *Prediction of Noise from Rocket Engines*, in *11th AIAA/CEAS Aeroacoustics Conference*. 2005.

24. Haynes, J. and R. Kenny, *Modifications to the NASA SP-8072 Distributed Source Method II for Ares I Lift-Off Environment Predictions*, in *15th AIAA/CEAS Aeroacoustics Conference (30th AIAA Aeroacoustics Conference)*. 2009.

25. Plotkin, K., L. Sutherland, and B. Vu, *Lift-Off Acoustics Predictions for the Ares I Launch Pad*, in *15th AIAA/CEAS Aeroacoustics Conference (30th AIAA Aeroacoustics Conference)*. 2009.

26. Varnier, J., *Experimental Study and Simulation of Rocket Engine Freejet Noise.* AIAA Journal, 2001. **39**(10): p. 1851-

1859.

27.   박순홍 and 전영두, *KSR-III 로켓의 추진기관에 의한 음향 하중 예측 및 측정*, in *기계의 날 선포 및 2002년도 기계관련 산학연 연합심포지엄*. 2002.

28.   심형석, et al., *우주 발사체 화염유도로 형상에 따른 음향하중 분석*, in *KSAS 학술대회*. 2012.

29.   최상현, 이정권, and 이익진, *발사체 이륙 음향하중 예측 시 화염유도로 반사 효과 고려*, in *한국음향학회 2014년 추계학술대회*. 2014.

30.   Choi, S.-H., J.-G. Ih, and I.-J. Lee, *Effect of Source Line Location on Lift-off Acoustic Loads of a Launch Vehicle.* Transactions of the Korean Society for Noise and Vibration Engineering, 2015. **25**(8): p. 539-545.

31.   Koudriavtsev, V., J. Varnier, and A. Safronov, *A Simplified Model of Jet Aerodynamics and Acoustics*, in *10th AIAA/CEAS Aeroacoustics Conference*. 2004.

32.   Casalino, D., et al., *Improved Empirical Methods for Rocket Noise Prediction Through CAA Computation of Elementary Source Fields*, in *14th AIAA/CEAS Aeroacoustics Conference (29th AIAA Aeroacoustics Conference)*. 2008.

33.   Kudryavtsev, V.V. and A.V. Safronov, *Acoustic environment resulting in interaction of launch vehicle main engines jets with a launch pad having closed long ducts like a tunnel*, in *Progress in Flight Physics*. 2012. p. 405-420.

34.   Varnier, J. and W. Raguenet, *Experimental Characterization of the Sound Power Radiated by Impinging Supersonic Jets.* AIAA Journal, 2002. **40**(5): p. 825-831.

35.   Casalino, D., et al., *Hybrid Empirical/Computational Aeroacoustics Methodology for Rocket Noise Modeling.* AIAA Journal, 2009. **47**(6): p. 1445-1460.

36.   Varnier, J., V. Koudriavtsev, and A. Safronov, *Simplified Approach of Jet Aerodynamics with a View to Acoustics.* AIAA Journal, 2006. **44**(7): p. 1690-1694.

37.   Kandula, M., *Near-field acoustics of clustered rocket engines.* Journal of Sound and Vibration, 2008. **309**(3-5): p. 852-857.

38.   Plotkin, K., et al., *Prediction of rocket noise footprints during boost phase*, in *3rd AIAA/CEAS Aeroacoustics Conference*. 1997.

39.   Casalino, D., et al., *Rocket Noise Sources Localization Through a Tailored Beam-Forming Technique.* AIAA Journal, 2012. **50**(10): p. 2146-2158.

40. Kumar, S.A. and N. Karthikeyan, *Prediction of Launch Vehicle Noise during Lift-off using a Modified Eldred's Method*, in *The 14 th Asia Congress of Fluid Mechanics - 14ACFM*. 2013.

41. Crocker, M.J., et al., *Prediction of the Sound Pressure Fields on Space Vehicles and Ground*, in *The Sixteenth Internaltional Congress on Sound and Vibration(ICSV 2009)*. 2009.

42. Nonomura, T., Y. Goto, and K. Fujii, *Aeroacoustic waves generated from a supersonic jet impinging on an inclined flat plate.* International Journal of Aeroacoustics, 2011. **10**(4): p. 26.

43. Barbarino, M., F.P. Adamo, and D. Bianco, *A HYBRID APPROACH FOR LAUNCH SYSTEM SCATTERING OF EMPIRICAL CORRELATED NOISE SOURCES IN ROCKET NOISE PREDICTION*, in *23rd International Congress on Sound and Vibration*. 2016.

44. Donaldson, C.D. and R.S. Snedeker, *A study of free jet impingement. Part 1. Mean properties of free and impinging jets.* Journal of Fluid Mechanics, 1971. **45**.

45. Shen, J. and W.C. Meecham, *Quadrupole directivity of jet noise when impinging on a large rigid plate.* Journal of the Acoustical Society of America, 1992. **94**(3).

46. Nonomura, T., Y. Goto, and K. Fujii, *Aeroacoustic waves generated from a supersonic jet impinging on an inclined flat plate.* aeroacoustics, 2011. **10**.

47. Maekawa, Z., *Noise Reduction by Screens.* Applied Acoustics, 1968.

48. Deb, K., et al., *A Fast and Elitist Multiobjective Genetic Algorithm: NSGA-II.* IEEE TRANSACTIONS ON EVOLUTIONARY COMPUTATION, 2002. **6**(2).

49. Powell, A., *On the Effect of Missile Motion on Rocket Noise.* Journal of the Acoustical Society of America, 1958. **30**(11).

50. Eldred, K.M., W. Roberts, and R.W. White, *Structural Vibrations in Space Vehicles*, in *WADD TR 61-62*. 1961, NASA.

51. Lighthill, M.J., *Sound Generated Aerodynamically.* The Bakerian Lecture, 1961.

52. Davies, M.G. and D.E.S. Oldfield, *TONES FROM A CHOKED AXISYMMETRIC JET.* Acoustica, 1962. **12**.

53. Eldred, K.M., R.W. White, and M.A. Mann, *Suppression of Jet Noise with Emphasis on the Near Field*, in *Technical Documentary Report*. 1963, NASA.

54. Lighthill, M.J., *Jet Noise.* AIAA Journal, 1963. **1**(7): p. 1507-1517.

55. Ribner, H.S., *The Generation of Sound by Turbulent Jets*, in *Advances in Applied Mechanics Volume 8.* 1964. p. 103-182.

56. Laufer, J., R. Schlinker, and R.E. Kaplan, *Experiments on Supersonic Jet Noise.* AIAA Journal, 1976. **14**(4): p. 489-497.

57. Tam, C.K.W., *Supersonic Jet Noise*, in *Annual Reviews Fluid Mechanics.* 1995.

58. Phillips, O.M., *On the generation of sound by supersonic turbulent shear layers.* Journal of Fluid Mechanics, 1960. **9**(01).

59. Williams, J.E.F., *The Noise from Turbulence Convected at High Speed.* Philosophical Transactions of the Royal Society A: Mathematical, Physical and Engineering Sciences, 1963. **255**(1061): p. 469-503.

60. Ribner, H.S., *Eddy-Mach Wave Noise from a Simplified Model of a Supersonic Mixing Layer*, in *SP-207.* 1969, NASA.

61. Oertel Sen, H., F. Seiler, and J. Srulijes, *Visualization of Mach waves produced by a supersonic jet and theoretical explanations.* Journal of Visualization, 2013. **16**(4): p. 303-312.

62. Harper-Bourne, M. and M.J. Fisher, *The noise from shock waves in supersonic jets*, CP-131, Editor. 1974, AGARD (Advisory Group for Aerospace Research & Development).

63. Tanna, H.K., *An experimental study of jet noise. Part I : Turbulent mixing noise; Part II : Shock associated noise.* Journal of Sound and Vibration, 1977. **50**.

64. Seiner, J.M. and T.D. Norum, *Experiments on shock associated noise of supersonic jets*, in *AIAA 12th fluid and plasma dynamics conference.* 1979.

65. Seiner, J.M. and T.D. Norum, *Aerodynamic Aspects of Shock Containing Jet Plumes*, in *AIAA 6th Aeroacoustics conference.* 1980.

66. Norum, T.D. and J.M. Seiner, *Broadband shock noise from supersonic jets.* Aiaa Journal, 1982. **20**.

67. Seiner, J.M. and J.C. Yu, *Acoustic near-field properties associated with broadband shock noise.* Aiaa Journal, 1984. **22**(9).

68. Yamamoto, K., et al., *Experimental investigation of shock-cell noise reduction for single stream nozzles in simulated flight*, in *comprehensive data report.* 1984, NASA.

69. Powell, A., *On the Mechanism of Choked Jet Noise.* Proceedings of the Physical Society, 1953. **66**.

70.   Powell, A., *The noise of chocked jets.* Journal of the Acoustical Society of America, 1953. **25**.

71.   Sherman, P.M., D.R. Glass, and K.G. Duleep, *Jet flow field during screech.* Applied Scientific Research, 1976. **32**.

72.   Norum, T.D., *Screech suppression in supersonic jets.* Aiaa Journal, 1983. **21**.

73.   Krothapalli, A., V. Arakeri, and B. Greska, *Mach Wave Radiation: a Review and an Extension*, in *41st Aerospace Sciences Meeting and Exhibit.* 2003.

74.   Nielsen, P. and D. Papamoschou, *Mean Flow – Acoustic Correlations for Dual-Stream Asymmetric Jets*, in *47th AIAA Aerospace Sciences Meeting including The New Horizons Forum and Aerospace Exposition.* 2009.

75.   Azimi, M. and F. Ommi, *Supersonic Jet Noise: Main Sources and Reduction Methodologies.* Journal of Engineering Science and Technology Review, 2014. **7**(2).

76.   Norum, T.D. and J.M. Seiner, *Measurements of static pressure and far field acoustics of shock-containing supersonic jets.* 1982, NASA.

77.   Soderman, P.T., *Prediction of STOVL noise*, in *Royal Aeronautical Society International Powered Lift Conference.* 1990.

78.   Krothapalli, A., et al., *Flight Effects on the Far-Field Noise of a Heated Supersonic Jet.* AIAA Journal, 1997. **35**(6): p. 952–957.

79.   Sutherland, L.C., *Progress and problems in rocket noise prediction for ground facilities*, in *15th Aeroacoustics Conference.* 1993.

80.   Park, S., et al., *Improved empirical prediction method for impinging acoustic sources distributed around interactive structures.* Noise Control Engineering Journal, 2017. **65**.

81.   Lamont, P.J. and B.L. Hunt, *The Impingement of Underexpanded, Axisymmetric Jets on Perpendicular and Inclined Flat Plates.* Journal of Fluid Mechanics, 1980. **100**.

82.   Nakai, Y., N. Fujimatsu, and K. Fujii, *Experimental Study of Underexpanded Supersonic Jet Impingement on an Inclined Flat Plate.* Aiaa Journal, 2006. **44**.

83.   Inman, J.A., et al., *Fluorescence Imaging Study of Impinging Underexpanded Jets*, in *46th AIAA Aerospace Sciences Meeting and Exhibit.* 2008.

84.   Powell, A., *The Sound-Producing Oscillations of Round*

Underexpanded Jets Impinging on Normal Plates. Journal of the Acoustical Society of America, 1988. **83**.

85. Alvi, F.S. and K.G. Iyer, *Mean And Unsteady Flowfield Properties of Supersonic Impinging Jets With Lift Plates*, in *5th AIAA/CEAS Aeroacoustics Conference*. 1999.

86. Krothapalli, A., et al., *Flow Field and Noise Characteristics of a Supersonic Impinging Jet.* Journal of Fluid Mechanics, 1999. **392**.

87. Tsutsumi, S., et al., *Numerical Study on Acoustic Radiation for Designing Launch-Pad of Advanced Solid Rocket*, in *44th AIAA/ASME/SAE/ASEE Joint Propulsion Conference & Exhibit*. 2008.

88. Cole, J.N., R.T. England, and R. Powell, G, *Effects of Various Exhaust Blast Deflectors on the Acoustic Noise Characteristics of 1,000 Pound-Thrust Rockets*, in *WADD Technical Report*. 1960, NASA.

89. Tsutsumi, S., et al., *Acoustic Generation Mechanism of a Supersonic Jet Impinging on Deflectors*, in *52nd Aerospace Sciences Meeting*. 2014.

90. Akamine, M., et al., *Effect of Nozzle-Plate Distance on Acoustic Phenomena from Supersonic Impinging Jet*, in *22nd AIAA/CEAS Aeroacoustics Conference*. 2016.

91. Nonomura, T., et al., *Plate-Angle Effects on Acoustic Waves from Supersonic Jets Impinging on Inclined Plates.* AIAA Journal, 2016. **54**(3): p. 816-827.

92. Akamine, M., et al., *Effect of Nozzle-Plate Distance on Acoustic Phenomena from Supersonic Impinging Jet.* AIAA Journal, 2018. **56**(5): p. 1943-1952.

93. Meadows, K., R, *A Study of Fundamental Shock Noise Mechanisms*, in *NASA Technical Paper*. 1997.

94. Brehm, C., J. Housman, and C. Kiris, *Computational Aeroacoustics Analysis of a Jet Impinging on an Inclined Plate*, in *AMS Seminar Series*. 2015, NASA Ames Research Center.

95. Schloth, A.P., *Measuremenotsf M eanF low andA cousticP owerf or a SubsonicJ et Impingingt o a LargeR igid Surfac*, in *TM*. 1976, NASA.

96. Sutherland, L.C. and D. Brown, *Prediction Methods for Near Field Noise Environments of VTOL Aircraft*. 1972, Wyle Laboratory.

97. Bailly, C., et al., *An Analysis of Shock Noise Components.* ONERA Aerospacelab Journal, 2014(7).

98. Tam, C.K.W. and H.K. Tanna, *Shock Associated Noise of Supersonic Jets from Convergent-Divergent Nozzles.* Journal of Sound and Vibration, 1982. **81**(3).

99. Olsen, W.A., J.H. Miles, and R.G. Dorsch, *Noise Generated by Impingement of a Jet Upon a Large Flat Board*, in *NASA Technical Note.* 1972, Rewis Research Center.

100. von Glahn, U.H., D.E. Groesbeck, and R.G. Huff, *Peak Axial-Velocity Decay with Single and Multi-Element Nozzle*, in *NASA Technical Memorandum.* 1972, Rewis Research Center.

101. Park, S.H. and Y.D. Chun, *Prediction and measurement of acoustic loads generated by KSR-III propulsion system.* Journal of Korean Society for Noise and Vibration Engineering, 2002. **9**.

102. 채연석, et al., *3단형 과학로켓 개발사업(IV).* 2000, 한국항공우주연구소.

103. Breen, D., W. Regli, and M. Peysakhov, *B-Splines and NURBS*, in *Computer Graphics I.* Drexel University.

104. Peterson, J., *An Introduction to Knot Vectors. #5: How to use Knot Vectors.* 1990.

105. Srinivas, N. and K. Deb, *Multiobjective function optimization using nondominated sorting genetic algorithms.* Evolutionary Computation, 1995. **2**(3).

106. Chankong, V. and Y.Y. Haimes, *Multiobjective Decision Making: Theory and Methodology.* North-Holland, ed. A.P. Sage. 1983.

107. Hwang, C., L. and M.A.S. Md., *Multiple objective decision making, methods and applications: a state-of-the-art survey.* 1979: Springer-Verlag.

108. Miettinen, K., *Multiobjective Optimization.* 1999: Springer.

109. Yoon, J., J. Lee, and D. Kim, *Feature selection in Multi-label classification using NSGA-II Algorithm.* Journal of KISS : Software and Applications, 2013. **40**(3).

110. *Pearson correlation coefficient.* 2019. p. https://en.wikipedia.org/wiki/Pearson_correlation_coefficient.

국문초록

경험적 방법과 진화알고리즘을 이용한

저소음 발사대의 다목적 최적설계 연구

박 서 룡

기계항공공학부 우주항공공학과

서울대학교 대학원

음향하중은 우주발사체 발사시에 초음속 제트화염에 의해 발생하는 강한 음향파로서 우주발사체 진동에 원인이 되며 안테나 패널이나 내부 전자장치의 성능을 악화시킬 수 있다. 따라서 발사체 주변의 음향환경을 미리 예측하는 것은 중요하다.

음향하중을 예측하는 데에는 대표적으로 2 가지 방법은 수치적 방법과 경험적 방법이다. 수치적 방법을 이용하여 발사체 주변 음향환경을 예측하는 데에 드는 비용은 매우 크기 때문에, 많은 연구들이 경험적 방법을 기반으로 이루어져왔다. 가장 대표적인 경험적 예측 방법은 소음원분포기법(DSM)으로서 NASA SP-8072 보고서를 통해 개발되었다. 하지만 이 방법은 자유제트 실험 데이터를 기반으로 하기 때문에 몇몇 물리적 현상을 고려하기

어렵다는 한계가 있다. 본 학위논문에서는, 개선된 경험적 방법을 개발하여 기존의 경험적 방법에서 고려하지 못하는 물리현상을 추가적으로 고려함으로서 실제 발사 환경에 형성되는 음향 환경을 더욱 정확히 예측하는 것을 목표로 한다.

한편 최근 발사체 발사 환경이 다변화됨에 따라 저소음 발사대에 대한 많은 연구가 진행되고 있다. 또한 저소음 발사대는 소음 측면뿐만 아니라 발사대에 대한 충돌힘 및 발사대 건설 비용 등 추가적인 요구조건을 고려할 필요가 있다. 이러한 저소음 발사대의 최적설계 연구는 주로 수치적 방법을 기반으로 수행되었는데, 이때 계산 비용이 아주 많이 수반되었다. 하지만 본 학위논문에서는 저소음 발사대의 최적설계 연구를 경험적 기반으로 수행하는 것을 목표로 한다. 이를 위해 경험적 방법에 몇 가지 방법을 추가로 도입하였다. 1) 곡선형 발사대 형상을 자유롭게 시뮬레이션 할 수 있는 방법인 NURBS(Non-Uniform Rational B-Spline)와 2) 다목적 최적설계 알고리즘인 NSGA-II (Non-dominated Sorting Genetic Algorithm-II) 이다. 이러한 방법을 경험적 방법에 적용한 후에 우리는 저소음 발사대의 다목적 최적 설계 연구에 대한 경험적 방법의 활용 결과를 정확성과 효율성 측면에서 살펴본다.

주요어: 음향하중 예측, 경험적 예측 방법, 다목적 최적설계, 저소음 발사대, 넙스 곡선, 비지배 정렬 진화 알고리즘

학번: 2012-20667

감사의 글

큰 꿈을 안고 대학원에 입학했던 20 대 중반부터 이제는 어느덧 배가 조금 나온 30 대 초반의 나이까지, 수많은 희로애락과 함께 했던 제 청춘의 대학원 생활을 이 글로 마무리합니다. 7 년 반이라는 시간 동안 가장 값진 경험을 꼽자면 살아계신 하나님을 만난 일일 것입니다. 풋풋했던 새내기의 열정은 점점 사그라지고, 좀처럼 내 의지대로 인생이 살아지지 않아서 자존감이 낮아질 때, 하나님께서는 무력하고 지친 저를 일으켜 이 자리까지 인도하셨습니다. 인생의 진정한 목표를 깨닫게 하시고, 무한한 은혜를 주신 하나님 아버지께 영광 돌립니다.

먼저 지도 교수님이신 이수갑 교수님께 감사드립니다. 부족한 모습이라도 질책이나 타박보다는 격려와 칭찬으로 지도해 주셔서 감사합니다. 교수님 덕분에 언제나 용기를 가지고 연구에 임할 수 있었습니다. 또한 교수님의 유머 있는 말씀으로 연구실이 항상 밝고 긍정적이었던 것 같습니다, 진심으로 감사하고 존경합니다. 항상 건강하십시오. 또한 부족한 제 논문을 심사해 주시고 여러 도움을 주셨던 심사위원분들께 감사드립니다. 신상준 교수님, 이복직 교수님과 멀리 대전에서 와주신 박광근, 김민우 선배님께 진심으로 감사드립니다.

CAA 팀 선배로 신입생 때부터 의지했던 경태 형, 규호 형, 병학이 형과 입학부터 함께 동고동락했던 동기 석종이, 같이 살며 수많은 삶의 부분을 공유했던 봉천동 가족 아침이와 동연이, 같이 졸업하면서 여러

157

도움을 준 찬일이 형, 신입생 때부터 여러 도움을 준 정우와 동욱이, 언제나 밝은 에너지를 주는 종희, 똑부러지고 똑똑한 지훈이, 착하고 성실한 재헌이, 자기만의 세계에 사는 매력적인 두 친구 현기와 원석이, 까다로운 과제를 맡아줘서 고마운 비그네쉬와 인정이, 위닝 메이트 원희, 신입생 병현이 국환이 태석이 호민이, 뒤에서 연구실을 든든히 지켜주시는 하경씨와 그 외에도 이미 졸업하신 은국이 형, 지영 누나, 승민이 형, 승훈이 형, 태형이 형, 두영이 형, 민우 형, 병호 형, 열완이, 기섭이, 홍석이, 재현이, 승수, 영환이, 경범이 등.. 너무 좋은 사람들과 함께 연구실 생활을 할 수 있어서 너무 감사했습니다.

또 어려서부터 제 인생의 많은 부분을 차지하며 인격을 형성해준 고마운 친구들. 학부 때부터 대학원 졸업할 때까지, 형제처럼 언제나 함께 지냈고 앞으로도 그렇게 지낼 든든한 해성이. 초등학교 때부터 운동하며 인생을 함께 해온 LSM 친구들, 어느덧 각자의 자리에서 멋진 어른이 된 중학교 친구들, 아직도 만나면 예전처럼 팔팔한 고등학교 친구들, 언제 만나도 든든하고 힘이 되어주는 대학교 친구들, 그동안 너무 고마웠고, 항상 사랑하고 기도한다 친구들아!

또한 여러 믿음의 동역자 분들께 감사드립니다. 리더로서, 믿음의 선배로서 많이 의지하고 배웠던 호정이 형, 석수 형, 선영 누나, 성은 누나, 단비, 보라 누나, 지혜 누나와 그 외에 많은 강남교회, 은향교회 지체분들께 감사드립니다. 그리고 항상 귀한 말씀으로 이끌어주신 디렉터 김상순 목사님, 노주찬 전도사님, 임노아 목사님, 친분은 거의

없지만 유튜브로 항상 말씀을 접하게 해주신 정준경 목사님, 고문산 목사님, 이규호 목사님, 이분들이 없었다면 저는 지금 무엇을 보고, 바라며 살고 있었을까요? 다시 한 번 진심으로 감사드립니다.

저를 낳으시고 길러주신 부모님, 어려운 형편에도 저를 끝까지 믿고 지켜봐 주셔서 감사합니다. 그동안 고생 참 많으셨죠, 앞으로 인생의 남은 기간 동안 잠잠히 보답하며 살겠습니다. 또, 우리 조카 샬롬이를 임신 중인 누나와 언제나 믿음직스러운 매형, 그동안 함께 할 수 있어서 너무 힘이 됐습니다, 감사합니다.

마지막으로, 내년에 저의 신부가 될 다인이. 결혼을 허락해줘서, 미래를 함께 하자고 약속해줘서 고마워요. 부족하고 연약한 제 모습을 누구보다 잘 알고 있지만, 항상 넓은 마음으로 이해해주며 응원해준 그 모습들, 항상 잊지 않을게요. 다인이 덕분에 지칠 수도 있었던 박사과정 막바지에 힘을 낼 수 있었던 것 같아요. 항상 고맙고 또 미안합니다. 앞으로도 지금처럼 서로 사랑하며 살아가요. 그리고 이렇게 예쁘고 착한 다인이를 낳아주시고 길러주신 예비 장인, 장모님, 언제나 저희를 믿어주시고 응원해주셔서 감사드립니다.

부족한 모습이 많았지만, 돌아보니 정말 감사한 일들과 감사한 사람들뿐이었습니다. 그렇기에 이 졸업은 제 힘으로 한 것이 아닌 거겠죠. 앞으로 겸손하게, 성실하고 정직하게 살겠습니다. 감사합니다.

박서룡 올림